ENTRANCE CHANNEL EFFECTS ON THE ALPHA DECAY PROBABILITIES OF NEUTRON AND PROTON INDUCED REACTIONS FOR TARGET MASS A=55 AND CHARACTERIZATION OF RF OSCILLATOR FOR LOW ENERGY CHARGED PARTICLE ACCELERATOR

By

H. Lalremruata

Department of Physics

Submitted

in partial fulfillment of the requirement of the Degree of Doctor of Philosophy in Physics of Mizoram University, Aizawl.

Declaration

Mizoram University

October 2019

I, H. Lalremruata, a Ph.D scholar in the Department of Physics, Mizoram University, do hereby declare that the subject matter of this thesis is the record of work done by me, that the contents of this thesis did not form basis of the award of any previous degree to me or to the best of my knowledge to anybody else, and that the thesis has not been submitted by me for any research degree in any other University/Institute.

This thesis is being submitted to Mizoram University for the degree of Doctor of Philosophy in Physics.

(H. LALREMRUATA)
Candidate

(Dr. B. LALREMRUATA)
Supervisor

(Dr. HRANGHMINGTHANGA)
Joint Supervisor

(Prof. R.C Tiwari)
Head

Dr. B. Lalremruata
Assistant Professor
Department of Physics
Mizoram University
Tanhril-796004
Aizawl, Mizoram

MIZORAM UNIVERSITY
DEPARTMENT OF PHYSICS
AIZAWL 796 004 MIZORAM
Phones: 0389 - 2330435, - 2330522
FAX : 0389 - 2330522
Mobile : +919436779952
E-mail : marema08@gmail.com

(A Central University Established by an Act of Parliament)

No. MZU/NUC-PHY/19/47 Date: 11th October, 2019.

Certificate

This is to certify that the thesis entitled ***"Entrance channel effects on the alpha decay probabilities of neutron and proton induced reactions for target mass A=55 and characterization of RF oscillator for low energy charged particle accelerator"*** *submitted by Mr. H. Lalremruata, for the degree of Doctor of Philosophy in Physics, of the Mizoram University: Aizawl, India, embodies the record of original investigations carried out by him under my supervision. He has been duly registered and the thesis presented is worthy of being considered for the award of Ph.D. degree. This research work has not been submitted for any degree to any other university.*

(Dr. B. LALREMRUATA)

Supervisor

(Dr. HRANGHMINGTHANGA)
Joint Supervisor

Acknowledgement

After an intensive study of few years, I finally reached the finishing touch of my Ph.D thesis. I would like to express my sincere gratitude to all those who helped me throughout the period of my research.

First of all, I would like to thank my supervisor Dr. B. Lalremruata for giving me the opportunity to complete my Ph.D research work under his supervision; without which I would not have completed this challenging research work. Thank you for giving me an opportunity to explore the world of Nuclear Physics and meet people I would have never come across in my life; I treasure the experience and discussions in the Nuclear Physics Research group. I also appreciate his devotion, ever helping hand, technical inputs and knowledge shared with me, which will always have a big impact in my future career.

I would like to thank my Joint Supervisor, Dr. Hranghmingthanga, for his help in the construction and characterization of the RF oscillator. He has always been there for me whenever I come across problems in the electronics part of my research work. I would never forget the efforts and new ideas he contributed to complete my research.

I would also like to extend my special thanks to the faculty of the Department of Physics, Mizoram University for their kind valuable help at various phases of my research. I express my sincere thanks to Prof. Zaithanzauva Pachuau (DEAN, SPS), Prof. R.C. Tiwari (Head, Department of Physics), Prof. Suman Rai, Prof. R.K. Thapa and Dr. Lalthakimi Zadeng for their encouraging words and support extended

towards me. My heartfelt thanks also go to all the non-teaching staff of the Department of Physics, Mrs. Nunpuii, Mr. Mala, Mr. Ngaia and Mrs.. Luri.

My acknowledgement will never be completed without special mention to my labmates, J. Lanthari, Mamawia, Samuel, Dr. Andrew, Biaktluanga, Zari and Ramnghaka, for their kind support. We were not only able to support each other by deliberating over our problems and findings, but also happily talking about things beyond research works.

I am extremely thankful to my family, who meant the world to me. I treasure the support, prayers, endless love, encouragement and help rendered to me in every phase of my personal and academic life without which the completion of my work would not have been possible. I consider myself the luckiest to have such an understanding and supportive family.

Most importantly, I would like to thank Almighty God for giving me good health and strength to be able to complete my research work.

Dated: 11th October, 2019

Mizoram University

(H. LALREMRUATA)

Department of Physics
Mizoram University
Aizawl, Mizoram

CONTENTS

List of Figures

List of Tables

Dedication

This work is dedicated to everyone who had always been true to me and helps me along my journey.

CHAPTER 1

INTRODUCTION

1. INTRODUCTION

1.1. Nuclear data and its applications

In the study of nuclear science and technology, nuclear data is the key component in the development and understanding of the nuclear systems and all of its applications. Nuclear data consist of experimentally measured or evaluated data consisting of a large number of physical quantities, like scattering and reaction cross sections, nuclear structure and nuclear decay parameters, etc. which are relevant for nuclear physics and nuclear applications.

A complete nuclear data for all isotopes are desirable for nuclear astrophysics, safe reactor design, transmutation, understanding nuclear structure and reaction dynamics, improving existing nuclear model parameters for better prediction, industrial and medical applications. However, for various nuclear applications, experimentally measured nuclear data are not available to cover all the required energies. Moreover, due to the fact that some isotopes are unstable and short-lived, or the reaction cross section itself is very small, it is sometimes impossible or difficult to measure their cross sections directly with the present technology. Therefore, in such cases, incomplete or inconsistent experimental data are coupled with the optimum theoretical models to produce evaluated data (Gunsing *et al.*, 2015; Chadwick *et al.*, 2006). These evaluated data are produced such that the important data for all the nuclear reactions at all energy regions are covered. Although the existing nuclear data covers rather complete information for all the nuclear reactions, there is still a need for further improvement in the evaluation of

nuclear data which may include evaluating the validity of nuclear models and the choice of parameters within it, and the technique adopted in analyzing a variety of observables related to the compound nucleus decay (Ajay Kumar, 2014).

1.2. Radiation effects in nuclear reactor materials - Necessity of nuclear data for unstable nuclei

In nuclear reactor developments, the generation of hydrogen and helium through neutrons has always been a very serious problem. In addition to the production of hydrogen and helium, the other processes such as atomic displacements and transmutations, etc. can produce micro-structural defects in the material. More precisely, two effects are known to occur in non-fissile materials in the intense neutron environment of a nuclear reactor:

(1) The extensive displacements of the atoms from their lattice sites due to elastic interactions with the impinging neutrons, and

(2) The formation of impurity atoms in the materials by transmutation reactions.

Both these effects, the displacement of atoms from their lattice sites and the consequent production of various types of defect structures as well as the production of impurity atoms due to transmutation reactions can influence important macroscopic properties like strength, ductility and dimensional stability which are the most important features for the practical application of the structural materials. The changes brought about by irradiation on these properties are quite often unfavorable and adverse, justifying the influence of radiation on materials being referred to as "radiation damage" (Rodriguez *et al.*, 1984). There have been many serious accidents occurred in nuclear power plants which results in many deaths and

the surrounding areas are left uninhabited. Out of such incidents, the three high-profile accidents that fueled most people fear of the nuclear power are the Three Mile Island, Chernobyl and Fukushima Daiichi.

The structural material, generally stainless steel, comprises of Fe, Ni, Cr, Mn, Co, Nb, etc. In the Stainless Steel of type SS316, the content of Fe and Cr are approximately 65% and 17% respectively. In the fusion reactors, the structural materials are exposed at a high fluence of 14.1 MeV neutrons. The high production rate of ^{55}Fe, having a half life of 2.744 years (Huo Junde, 2008), from the neutron exposure of natural iron via the threshold reaction ^{56}Fe(n,2n)^{55}Fe, ^{54}Fe(n,γ)^{55}Fe, ^{58}Ni(n,α)^{55}Fe and the production rate of ^{55}Cr via ^{53}Cr(n,γ)^{54}Cr(n,γ)^{55}Cr, ^{54}Cr(n,γ)^{55}Cr and ^{52}Cr(n,γ)^{53}Cr(n,γ)^{54}Cr(n,γ)^{55}Cr is of main concern as an activation product during the lifetime of an operating reactor (Wallner *et al.,* 2011). Since Chromium is structural elements in fission and fusion reactors, accurate knowledge of neutron or proton induced reaction cross sections for its stable as well as unstable isotopes is very important. The neutron induced reactions on ^{55}Fe and other long-lived radionuclides, however, are difficult to measure using the standard activation techniques due to the unstable nature of the targets and their low activities. For this purpose and other applications, the values of total cross-sections for the production of charged particles in the reactor materials through nuclear reactions induced by different projectiles in the energy range from few keV to 20 MeV are required (Lalremruata *et al.,* 2009). Recent studies have shown that there is a possibility in extracting the total cross sections of such nuclei which are impossible or difficult to measure experimentally.

1.3. Literature survey: Entrance channel effects on the compound nucleus decay

Ghoshal (1950) performed an experiment to study the excitation functions of ^{64}Zn formed between proton and alpha particle induced reactions on ^{63}Cu and ^{60}Ni respectively. He established the validity of Bohr's independent hypothesis that the decay of compound nucleus does not depend on its mode of formation. Several authors recently studied heavy ion fusion of some nuclei and observed an entrance channel effect in the decay of a compound nucleus.

Bissem *et al.* (1980) studied the decay of the composite system ^{66,68}Ga* formed through d+^{64,66}Zn and ^{3}He+^{63,65}Cu at E_d = 9-26 MeV and E(^{3}He) = 10–44 MeV respectively. They observed entrance channel dependence in the yields for single *p*- and *n*- emission. Ruckelshausen *et al.* (1986) reported that an unexpected entrance channel effect was observed in the decay of the compound nucleus ^{156}Er formed between the nearly mass-symmetric ^{64}Ni+^{92}Zr and asymmetric ^{12}C+^{144}Sm entrance channels. Similar results were also observed by Thoennessen *et al.* (1991) in the decay of excited compound nuclei ^{160}Er and ^{164}Yb at excitation energies 53 MeV and 49 MeV respectively. The compound nuclei ^{160}Er were formed by bombardment of ^{16}O and ^{64}Ni on the isotopically enriched ^{144}Nd and ^{96}Zr respectively, and the compound nuclei ^{164}Yb were formed via the entrance channels ^{16}O + ^{148}Sm and ^{64}Ni + ^{100}Mo. They observed that the gamma ray spectra from ^{16}O induced reactions on ^{144}Nd show a typical giant dipole resonance bump whereas the gamma ray spectra from the more symmetric entrance channels ^{64}Ni+^{96}Zr and ^{64}Ni+^{100}Mo show a dramatically different shape. They claimed that the differences

observed in the gamma ray spectra between the different entrance channels arises from detailed nuclear structure effects in the early stages of the compound nucleus decay.

Ajay Kumar (2014) observed an angular momentum variation in the compound nuclei ^{76}Kr* formed by the fusion reactions of the asymmetric entrance channel ^{12}C+^{64}Zn and the symmetric entrance channel ^{31}P+^{45}Sc at the excitation energy of 75 MeV. In the case of the compound nucleus ^{76}Kr* formed via the asymmetric entrance channel ^{12}C+^{64}Zn, the maximum angular momentum is 41ħ which is the same as suggested by the Bass model (Bass, 1973) and the neutron spectra are in good agreement with the statistical model calculations using the normal-level density parameter a = A/8 MeV^{-1}; whereas the maximum angular momentum is 30ħ in the case of the compound nucleus ^{76}Kr* formed via the symmetric entrance channel ^{31}P+^{45}Sc and found that the neutron spectra are not in agreement with the statistical model predictions using normal parameters as used for the asymmetric system.

A more detail investigation on heavy ion reactions was made by Anastasi *et al.* (2018) towards the various properties of de-excitation of the same ^{220}Th* compound nuclei, formed by the four different entrance channels ^{16}O+^{204}Pb, ^{40}Ar+^{180}Hf, ^{82}Se+^{138}Ba and ^{96}Zr+^{124}Sn. Even though the compound nucleus ^{220}Th* is characterized by the same Z and A values and has the same excitation energy E^*_{CN}, the authors pointed out the effects of the entrance channel on the compound nucleus formation and the consequent different ways of its de-excitation cascade in the emissions of charged particles proton and alpha together with neutron emission.

They reported that the reason of the different way of de-excitation is due to the different orbital angular momentum distribution in the four considered entrance channels.

The role of entrance channel effects for prediction of charged particle spectra from the compound nuclei formed via the fusion of asymmetric and symmetric systems was reported by Govil *et al.* (2000). In their experiment, a nearly same compound nucleus having same angular momentum 42ħ and the same excitation energy of 84 MeV was formed through the fusion reaction of $^{12}C+^{45}Sc$ asymmetric system and $^{28}Si+^{27}Al$ symmetric system. They observed that the α-spectra from $^{28}Si+^{27}Al$ symmetric system deviate at both higher and lower energies from the statistical model calculations while the measured α-spectra from $^{12}C+^{45}Sc$ asymmetric system agrees the predictions from the statistical model calculations. However, the authors claimed that these results could be quite different when it comes to higher masses and at high excitation energies where the dynamics of the reactions are perhaps quite different. Boger *et al.* (1994) also studied the α-evaporation spectra from the composite nuclei $^{147,149}Tb^*$ formed by $^{40}Ar+^{nat}Ag$ at 337 MeV and $^{86}Kr+^{63}Cu$ entrance channels. Cinausero *et al.* (1996) have also reported the comparison of α-evaporation spectra for three different systems $^{86}Kr+^{76}Ge$, $^{16}O+^{150}Sm$ and $^{60}Ni+^{100}Mo$. They have concluded that the α-evaporation spectra for these systems are independent of the entrance channel.

Since the 1970's, surrogate method had been utilized successfully for neutron induced fission cross section measurements (Escher *et al.*, 2012; Cramer and Britt, 1970; Britt and Wilhelmy, 1979; Younes and Britt, 2003; Younes and Britt, 2003;

Petit *et al.*, 2004; Plettner *et al.*, 2005; Burke *et al.*, 2006; Lyles *et al.*, 2007; Lyles *et al.*, 2007; Nayak *et al.*, 2008; Goldblum *et al.*, 2009; Basunia *et al.*, 2009; Lesher *et al.*, 2009; Goldblum *et al.*, 2010; Lesher *et al.*, 2010; Kessedjian *et al.*, 2010; Ressler *et al.*, 2010; Ressler *et al.*, 2011; Desai *et al.*, 2013; Desai *et al.*, 2013). Recently, the surrogate ratio method was also used to measure the ^{55}Fe(n,p) reaction cross section in the incident energy range 7.9 – 20.1 MeV (Bhawna Pandey *et al.*, 2016). A lot of efforts have also been given to extend the surrogate method for other reaction channels such as for neutron capture cross sections and theoretical investigations have been performed (Forssen *et al.*, 2007). Experimental investigations have also been performed for well known neutron capture reactions (Bernstein *et al.*, 2006; Boyer *et al.*, 2006; Goldblum *et al.*, 2008; Allmond *et al.*, 2009; Hatarik *et al.*, 2010). Recently, Boutoux *et al.* (2012) performed experiment for ^{172}Yb(n,γ) and ^{175}Lu(n,γ) with ^{174}Yb(^{3}He,αγ)^{173}Yb and ^{174}Yb(^{3}He,pγ)^{176}Lu reactions as their surrogates respectively. They observed large discrepancies in the gamma decay branching ratio between the surrogate and the desired neutron induced reactions. This large discrepancy is attributed to the fact that gamma decay probabilities are very sensitive to the mismatch in the J^{π} distributions between the compound nucleus formed by the surrogate and desired reactions. They reported that the average compound nucleus spin is 3–4 ħ higher in the surrogate reaction than the neutron induced reaction. Scielzo *et al.* (2010) also performed experiments to investigate the reliability of ^{153,155,157}Gd(n,γ) reactions using the surrogate reactions ^{154,156,158}Gd(p,p'). They also observed large deviation in the gamma emission probabilities from the direct and surrogate reactions. They concluded that in order to extract reliable (n,γ) cross

sections, a more sophisticated analysis should be developed that takes into account angular momentum differences between the neutron induced and surrogate reactions.

1.4. Basic principles of RF oscillator

Oscillator is an electronic device for generating an AC signal voltage. Oscillators generate sinusoidal or non-sinusoidal waveform from very low frequencies up to very high frequencies. It converts direct current (DC) from a power supply to an alternating current (AC) signal.

Basically, an RF oscillator is an amplifier that provides itself (through feedback) with an input signal. It is a non-rotating device for producing alternating current, the output frequency of which is determined by the characteristics of the device.

Oscillators are characterized by the frequency of their output signal:

1) A low frequency oscillator (LFO) is an electronic oscillator that generates a frequency below 20 Hz. This term is typically used in the field of audio synthesizers, to distinguish it from audio frequency oscillators.
2) An audio oscillator produces frequencies in the audio range, about 16 Hz to 20 kHz.
3) An RF oscillator produces signals in the radio frequency range of about 100 kHz to 100 GHz.

An RF oscillator produces a periodic signal without any input signal. Depending on the requirement of the frequency range, there are different types of oscillator circuits. In order to achieve high frequencies, the RF oscillator is developed with an LC oscillator circuit; typically the Hartley, Colpitts, Clapp

circuits, etc. The basic principle of an oscillator circuit can be explained via a linear feedback system. Figure 1.1 shows the basic block diagram of the oscillator circuit. It includes an amplifier and a resonator, which comprise the positive feedback network. When the power is switched ON, the circuit produces noise. The noise is amplified by the amplifier, and passes through a resonator circuit which has filter function. At last what's left is the signal in the passband.

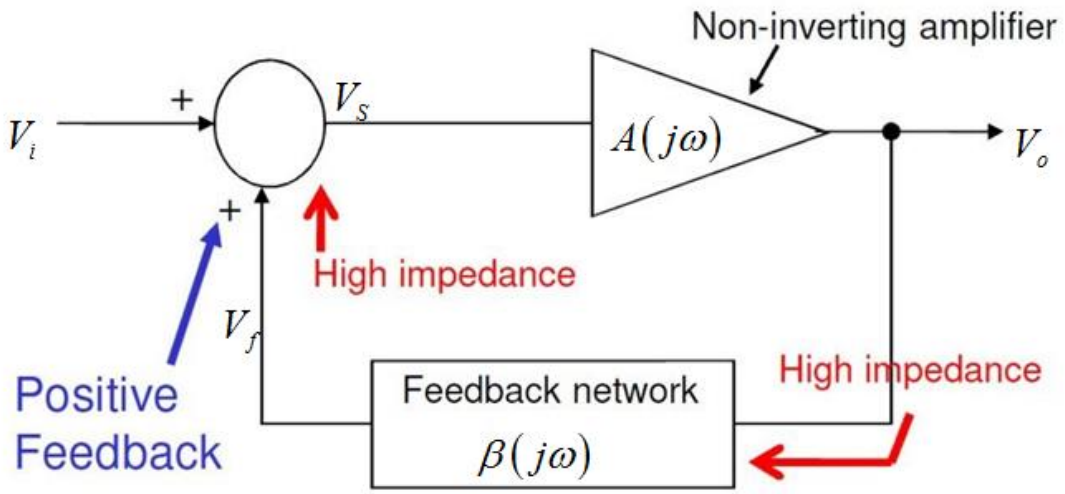

Figure 1.1: Basic block diagram of oscillator circuit.

The unwanted signal is filtered by the resonator. So, the signal that passes through the resonator will then be send to the input port of amplifier and combine with the original signal having the same phases with each other. The signal will be amplified again at this stage. The transfer function can be expressed as:

$$A_f(jw) = \frac{V_o(jw)}{V_i(jw)} = \frac{A(jw)}{1 - A(jw)\beta(jw)} \qquad \text{..... (1.1)}$$

The definition of open loop gain is:

$$L(jw) = A(jw)\beta(jw) \qquad \text{..... (1.2)}$$

Using Barkhausen principle, the oscillation condition is:

$$L(jw_o) = A(jw_o)\beta(jw_o) = 1 \qquad \text{..... (1.3)}$$

Therefore, a specific corner frequency ω_0 can be obtained to ensure that the open loop gain $L(jw_o)$ is equal to 1, and the phase must be 0^0, that is:

$$\left|A(jw_o)\beta(jw_o)\right| = 1 \qquad \text{..... (1.4)}$$

$$\arg\left[A(jw_o)\beta(jw_o)\right] = 0^0 \qquad \text{..... (1.5)}$$

In order to satisfy Equations (1.3) and (1.4), the product of the feedback factor and the amplifier gain should be 1. Meanwhile, the total summation of the phases is zero after feedback. Therefore, Figure 1.1 can be changed to figure 1.2 for different structures of amplifier.

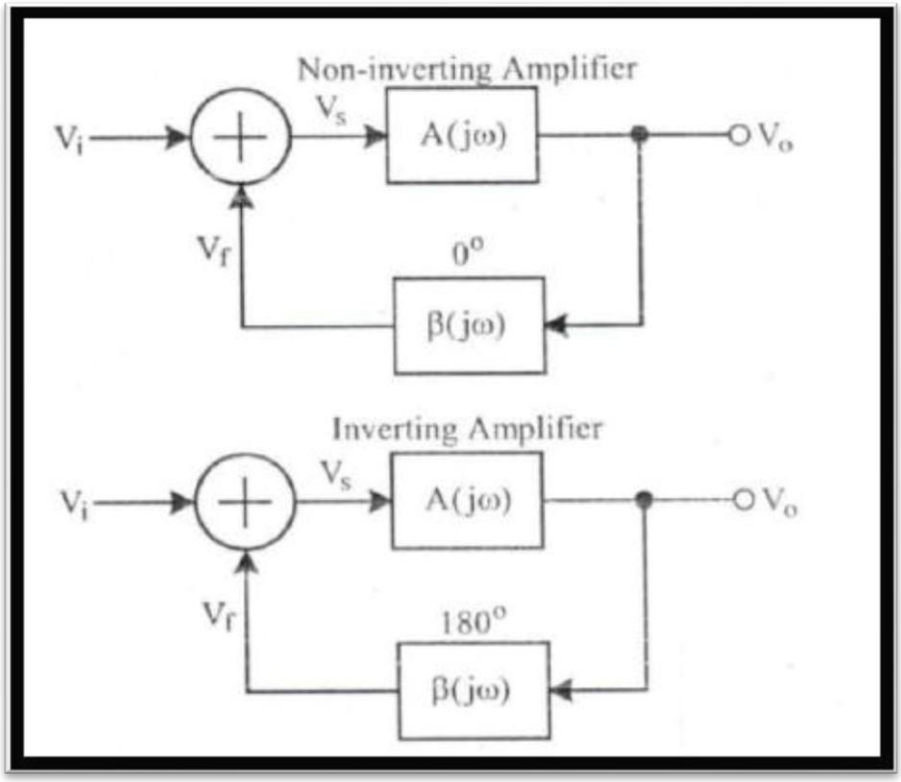

Figure 1.2: Oscillator circuits comprised by non-inverting and inverting amplifier.

1.5. Applications of RF oscillator and motivation of the work

An RF radiation has many applications in various fields such as communication systems, medical sciences, etc. The main focus of the present study lies in the development of ion sources. The use of RF voltage to create plasma in ion sources dates back to the late 1940s (Thonemann *et al.*, 1948; Hall, 1948). Since then, the improvements made on radio frequency ion sources to deliver large ion beams has been one of the most important advancement in the development of particle accelerators(Thonemann, 1946; Goodwin, 1953; Eubank *et al.*, 1954). Ion sources have widespread applications in industrial plasmas (Kaufman *et al.*, 1982), neutral-beam injection (NBI) systems for fusion devices (Fantz *et al.*, 2007), bio-

medical sciences (Schardt *et al.*, 2010), particle accelerators (Brown *et al.*, 2004) and mass-spectrometry (Houk *et al.*, 2004). In an RF driven ion source, the high frequency electric field accelerates free electrons to energies that are high enough to ionize atoms or molecules with which they collide. The density of the plasma thus created depends on the RF signal frequency and power, and plays crucial role in the performance of the ion source (Zhu *et al.*, 2007; Tripathi *et al.*, 2011).

In the development of RF ion sources, the main factors to be optimized are the operating frequency and output power of the RF oscillator, extraction probe voltage and the ion current. Out of the various factors that affect the ion current extracted from ion sources, the effect of RF power on the plasma density is the main interest of the present study. Numerous works have been seen in literature on the design and construction of RF ion sources (Brown *et al.*, 2004; Tripathi *et al.*, 2011). However, these studies are mainly devoted to the extraction and different characteristics of plasma, and little attention has been paid towards RF oscillator itself. In the operation of vacuum tube RF oscillator, the only parameter used to adjust the total output power level is the DC plate voltage. Thus understanding the relationship between the two parameters is important for proper operation of the oscillator. To measure the output power of the oscillator, two simple and inexpensive techniques, namely, a modified form of photometric method and an RF peak voltage detection method were used. Photometric method is one of the oldest methods of RF power measurement in history. It is based on the ability of incandescent lamp to convert RF power into light which is then measured with a photometer (Conhaim *et al.*, 1963; TM 11-685/TO 31R-1-9, 1961s). However, this method is rather classified

as power indicator than absolute power measurement due to the inductive reactance of the load at high frequency. On the other hand the latter method is one of the standard and well known methods where RF power is made to be absorbed by a purely resistive load and the electrical energy consumed is calculated from the RF signal peak voltage. The detail procedure for RF power measurement using these two different methods is discussed.

It has been reported that an RF ion source with power up to 300 W provides high current density at the operating frequency of 27.12 MHz (Voznyi *et al.*, 2013). The saturation in the ion current can be achieved at an RF power of 380 W according to their experimental observations (Ganguly and Bakhru, 1963). The frequency of the RF oscillator used in their study was 40 MHz. Although it is now understood that saturation in the ion current can be achieved at a particular frequency, it is still important to understand the operational characteristics of an RF oscillator in terms of its operating frequency. Therefore, the effect of the operating frequency of an RF oscillator on its output power which is basically determined by the design of the tank circuit or RF coil, used as antenna is studied in the present work. The dependence of the operating frequency on the design of the RF coil is also discussed.

Among the various designs available, vacuum tube self-excited push-pull oscillator is one of the most commonly used RF signal generator in radio frequency (RF) driven plasma source. Even though there are now more efficient semi-conductor based RF power sources, vacuum tube oscillator, especially self-excited push-pull RF generator continues to occupy important place in the design and construction of RF ion sources due to its circuit simplicity, robustness, compactness

and ease of maintenance. However, electron tubes are high voltage devices and have operating conditions different from that of semiconductor devices. Therefore, proper understanding of the performance of such device is important for their application in ion sources. The present work aimed at providing a more detailed description of the oscillator system and operational characteristics of a self-excited push-pull oscillator using twin beam-power tetrode, constructed for operation at around 100 MHz.

CHAPTER 2

ENTRANCE CHANNEL EFFECTS ON THE DECAY OF A COMPOUND NUCLEUS

2. ENTRANCE CHANNEL EFFECTS ON THE DECAY OF A COMPOUND NUCLEUS

2.1. Nuclear Models

In the present work, the compound nucleus formation cross sections in both the neutron and proton induced reactions are calculated using the nuclear reaction code TALYS-1.9 (Koning *et al.*, 2008). The simulation of nuclear reactions in this code involves neutrons, photons, protons, deuterons, tritons, ^{3}He- and alpha-particles, in the 1 keV - 200 MeV energy range and for target nuclides of mass 12 and heavier. The compound nuclear reaction calculations are done in the statistical Hauser-Feshbach formalism (Hauser and Feshbach, 1952) with the optical potentials developed by Koning and Delaroche (2003). Theoretical calculations for the neutron and proton induced reactions are performed for the same set of default nuclear models and model parameters in TALYS-1.9 from few MeV to 20 MeV incident energy in the steps of 1 MeV.

The nuclear models that are included in TALYS can generally be categorized into optical, direct, pre-equilibrium, compound and fission models, all driven by a comprehensive database of nuclear structure and model parameters.

2.1.1. Optical Models

The optical model has a significant impact on many branches of nuclear reaction physics. The central assumption of this model is that the complicated interaction between an incident particle and a nucleus can be represented by a complex mean-field potential, which divides the reaction flux into a part covering

shape elastic scattering and a part describing all competing non-elastic channels. Solving the Schrödinger equation with this complex potential yields a prediction for the basic observables, namely the elastic scattering angular distribution and analyzing power, the reaction and total cross sections and, for low neutron energies, the s- and p-wave strength functions (S_0,S_1) and the potential scattering radius (R). An important feature of a good optical model potential (OMP) is that it can be used to reliably predict these observables for energies and nuclides for which no measurements exist, while the ingredients of the model, either microscopic or phenomenological, are physically well-behaved (Koning and Delaroche, 2003).

The default optical model potentials (OMP) for neutrons and protons used in TALYS are the local and global parameterisations of Koning and Delaroche (2003).

The phenomenological OMP for nucleon-nucleus scattering, Y, is defined as:

$$Y(r,E) = -\varsigma_V(r,E) - i\Omega_V(r,E) - i\Omega_D(r,E) + \varsigma_{SO}(r,E).l.\sigma + i\Omega_{SO}(r,E).l.\sigma + \varsigma_C(r), \quad (2.1)$$

where $\varsigma_{V,SO}$ and $\Omega_{V,D,SO}$ are the real and imaginary components of the volume-central (*V*), surface-central (*D*) and spin-orbit (*SO*) potentials, respectively. *E* is the LAB energy of the incident particle in MeV. All components are separated in energy-dependent well depths, ς_V, Ω_V, Ω_D, ς_{SO}, and Ω_{SO}, and energy-independent radial parts *f*, namely

$$\varsigma_V(r,E) = \varsigma_V(E)\, f(r,R_V,a_V), \quad (2.2)$$

$$\Omega_V(r,E) = \Omega_V(E)\, f(r,R_V,a_V), \quad (2.3)$$

$$\Omega_D(r,E) = -4a_D\Omega_D(E)\frac{d}{dr} f(r,R_D,a_D), \quad (2.4)$$

$$\varsigma_{SO}(r,E) = \varsigma_{SO}(E)\left(\frac{\hbar}{m_\pi c}\right)^2 \frac{1}{r}\frac{d}{dr} f(r,R_{SO},a_{SO}), \quad (2.5)$$

$$\Omega_{SO}(r,E) = \Omega_{SO}(E)\left(\frac{\hbar}{m_\pi c}\right)^2 \frac{1}{r}\frac{d}{dr} f(r,R_{SO},a_{SO}), \quad (2.6)$$

The form factor $f(r,R_i,a_i)$ is given by

$$f(r,R_i,a_i) = (1 + exp[(r - R_i)/a_i])^{-1}, \quad (2.7)$$

where $R_i = r_i A^{1/3}$, A is the atomic mass number and a_i is the diffuseness parameter.

For charged projectiles, the Coulomb term ς_C is given by

$$\varsigma_C(r) = \frac{Zze^2}{2R_C}\left(3 - \frac{r^2}{R_C^2}\right), \quad \text{for } r \le R_C$$

$$= \frac{Zze^2}{r}, \quad \text{for } r \ge R_C \quad (2.8)$$

where Z and z is the charge of the target and projectile respectively, and $R_C = r_C A^{1/3}$ is the Coulomb radius.

The parameterization of optical model potential for either incident neutrons or protons is

$$\varsigma_V(E) = v_1\left[1 - v_2(E - E_f) + v_3(E - E_f)^2 - v_4(E - E_f)^3\right]$$

$$\Omega_V(E) = w_1 \frac{(E-E_f)^2}{(E-E_f)^2 + (w_2)^2}$$

r_V = constant

a_V = constant

$$\Omega_D(E) = d_1 \frac{(E-E_f)^2}{(E-E_f)^2 + (d_3)^2} exp[-d_2(E - E_f)]$$

r_D = constant

a_D = constant

$$\varsigma_{SO}(E) = v_{SO1} exp\left[-v_{SO2}\left(E - E_f\right)\right]$$

$$\Omega_{SO}(E) = w_{SO1} \frac{\left(E-E_f\right)^2}{\left(E-E_f\right)^2 + (w_{SO2})^2}$$

r_{SO} = constant

a_{SO} = constant

r_C = constant (2.9)

where $E_f = E_f^n = -\frac{1}{2}[S_n(Z,N) + S_n(Z,N+1)]$ and $E_f = E_f^p = -\frac{1}{2}\left[S_p(Z,N) + S_p(Z,N+1)\right]$ are the Fermi energy for neutrons and protons respectively in MeV, with S_n and S_p being the neutron and proton separation energies for a nucleus with proton number *Z* and neutron number *N*.

In general, all parameters appearing in Eq. (2.9) differ from nucleus to nucleus. When enough experimental scattering data of a certain nucleus is available, a so called local OMP can be constructed. TALYS retrieves all the parameters of these local OMPs automatically from the nuclear structure and model parameter database. If a local OMP parameterisation is not available in the database, the built-in global optical models are automatically used, which can be applied for any Z, A combination. A flag exists (the **localomp** keyword) to overrule the local OMP by the global OMP. All optical model parameters mentioned above can be adjusted.

2.1.2. Compound nuclear reactions

When a projectile is captured by the target nucleus, a highly excited nucleus, called compound nucleus, is formed which subsequently decays by emission of a particle or gamma. The compound nucleus has a total energy E^{tot} and a range of

values for the total spin J and parity Π. In such a picture, the following conservation laws need to be obeyed.

$$E_a + S_a = E_{a'} + E_x + S_{a'} = E^{tot} \quad (2.10)$$

$$S + I + l = s' + I' + l' = J \quad (2.11)$$

$$\pi_0\Pi_0(-1)^l = \pi_f\Pi_f(-1)^{l'} = \Pi \quad (2.12)$$

The compound nucleus formula for the binary cross section is given by

$$\sigma_{\alpha\alpha'}^{comp} = D^{comp}\frac{\pi}{k^2}\sum_{J=mod(I+s,1)}^{l_{max}+I+s}\sum_{\Pi=-1}^{1}\frac{2J+1}{(2I+a)(2s+1)}\sum_{j=|J-I|}^{J+I}\sum_{l=|j-s|}^{j+s}\sum_{j'=|J-I'|}^{J+I'}\sum_{l'=|j'-s'|}^{j'+s'} \times \delta_\pi(\alpha)\delta_\pi(\alpha')\frac{T_{\alpha lj}^J(E_a)\langle T_{\alpha' l' j'}^J(E_{a'})\rangle}{\sum_{\alpha,l,j''}\delta_\pi(\alpha'')\langle T_{\alpha'' l'' j''}^J(E_{a''})\rangle}W_{\alpha lj\alpha' l' j'}^J, \quad (2.13)$$

where E_a = projectile energy

s = spin of the projectile

π_0 = parity of the projectile

l = orbital angular momentum of the projectile

j = total angular momentum of the projectile

$\delta_\pi(\alpha)$ = 1, if $(-1)^l\pi_0\Pi_0 = \Pi$ and 0 otherwise

α = channel designation of the initial system of projectile and target nucleus:

$\alpha = \{a, s, E_a, E_x^0, I, \Pi_0\}$, where a is the projectile type and E_x^0 the excitation energy of the target nucleus (usually zero).

l_{max} = maximum l-value for projectile

S_a = separation energy

$E_{a'}$ = ejectile energy

s' = spin of the ejectile

π_f = parity of the ejectile

l' = orbital angular momentum of the ejectile

j' = total angular momentum of the ejectile

$\delta_\pi(\alpha')$ = 1, if $(-1)^{l'}\pi_f \Pi_f = \Pi$ and 0 otherwise

α' = channel designation of the final system of ejectile and residual nucleus:

$\alpha' = \{a', s', E_{a'}, E_x, I', \Pi_f\}$, where a' is the ejectile type, E_x the excitation energy of the residual nucleus

I = spin of the target nucleus

Π_0 = parity of the target

I' = spin of the residual nucleus

Π_f = parity of the residual nucleus

Π = parity of the compound system

J = total angular momentum of the compound system

D^{comp} = depletion factor to account for direct and pre-equilibrium effects

k = wave number of relative motion

T = transmission coefficient

W = width fluctuation correction (WFC) factor.

For α' channels in which E_x is in the continuum, the effective transmission coefficient for an excitation energy bin with width ΔE_x is

$$\langle T^J_{\alpha' l' j'}(E_{\alpha'})\rangle = \int_{E_x-\frac{1}{2}\Delta E_x}^{E_x+\frac{1}{2}\Delta E_x} d\,E_{x'}\rho(E_{x'}, J, \Pi) T^J_{\alpha' l' j'}(E_{\alpha'}), \qquad (2.14)$$

where ρ is the level density and T is evaluated at an emission energy $E_{a'}$ that corresponds to the middle of the excitation energy bin, i.e. $E_{a'} = E^{tot} - E_x - S_{a'}$. Hence, both transitions to discrete states and transitions to the whole accessible continuum are covered by the sum over α′ in Eq. (2.13). The normalization factor D^{comp} is

$$D^{comp} = \left[\sigma_{reac} - \sigma^{disc,direct} - \sigma^{PE}\right]/\sigma_{reac} , \qquad (2.15)$$

For the angle-integrated compound cross section, instead of performing the full calculation, Eq. (2.13) can be decoupled into two parts that represent the incoming and outgoing reaction flux, respectively. It simplifies to

$$\sigma_{\alpha\alpha'}^{comp} = \sum_{J=mod(I+s,1)}^{l_{max}+I+s} \sum_{\Pi=-1}^{1} \sigma_{J\Pi}^{CF}(E^{tot}) \frac{\Gamma_{\alpha'}(E^{tot},J,\Pi \to E_x,I',\Pi_f)}{\Gamma^{tot}(E^{tot},J,\Pi)} , \qquad (2.16)$$

where $\sigma_{J\Pi}^{CF}$ is the compound formation cross section per spin and parity given by

$$\sigma_{J\Pi}^{CF}(E^{tot}) = D^{comp} \frac{\pi}{k^2} \frac{2J+1}{(2I+1)(2s+1)} \sum_{j=|J-I|}^{J+I} \sum_{l=|j-s|}^{j+s} T_{\alpha lj}^{J}(E_a)\delta_{\pi}(\alpha) , \qquad (2.17)$$

2.1.2.1. Width fluctuation correction factor

The Eq. (2.13) show that the width fluctuation correction factors depend on all the angular momentum quantum numbers involved, and thus has to be re-evaluated each time inside all the summations. The Eq. (2.13) is needed for relatively low incident energy, where the WFC has a significant impact and where the compound nucleus cross section to each individual discrete state is large enough to make its angular distribution of interest. For projectile energies above several MeV

(we generally take the neutron separation energy for safety), the width fluctuations have disappeared, meaning that $W^{J}_{\alpha l j \alpha' l' j'} = 1$ for all channels.

The WFC factor *W* accounts for the correlations that exist between the incident and outgoing waves. Above a few MeV of projectile energy, when many competing channels are open, the WFC factor can be neglected and the simple Hauser-Feshbach model is adequate to describe the compound nucleus decay.

Defining $a = \{\alpha, l, j\}$ and $b = \{\alpha', l', j'\}$, the compound nucleus cross section can be written in the compact form

$$\sigma_{ab} = \frac{\pi}{k_a^2} \frac{T_a T_b}{\sum_c T_c} W_{ab} \,, \qquad (2.18)$$

Theoretical calculations are also carried out with and without width fluctuation corrections. However, we do not observe difference in the results with and without width fluctuation corrections in the energy ranged considered.

2.1.3. Level densities

The nuclear level density is an important physical quantity in the statistical calculation of compound nuclear decay and therefore, useful for both pure and applied research. It is a fundamental property of the atomic nucleus defined as the number of energy levels per unit energy at excitation energy E_x. Together with the optical model potential, a correct level density is perhaps the most crucial ingredient for a reliable theoretical analysis of cross sections, spectra, angular distributions, and other nuclear reaction observables. This is one of the reasons why level densities have been thoroughly studied in the past and the existing literature on the subject

consists of panoply of models ranging from microscopic level densities that are directly obtained from combinatorial methods and Hartree–Fock approaches to phenomenological analytical expressions (Koning *et al.*, 2008). In the latest version of Talys, i.e. Talys-1.9, there are six different level density models. A good reason to provide more than one level density model is that while no single model is the most appropriate for all nuclides, having various approaches that are all assumed to be more or less reliable offer the possibility to do sensitivity and uncertainty analyses of nuclear reaction calculations.

The analytical expression of level density is factorized as follows

$$\rho(E_x, J, \Pi) = P(E_x, J, \Pi)\, R(E_x, J)\, \rho^{tot}(E_x), \quad (2.19)$$

where $P(E_x, J, \Pi)$ is the parity distribution, $R(E_x, J)$ the spin distribution and $\rho^{tot}(E_x) = \sum_J \sum_\Pi \rho(E_x, J, \Pi)$ is the total level density which corresponds to the total number of levels per MeV around E_x.

2.1.3.1. The Constant Temperature Model (LDM-1)

In the Constant Temperature Model (CTM) (Gilbert and Cameron, 1965), the excitation energy range is divided into two:

(i) A low energy part from 0 MeV up to a matching energy E_M, where the so-called constant temperature law applies, and

(ii) A high energy part above E_M, where the Fermi gas model applies.

Hence, for the total level density we have

$$\rho^{tot}_{CTM}(E_x) = \rho^{tot}_T(E_x), \quad \text{if } E_x \le E_M$$
$$= \rho^{tot}_F(E_x), \quad \text{if } E_x > E_M \quad (2.20)$$

and for the level density

$$\rho_{CTM}(E_x, J, \Pi) = \frac{1}{2} R_F(E_x, J) \rho_T^{tot}(E_x), \qquad \text{if } E_x \leq E_M$$

$$= \rho_F(E_x, J, \Pi), \qquad \text{if } E_x > E_M \tag{2.21}$$

where $R_F(E_x, J) = \frac{2J+1}{2\sigma^2} exp\left[-\frac{\left(J+\frac{1}{2}\right)^2}{2\sigma^2}\right]$ is the Fermi gas spin distribution and σ^2 is the spin cut-off parameter, which represents the width of the angular momentum distribution and is given by

$$\sigma^2(E_x) = \sigma_d^2, \qquad \text{for } 0 \leq E_x \leq E_d$$

$$= \sigma_d^2 + \frac{E_x - E_d}{S_n - E_d}(\sigma_F^2(E_x) - \sigma_d^2), \qquad \text{for } E_d \leq E_x \leq S_n$$

$$= \sigma_d^2 \qquad \text{for } E_x \geq S_n \tag{2.22}$$

The Fermi gas level density of Eq. (2.21) is

$$\rho_F(E_x, J, \Pi) = \frac{1}{2} \frac{2J+1}{2\sqrt{2\pi}\sigma^3} exp\left[-\frac{\left(J+\frac{1}{2}\right)^2}{2\sigma^2}\right] \frac{\sqrt{\pi}}{12} \frac{exp\left[2\sqrt{aU}\right]}{a^{1/4} U^{5/4}}, \tag{2.23}$$

where the first factor 1/2 represents the equiparity distribution, a is the level density parameter and $U = E_x - \Delta^{CTM}$ is the effective excitation energy in which the energy shift is given by

$$\Delta^{CTM} = \chi \frac{12}{\sqrt{A}} \tag{2.24}$$

with χ = 0, for odd – odd,

= 1, for odd – even,

= 2, for even – even, (2.25)

2.1.3.2. The Back-shifted Fermi gas Model (LDM-2)

The expression for the total Back-shifted Fermi gas Model (BFM) level density is

$$\rho_{BFM}^{tot}(E_x) = \left[\frac{1}{\rho_F^{tot}(E_x)} + \frac{1}{\rho_0(t)}\right]^{-1}, \quad (2.26)$$

In the above equation, for the total level density, the pairing energy is treated as an adjustable parameter and the Fermi gas expression is used all the way down to 0 MeV given by

$$\rho_F^{tot}(E_x) = \frac{1}{\sqrt{2\pi}\sigma}\frac{\sqrt{\pi}}{12}\frac{exp\left[2\sqrt{aU}\right]}{a^{1/4}U^{5/4}}, \quad (2.27)$$

where $U = E_x - \Delta^{BFM}$ is the effective excitation energy with energy shift given by

$$\Delta^{BFM} = \chi\frac{12}{\sqrt{A}} + \delta, \quad (2.28)$$

where $\chi = -1$, for odd − odd,

$= 0$, for odd − even,

$= 1$, for even – even.

and δ is an adjustable parameter to fit experimental data per nucleus.

And, ρ_0 of Eq. (2.26) is given by

$$\rho_0(t) = \frac{exp(1)}{24\sigma}\frac{\left(a_n + a_p\right)^2}{\sqrt{a_n a_p}}exp\left(4a_n a_p t^2\right), \quad (2.29)$$

where $a_n = a_p = a/2$ and $t = \sqrt{\frac{U}{a}}$.

Hence, with the two adjustable parameters a and δ, and the inclusion of spin distribution, Back-shifted Fermi gas Model (BFM) level density is

$$\rho_{BFM}(E_x, J, \Pi) = \frac{1}{2}\frac{2J+1}{2\sigma^2}exp\left[-\frac{\left(J+\frac{1}{2}\right)^2}{2\sigma^2}\right]\rho_{BFM}^{tot}(E_x), \quad (2.30)$$

2.1.3.3. The Generalized Superfluid Model (LDM-3)

In the Generalized Superfluid Model (GSM), the total level density has two forms: one below and one above the critical energy U_c. The general formula for the total level density according to the Fermi Gas Model is given by

$$\rho_F^{tot}(E_x) = \frac{1}{\sqrt{2\pi}\sigma}\frac{e^S}{\sqrt{D}}, \tag{2.31}$$

(i) For energies below U_c, i.e. $U' \leq U_c$, the total level density is given by

$$\rho_{GSM}^{tot}(E_x) = \frac{1}{\sqrt{2\pi}\sigma}\frac{e^S}{\sqrt{D}}, \tag{2.32}$$

and the level density is

$$\rho_{GSM}(E_x, J, \Pi) = \frac{1}{2}R_F(E_x, J)\rho_{GSM}^{tot}(E_x), \tag{2.33}$$

where the critical energy is $U_c = a_c T_c^2 + E_{cond.}$, (2.34)

and the critical temperature is $T_c = 0.567\ \Delta_0$, (2.35)

Here, the pairing correlation function is given by

$$\Delta_0 = \frac{12}{\sqrt{A}}, \tag{2.36}$$

The condensation energy $E_{cond.}$, which characterizes the decrease of the superfluid phase relative to the Fermi gas phase, is given by the expression

$$E_{cond.} = \frac{3}{2\pi^2}a_c\Delta_0^2, \tag{2.37}$$

where the critical level density parameter ac is given by the iterative equation

$$a_c = \tilde{a}\left[1 + \delta W\frac{1-exp(-\gamma a_c T_c^2)}{a_c T_c^2}\right], \tag{2.38}$$

The entropy S is defined as

$$S = S_c\frac{T_c}{T}(1-\varphi^2) = S_c\frac{T_c}{T}\frac{U\prime}{U_c}, \tag{2.39}$$

where $S_c = 2\ a_c\ T_c$ is the critical entropy and $\varphi^2 = 1 - \frac{U\prime}{U_c}$.

The determinant D is expressed as

$$D = D_c(1-\varphi^2)(1+\varphi^2)^2 = D_c\frac{U\prime}{U_c}\left(2-\frac{U\prime}{U_c}\right)^2, \quad (2.40)$$

where $D_c = \frac{144}{\pi}a_c^3 T_c^5$ is the critical determinant.

The spin cut-off parameter is given by

$$\sigma^2 = \sigma_c^2(1-\varphi^2) = \sigma_c^2\frac{U\prime}{U_c}, \quad (2.41)$$

where $\sigma_c^2 = 0.01389A^{5/3}\frac{a_c}{\tilde{a}}T_c$ is the critical spin cut-off parameter.

The Fermi gas spin distribution is given by

$$R_F(E_x,J) = \frac{2J+1}{2\sigma^2}exp\left[-\frac{\left(J+\frac{1}{2}\right)^2}{2\sigma^2}\right], \quad (2.42)$$

(ii) For energies above U_c, i.e. $U' \geq U_c$, the total level density is given by

$$\rho_{GSM}^{tot}(E_x) = \frac{1}{\sqrt{2\pi}\sigma}\frac{\sqrt{\pi}}{12}\frac{exp[2\sqrt{aU}]}{a^{1/4}U^{5/4}}, \quad (2.43)$$

And the level density is given by

$$\rho_{GSM}(E_x,J,\Pi) = \frac{1}{2}R_F(E_x,J)\rho_{GSM}^{tot}(E_x), \quad (2.44)$$

where $U = E_x - \Delta^{GSM}$ is the effective excitation energy, with the energy shift given by

$$\Delta^{GSM} = E_{cond.} - \chi\Delta_0 - \delta, \quad (2.45)$$

and the spin cut-off parameter in the high-energy region is

$$\sigma^2 = I_0\frac{a}{\tilde{a}}\sqrt{\frac{U}{a}}, \quad (2.46)$$

Finally, in the Generalized Superfluid Model (GSM), the adjustable parameters are a and δ.

2.1.3.4. The microscopic level densities (Skyrme force) from Goriely's tables (LDM-4)

The previous three level density models are based on phenomenological approaches. Although the analytical level density formulae are still routinely used in nuclear reaction calculations, microscopic approaches are obviously to be preferred, and the combination of advances in theoretical nuclear physics and dramatically increased computer power has indeed led to very promising results (Koning *et al., 2008*). Therefore, for incident energies up to 150 MeV and spin values up to *J = 30*, there is an option to employ the nuclear level densities in tabular format which are calculated by S. Goriely on the basis of Hartree-Fock calculations.

2.1.3.5. The microscopic level densities (Skyrme force) from Hilaire's combinatorial tables (LDM-5)

Apart from the Goriely's table, level densities for more than 8500 nuclei are available in tabular format (Capote *et al.*, 2009), for excitation energies up to 200 MeV and for spin values up to J = 49. These level densities are used with **ldmodel 5**.

2.1.3.6. The microscopic level densities (temperature dependent Hartree-Fock-Bolyubov, Gogny force) from Hilaire's combinatorial tables (LDM-6)

Since the above two microscopic level densities referred as 'LDM-4' and 'LDM-5' have not been adjusted to experimental data, adjustment flexibility is added through a scaling function to the microscopic level densities. Therefore, the level density becomes

$$\rho(E_x, J, \Pi) = exp\left(c\sqrt{E_x - \delta}\right)\rho_{HFM}(E_x - \delta, J, \Pi), \qquad (2.47)$$

where δ is the pairing shift which simply implies the level density at different energy, the constant *c* is more or less similar to the level density parameter *a* of the

phenomenological models. By default, δ and *c* are both zero which is the case when these two values are not altered. Adjusting δ and c together gives adjustment flexibility at both low and higher energies, so that both discrete levels and experimental mean resonance spacings can be reproduced as good as possible.

2.2. Theoretical framework

According to the compound nucleus theory, the decay of the compound nucleus is independent of how it is formed. However, it is known that due to the different J^{π} distributions of the compound nuclei formed by different entrance channels, a particle decay probabilities can be very different. In this work, we investigate how the J^{π} distributions of the compound nuclei formed by the neutron induced and proton induced reactions influence the alpha decay channel for the reactions mentioned above.

In the Weisskopf-Ewing(WE) limit of the Hauser-Feshbach compound nucleus theory, it is assumed that the decay branching ratios are independent of the compound nucleus angular momentum and parity (Hauser and Feshbach, 1952). We can therefore write the expression for the neutron induced reaction cross section referred here as 'reference' by

$$\sigma_{n\alpha}(E_n) = \sigma_n^{CN}(E^*)G_{\alpha}(E^*) \qquad (2.48)$$

where $\sigma_n^{CN}(E^*) = \sum_{J^{\pi}} \sigma_n^{CN}(E^*, J^{\pi})$ is the compound nucleus formation cross section at the excitation energy E^* in the neutron induced reaction which can be calculated easily with a suitable optical potential, and $G_{\alpha}(E^*)$ is the alpha branching ratio of the compound nucleus produced by neutron induced reaction.

Similarly, the proton induced reaction which produced the same compound nucleus at the same excitation energy, and decay into the same outgoing channel as the neutron induced reaction can also be expressed as

$$\sigma_{p\alpha}(E_p) = \sigma_p^{CN}(E^*)G'_\alpha(E^*) \tag{2.49}$$

where $\sigma_p^{CN}(E^*) = \sum_{J^\pi} \sigma_p^{CN}(E^*, J^\pi)$ is the compound nucleus formation cross section in the proton induced reaction which can also be calculated easily with a suitable optical potential, and $G'_\alpha(E^*)$ is the alpha branching ratio of the compound nucleus produced by proton induced reaction.

The kinetic energy of the particle E_i is related to the excitation energy of the compound nucleus E^*, via

$$E^* = E_i + S_i \tag{2.50}$$

where $\boldsymbol{E^*}$ is the compound nucleus excitation energy that has been reached in the case of the neutron induced reaction, A_p is the mass of proton, A is the mass of the target nucleus and S_p is the separation energy of proton from the compound nucleus. The proton energy can be converted into its equivalent neutron energy using equation (2.50).

In the WE limit, the branching ratios in Eq. (2.48) and Eq. (2.49) are similar, which is experimentally measurable alpha decay probability from the proton induced reaction. Hence, we can write the decay probability as

$$P^{decay}(E^*) = G_\alpha(E^*) = G'_\alpha(E^*) \tag{2.51}$$

By utilizing Eq. (2.51), the neutron induced reaction cross section can be extracted by using the proton induced reaction referred as 'extracted' by

$$\sigma'_{n\alpha}(E_n) = \sigma_n^{CN}(E^*)G'_\alpha(E^*) \tag{2.52}$$

where symbols have their usual meanings.

If the neutron induced cross section given by Eq. (2.48) is taken as reference, and under the Hauser-Feshbach formalism of compound nucleus reaction calculation with the valid assumption of the WE limit, this reference cross section should be the same as the extracted (n,α) cross section from the proton induced reaction using Eq. (2.51).

For the reactions considered in the present work, since the preequilibrium contributions are significant especially above 7 MeV incident energy, their contributions have to be taken into account. Escher *et al.* (2012) suggested that the best way to account for the missing preequilibrium contribution is to perform model calculations of the reference reaction with ($\sigma_{n\alpha}^{CN+PE}$) and without ($\sigma_{n\alpha}^{CN}$) preequilibrium, and to multiply the ratio of the two model calculations with the cross sections extracted using Eq. (2.52). This can be implemented by extending Eq. (4) as follows

$$\sigma'_{n\alpha}(E_n) = \sigma_n^{CN}(E^*)G'_\alpha(E^*)R \tag{2.53}$$

where $R = \frac{\sigma_{n\alpha}^{CN+PE}}{\sigma_{n\alpha}^{CN}}$ and other symbols have their usual meanings as in Eq. (2.52).

There are eight different options for the γ-ray strength function in TALYS-1.8 and their sensitivity has been studied. In general, most of these options are based

on the work of Kopecky and Uhl (Kopecky and Uhl, 1990), or Brink (Brink, 1957) and Axel (Axel, 1962). The eight different Photon Strength Functions are listed below:

(1) Photon Strength Function 1(PSF-1): Kopecky-Uhl generalized Lorentzian (Kopecky and Uhl, 1990).

(2) Photon Strength Function 2(PSF-2): Brink (Brink, 1957) and Axel Lorentzian (Axel, 1962).

(3) Photon Strength Function 3(PSF-3): Hartree-Fock BCS tables (Capote et al., 2009).

(4) Photon Strength Function 4(PSF-4): Hartree-Fock-Bogolyubov tables (Capote et al., 2009).

(5) Photon Strength Function 5(PSF-5): Goriely's hybrid model (Goriely, 1998).

(6) Photon Strength Function 6(PSF-6): Goriely temperature-dependent Hartree-Fock-Bogolyubov.

(7) Photon Strength Function 7(PSF-7): Temperature-dependent relativistic mean field.

(8) Photon Strength Function 8(PSF-8): Gogny D1M Hartree-Fock-Bogolyubov+QRPA.

Theoretical calculations are also carried out with and without width fluctuation corrections. However, we do not observe difference in the results with and without width fluctuation corrections in the energy ranged considered.

CHAPTER 3

CONSTRUCTION AND CHARACTERIZATION OF AN RF OSCILLATOR

3. CONSTRUCTION AND CHARACTERIZATION OF AN RF OSCILLATOR

3.1. Introduction

This chapter consists of a detail description in the design of the RF oscillator adopted in the present work. In Section 3.2, the complete circuit diagram of the present RF oscillator is shown. Each of the associated parts comprising the RF oscillator is characterized in the present work. The different parts of the oscillator are described in the succeeding sections from Section 3.2.1 to 3.2.5.

As discussed in the importance of power measurement in Chapter 1, the reliable and inexpensive power measurement technique is required for better maintenance of the RF ion sources. Different techniques for measuring the RF power were investigated in this work. The detail description of two of the most simple and reliable power measurement techniques and their flaws are presented in Section 3.3.

3.2. Circuit Description

Schematic circuit diagram of an RF oscillator used in the present study is shown in Figure 3.1. The present RF oscillator follows the design used in an Oak Ridge type ion source reported by Moak *et al.*, 1951, and works on the principle of a push pull amplifier.

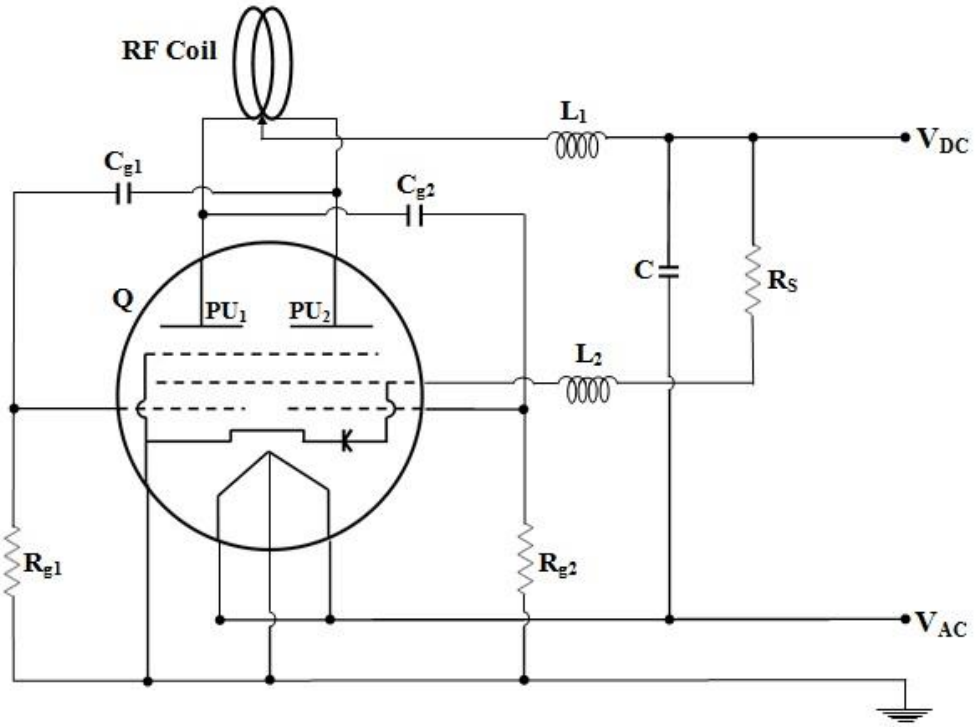

Figure 3.1: Circuit diagram of RF oscillator. Q = 829B twin beam-power tetrode; RF Coil: tube diameter = 0.6 cm, pitch = 1 cm, coil diameter = 7 cm; R_S = 20 kΩ, 20 W; $R_{g1} = R_{g2}$ = 6.8 kΩ, 1 W; $C_{g1} = C_{g2}$ = 1 pF, 1 kV; C = 50 μF, L_1= 586 μH; L_2= 589.5 μH.

3.2.1. Power supply

DC power supply for the tube is obtained from a full-wave rectifier with center-tapped 230V to 1kV step-up transformer and RC filtering circuit as shown in Figure 3.2. The necessary biasing DC voltage is also supplied to the screen grid via a resistor 'R_S' (20 kΩ, 20 W). Low wattage below 15 W results in excessive heating of the screen grid resistor, and thus changing the resistance value and operating point of the tube. Separate ac supply of proper voltage is employed to heat the filament. The applied plate voltage of the tube can be varied using a Variac (0-270 V) connected at the input of the step-up transformer.

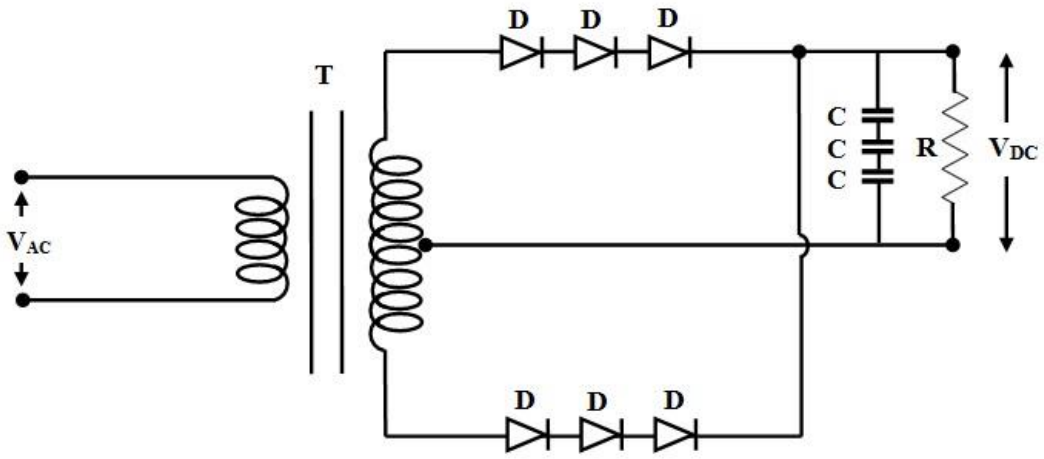

Figure 3.2: Circuit diagram of 1 kV DC power supply. T = 100 VA Step-Up Transformer; D = IN 4007, 700 V (PIV); C = 330 µF, 450 V; R = 1.18 MΩ.

3.2.2. Amplifier

The amplifying stage of the oscillator is a vacuum tube connected in push-pull arrangement with capacitive coupling to the control grid. Vacuum tube is an electronic device that controls the flow of electrons in a vacuum. It is also called electron tube or a valve. It is a device used to amplify electronic signal. A vacuum tube consists of a cathode (also called filament) that emits free electrons, anode (also called plate) that collects the electrons emitted by the Cathode and the grid that controls the flow of electrons or electric current between Anode and Cathode. The vacuum tube used in this study is an 829B Twin Beam Power Tube.

The schematic diagram of a pentode valve and the photographic image of an 829B twin beam power tube are shown in Figure 3.3 (a) and (b).

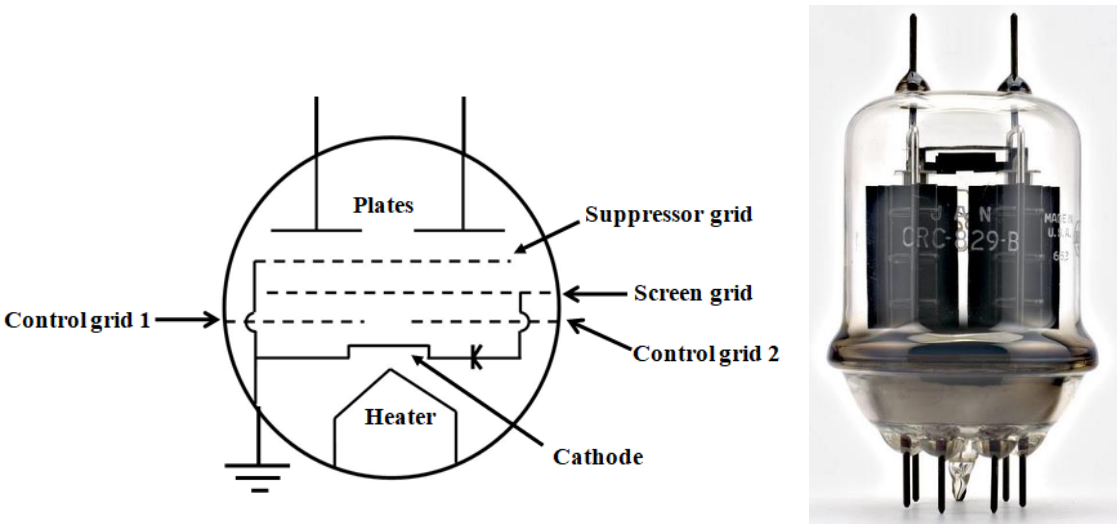

(a) (b)

Figure 3.3: (a) Schematic diagram of pentode, (b) Photograph image of 829B power tube.

3.2.3. RF Choke

Radio Frequency Choke (R.F.C) is a basic inductor used to choke the Radio frequencies. This kind of inductor will allow DC current to pass through but blocks AC current in the radio frequency range. The choke circuits are low pass filters because they choke out high frequencies and pass the lower frequencies. L_1, L_2 and C of Figure 3.1 are the RF chokes and capacitor to prevent the dc source from RF signal interference.

3.2.4. RF Coil

The LC frequency selector or RF coil or Tank circuit is the most important part of the RF oscillator. It is used as an antenna for transmission of the generated RF signal. The RF coil is basically an inductor and a capacitor connected in parallel.

Initially the capacitor is charged to some voltage. Then the capacitor C will start discharging through inductor L. The voltage across capacitor will start to decrease and the current through the inductor starts increasing. The increasing current creates an electromagnetic field around the coil and when the capacitor is fully discharged the electrostatic energy stored in the capacitor will be fully transferred into the coil as electromagnetic field. With no more energy in the capacitor to sustain the current through the coil, the field around the coil starts to fall and the current through the coil tends to decrease. Due to electromagnetic induction, the inductor will generate a back emf equal to L(di/dt) in order to oppose the change in current. This back emf will charge the capacitor again.

When the capacitor is fully charged, the energy stored in the inductor as electromagnetic field will be moved to the capacitor as electric field. Then the

capacitor starts discharging again and the cycle is repeated. This cyclic transfer of energy between the capacitor and inductor is the reason behind the production of oscillation in the tank circuit. Hence, the oscillation frequency of the oscillator is primarily determined by the resonance frequency of the RF coil forming LC tank circuit and is given by

$$f = 1/2\pi\sqrt{(LC)}, \qquad (3.1)$$

The inductance 'L' and capacitance 'C' of equation (3.1) are dependent factors which are basically determined by the dimension of the tank circuit. The schematic diagram of the RF coil used in the present study is shown in Figure 3.4. It is made of copper tubing winded into two turns of coil. The parasitic or stray capacitance between the windings serves as the capacitive part of the LC tank circuit. The inductance and other parameter of the RF coil are calculated using a web-based calculator employing current-sheet coil geometrical formula (Corum *et al.*, 2001) available at http://www.hamwaves.com/antennas/inductance.html corrected for field non-uniformity and round wire.

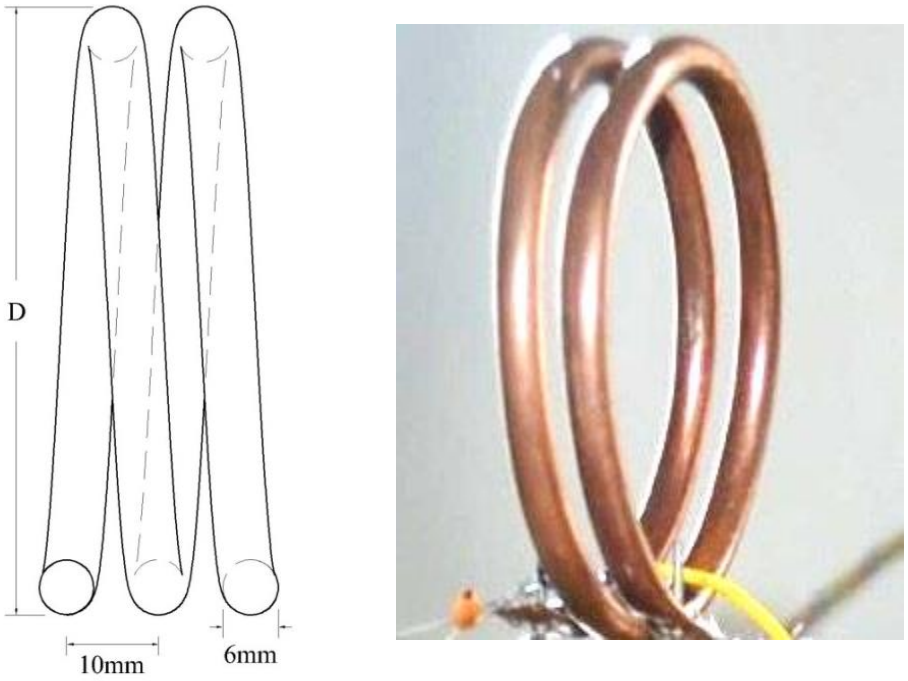

Figure 3.4: A photograph and schematic diagram of RF coil

3.2.5. Push-pull Amplifier and operation of a push-pull oscillator

Push-Pull Amplifier is a power amplifier which is used to supply high power to the load. It consists of two amplifying stages. One of the amplifying stages pushes the output on positive half cycle and the other pulls on negative half cycle; this is why it is known as Push-Pull Amplifier. The basic operation of a push-pull oscillator can be described briefly as explained below.

When a random voltage fluctuation makes the grid of P_{U1} (see Fig. 3.1) positive, it makes the grid of P_{U2} negative. These cause changes in the plate current. Resonated by the tank coil in the plate circuit, they cause voltage changes on the plate which, fed through the plate to grid capacitance, reverse the polarity of the

grids. This continues, the tank circuit strengthens the voltage changes of the grids and plates, so that strong oscillations are developed.

In addition to the fact that the two tubes are operating to give greater power, the symmetry of the circuit makes it particularly suitable for use at ultra high frequencies.

3.2.6. Grid leak resistors and capacitors

The grid leak resistors and the capacitors are used for switching the two amplifying stages of the tube. The grid leak resistors R_{g1} and R_{g2} each of resistances 22 kΩ are connected between the control grids and ground, to which both the cathodes are also connected. The plates and control grids are connected cross-wise by coupling capacitors of capacitance 1pF. The grid leak resistors together with coupling capacitors provide the necessary biasing to the control grid. This combination forms an astable multi-vibrator circuit, which has no stable state and the output is continuously oscillating between the two unstable stages. It automatically and continuously goes on triggering itself internally. The time period of each state is determined by the RC time constant.

The plate resistances of the tube in the fully conducting state and the internal grid resistances at zero or positive grid-to-cathode potential are very small compared with the external resistances in the plate and grid circuits. Furthermore, it is assumed that the influence of the stray capacitances of the valve electrodes and the wiring, which shunt the resistances and can have considerable effects on the wave shape of the relaxation signal at high frequencies, is negligible. More precisely, this means

that the time constants containing these stray capacitances are very small compared with the period and time of rise of the relaxation signal.

With these assumptions, the multivibrator action may be described as a switching device that changes the two amplifying stages of the valve alternately from the conducting into the non-conducting state in a switching time that is negligibly small compared with the total period of the relaxation signal which results from this switching action. Then, during one half of the total period of the multivibrator signal, one of the amplifying stages, say Unit No. 1 (U_1), is conducting; the other stage, Unit No. 2 (U_2), is cut off. During the second half of the period, the reverse process holds, namely U_1 is cut off and U_2 is conducting.

The oscillator is naturally air cooled during operation and the frequency of the RF signal is directly measured with frequency counter FC 2400. Conventional digital multimeters are used to measure voltage and current.

3.3. RF Power measurement

3.2.1 Modified form of Photometric Method

The experimental setup for RF power measurement is shown in Figure 3.5. The method is based on the ability of incandescent light bulb to convert RF power directly into heat and light. The setup consists of an ordinary 100 Watt, 230 V light bulb ‘B’ directly coupled to the RF tank coil using two parallel open wires of length 50 cm. Light emitted by the incandescent lamp is detected with a cadmium sulphide LDR (light-dependent resistor) photometer. For all measurements, LDR is kept at distance of 5 cm from the center of the bulb and V_{LDR} is fixed at 7 V. To achieve

impedance matching between the source and the load, the positions of the two output tapping points in the RF coil are adjusted till maximum LDR current reading is indicated by the ammeter. With 100 watt light bulb load, impedance matching is observed at 1/3 of the coil center tapped point.

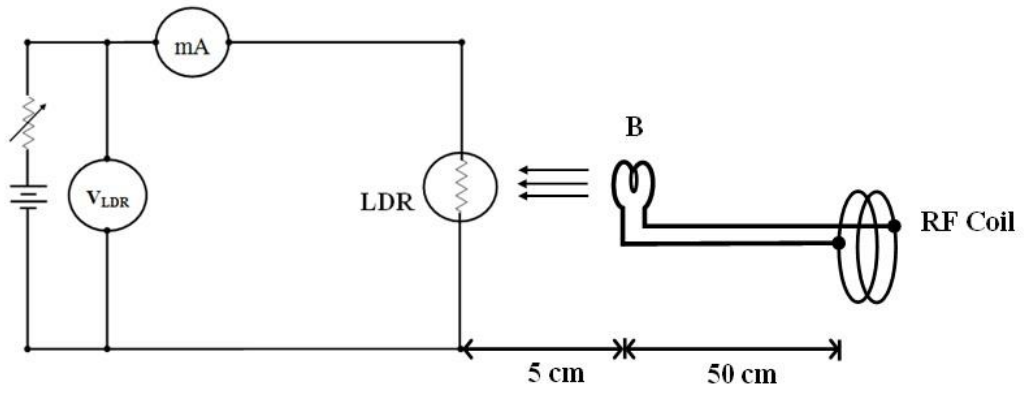

Figure 3.5: Experimental setup for photometric method of RF power measurement.

The LDR current reading at different light intensity is next calibrated into power with standard 50 Hz AC source using the following relation

$$P = VI \qquad (3.2)$$

In the calibration process, the transmitter is replaced by a variable standard ac source and the brightness of the bulb is adjusted to give LDR current reading equal to that recorded with RF power. With this modified form of photometric method the relative RF output power can be obtained at a more precise level.

However, the filament of incandescent lamp is coiled coil in structure and as a result the power value indicated by this measurement method will not be same if the load is purely resistive. To estimate the amount of power attenuated by the filament, inductors of different inductances are connected in series with a 100 watt light bulb in a 50 Hz AC circuit, and the variation of AC power with inductive reactance is first studied at different applied voltage. The inductance of the external inductors used in

this study varies from 14 mH to 415 mH according to direct measurement with Fluke PM6303A RCL meter at 1 kHz. From the relationship between inductive reactance and power delivered to the load, the amount of RF power attenuated by the filament reactance can be calculated as explained in Section 3.2.

The inductance of the filament is calculated from its physical dimension using Lundin's formula (Lundin *et al.*, 1985) as the 1 kHz RCL meter cannot be used for direct measurement. Following are the dimension of the filament obtained with a travelling microscope (VC = 0.001): length = 35 mm; bigger coil diameter = 0.8 mm (outer), pitch = 0.27 mm; smaller coil diameter = 0.12 mm; filament wire thickness = 0.05 mm; number of turns (bigger coil) = 96; number of smaller coil turns in the bigger coil = 22.

All power measurements using photometric method are conducted in a dark room to avoid interference from background light. Each measurement was repeated at least three times to check the consistency in our results and the maximum uncertainty in power measurement is calculated to be about 2%.

3.2.2. Peak voltage detection method

In this method, the RF power is transferred to a purely resistive load of 50 ohm through a coaxial cable and the voltage developed across the load is detected with a high speed diode as shown in Figure 3.6. The diode rectifies the RF signal and converts it to a DC voltage, which can be read by a multimeter with good accuracy; the 1nF capacitor is there to smooth the rectified DC signal presented to the meter. The voltage thus measured corresponds to the peak RF voltage and related to the RF power by the equation

$$P = V_p^{\,2}/2R \text{ (watt)} \qquad (3.3)$$

where V_p= measured peak voltage + diode forward voltage drop which is 0.7 V for Silicon, and R is 50 ohms. The high speed diode used to detect and rectify RF signal is 1N4148 having reverse recovery time of 4 ns. The 50 ohm dummy load is constructed out of 20 number of 1k (1 watt) carbon resistors connected in parallel between two circular copper coated PCB. The whole unit is then immersed in paraffin oil to further increase the power handling capacity. No appreciable change in temperature of the paraffin oil was observed during operation. Peak voltage measurement cannot be performed beyond 800 V due to the interference of the digital voltage measuring device by the high field RF signal.

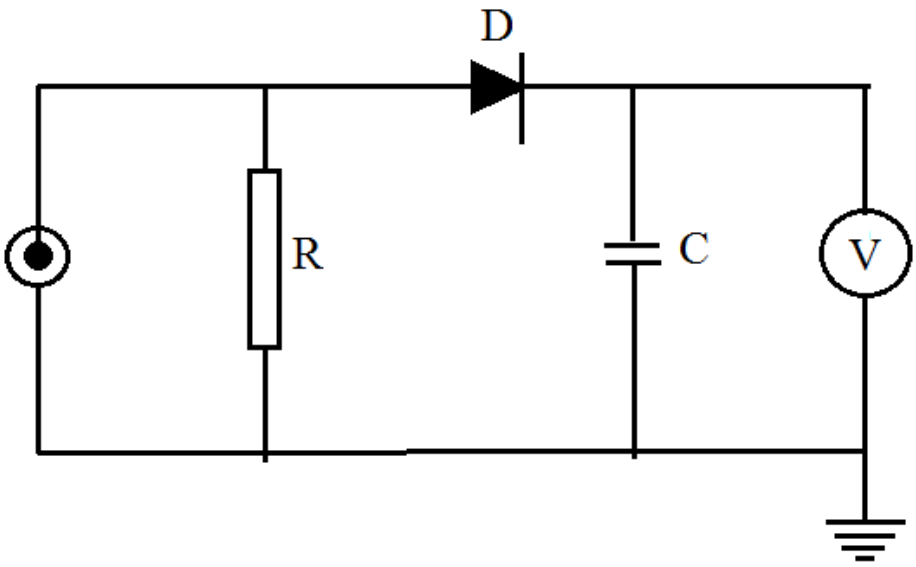

Figure 3.6: Circuit diagram for peak voltage measurement with diode detector and dummy load. (R = 50 ohm; D = 1N4148, 100V PIV; C = 1 µF).

CHAPTER 4

RESULTS AND DISCUSSION

4. RESULTS AND DISCUSSION

4.1. Introduction

In the first two sections of this chapter, a complete description on how the different entrance channel affects the decay probability is reported. Case studies for two particular reaction combinations are made. In particular, the alpha decay probability is observed for the two reactions in each case. In Section 4.2, the case study for a reaction combination of the $^{55}Mn(n,\alpha)^{52}V$ reaction and the $^{55}Cr(p,\alpha)^{52}V$ reaction is reported. The case study for the other reaction combination consisting of the $^{55}Fe(n,\alpha)^{52}Cr$ reaction and the $^{55}Mn(p,\alpha)^{52}Cr$ reaction is reported in Section 4.3.

The remaining part of this chapter contains the characterization of an RF oscillator on account of its application in the low energy charged particle accelerator and the power measurement techniques for the RF output power. In Section 4.4, the operating conditions of RF oscillator are discussed in detail. Section 4.5 contains a detail description on the techniques adopted for measuring the RF output power. The dependence of the operating frequency of the RF oscillator and hence the RF output power on the RF coil design is reported in Section 4.6.

4.2. The $^{55}Mn(n,\alpha)^{52}V$ reaction

In this case, the reaction of interest is the $^{55}Cr(p,\alpha)^{52}V$ reaction. As already discussed in Chapter 1, since the target ^{55}Cr is unstable, an alternative $^{55}Mn(n,\alpha)^{52}V$ reaction will be used to extract the $^{55}Cr(p,\alpha)^{52}V$ reaction cross section. Converting the proton energy to its equivalent neutron energy, the proton energy scale has been shifted by ~1.82 MeV with respect to the neutron energy scale. The important

physical information necessary for theoretical calculations between the reactions under considered are given in Table 4.1.

Figure 4.1 shows the neutron and proton transmission coefficients on ^{55}Mn and ^{55}Cr targets respectively calculated using local optical potential by Koning and Delaroche for several partial waves ranging from l = 0 to 9. The solid curves represent the neutron transmission coefficients on the ^{55}Mn target, and the dash lines are for the proton transmission coefficients on the ^{55}Cr target. The list of possible states of the J^{π} population of the compound nucleus ^{56}Mn formed via n+^{55}Mn and p+^{55}Cr are given in Table 4.2 and 4.3 respectively.

Table 4.1: General information of ^{55}Mn(n,α)^{52}V and ^{55}Cr(p,α)^{52}V reactions

Sl. No.	**Physical quantity**	**^{55}Mn(n,α)^{52}V**	**^{55}Cr(p,α)^{52}V**
1	Projectile spin (s)	0.5	0.5
2	Projectile parity	+1	+1
3	Projectile mass	1.00782503223 a.m.u.	1.008665 a.m.u.
4	Target spin (I)	2.5	1.5
5	Target parity	-1	-1
6	Target mass	54.93804391 a.m.u.	54.9408397 a.m.u.
7	Q-value	-0.62223MeV	1.19812 MeV
8	Separation Energy of projectile	7.27045 MeV	9.09080 MeV
9	Reaction Threshold	0.633 MeV	0

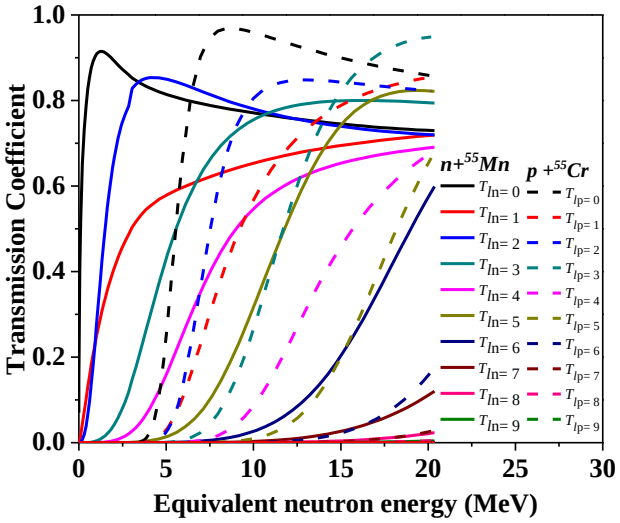

Figure 4.1: Transmission coefficients of neutron on ^{55}Mn and proton on ^{55}Cr.

Table 4.2: Possible J^{π} states of the compound nucleus ^{56}Mn formed via n + ^{55}Mn

l	**Designation**	**Spin and Parity of Projectile (neutron)** ***s***	**Spin of target (^{55}Mn)** ***I***	**Possible Spin and Parity of the Compound Nucleus (^{56}Mn)** ***J^{π}***
0	s	0.5^{+}	2.5^{-}	$2^{-}, 3^{-}$
1	p			$1^{+}, 2^{+}, 3^{+}, 4^{+}$
2	d			$0^{-}, 1^{-}, 2^{-}, 3^{-}, 4^{-}, 5^{-}$
3	f			$0^{+}, 1^{+}, 2^{+}, 3^{+}, 4^{+}, 5^{+}, 6^{+}$
4	g			$1^{-}, 2^{-}, 3^{-}, 4^{-}, 5^{-}, 6^{-}, 7^{-}$
5	h			$2^{+}, 3^{+}, 4^{+}, 5^{+}, 6^{+}, 7^{+}, 8^{+}$
6	i			$3^{+}, 4^{-}, 5^{-}, 6^{-}, 7^{-}, 8^{-}, 9^{-}$

Table 4.3: Possible J^{π} states of the compound nucleus ^{56}Mn formed via p + ^{55}Cr

l	**Designation**	**Spin and Parity of Projectile (proton)** ***s***	**Spin of target (^{55}Cr)** ***I***	**Possible Spin and Parity of the Compound Nucleus (^{56}Mn)** J^{π}
0	s	0.5^{+}	1.5^{-}	$1^{-}, 2^{-}$
1	p			$0^{+}, 1^{+}, 2^{+}, 3^{+}$
2	d			$0^{-}, 1^{-}, 2^{-}, 3^{-}, 4^{-}$
3	f			$1^{+}, 2^{+}, 3^{+}, 4^{+}, 5^{+}$
4	g			$2^{-}, 3^{-}, 4^{-}, 5^{-}, 6^{-}$
5	h			$3^{+}, 4^{+}, 5^{+}, 6^{+}, 7^{+}$
6	i			$4^{-}, 5^{-}, 6^{-}, 7^{-}, 8^{-}$

Fig. 4.2 shows comparison of J^{π} distributions of the ^{56}Mn compound nuclei formed by the ^{55}Mn(n,α)^{52}V and ^{55}Cr(p,α)^{52}V reactions at equivalent neutron energies of 5, 10, 15 and 20 MeV. Although calculations are carried out from threshold to 20 MeV in the steps of 1 MeV, only few selected results are plotted as the trends are similar. In Fig. 4.2, the figures on the left panel are the angular momentum distributions for the positive parity and the figures on the right panel are for the negative parity. The figure labels also indicate the average angular momentum $< J^{\pi} >= \frac{\sum_J \sigma^{CN}(E^*, J^{\pi}) J dJ}{\sum_J \sigma^{CN}(E^*, J^{\pi}) dJ}$ in both the neutron and proton induced reactions. It can be seen from Fig. 4.2 that the angular momentum distributions of the ^{56}Mn compound nuclei formed by the neutron and proton induced reactions are very similar and the average angular momentum difference is also less than 2ħ for all the positive and negative parities, throughout the energy range considered. This similar

angular momentum distribution is a result of the features in Fig. 4.1. In Fig. 4.2, at 5 MeV equivalent energy, the main contributions are from s, p, d, f, g and h-waves as shown in Fig. 4.1, in the case of neutron absorption. The J^{π} population of ^{56}Mn after neutron absorption on ^{55}Mn(5/2-) is therefore dominated by 0^-, 1^-, 2^-, 3^-, 4^-, 5^-, 6^-, 7^- and 0^+, 1^+, 2^+, 3^+, 4^+, 5^+, 6^+, 7^+, 8^+. Similarly, for the proton absorption in ^{55}Cr(3/2-), the main contributions are from s, p and d-waves as seen in Fig. 4.1. The J^{π} population of ^{56}Mn is dominated by 1^-, 2^-, 3^-, 4^- and 1^+, 2^+, 3^+. As the incident energy increases, higher angular momenta contribute resulting in the increase of the <J> value as shown in Fig. 4.2. The decrease of the difference in the <J> between the two incident channels as the energy increases can also be understood from Fig. 4.1.

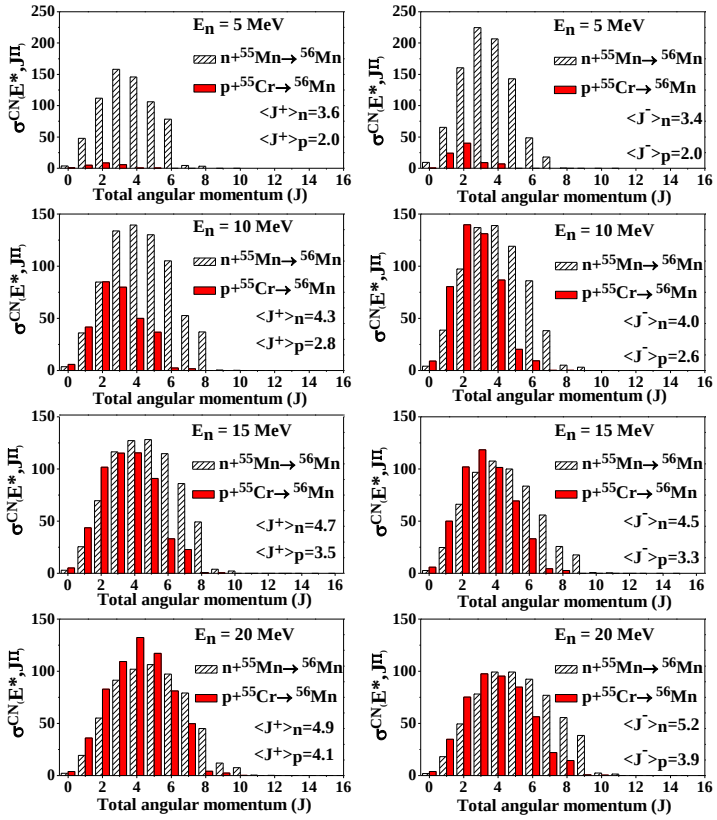

(a) **(b)**

Figure 4.2: Comparison of the J^{π} distributions of the ^{56}Mn compound nuclei formed by the neutron and proton induced reactions (a) for positive parity and (b) for negative parity.

Fig. 4.3 (a) & (b) shows the reaction cross sections for all the opening channels in both the neutron and proton induced reactions on the target nuclei ^{55}Mn and ^{55}Cr respectively in the energy range considered. The figure on the left panel is for the n+^{55}Mn channel and the right panel is for the p+^{55}Cr channel. It can be seen from the figure that the only opening channels are neutron, proton, gamma and alpha below ~7 MeV in both the channels. As the incident energy increases, the number of opening channels increased in both the case. It can also be seen that the alpha emission channel is maximum at ~15 MeV. However, since there are many other opening channels above ~15 MeV, the cross sections for ^{55}Mn(n,α)^{52}V and ^{55}Cr(p,α)^{52}V reactions is expected to decrease beyond this energy.

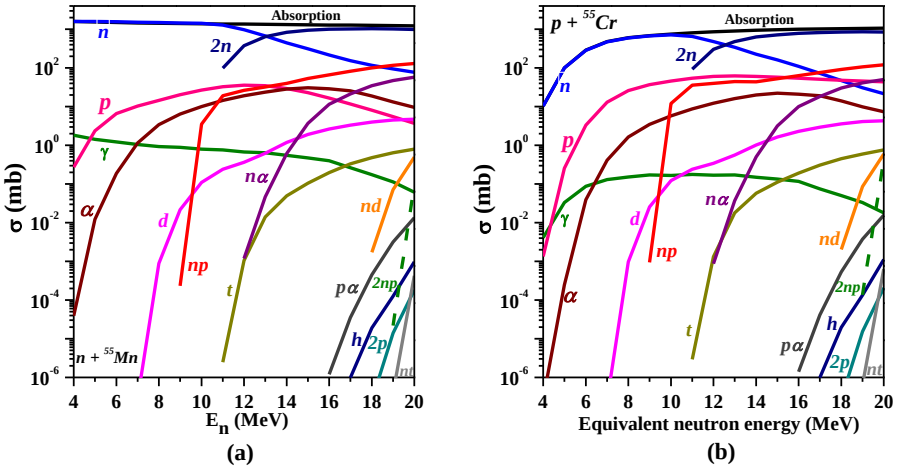

Figure 4.3: A plot of all the opening channels induced by neutron energy from 4 MeV to 20 MeV for the entrance channels: (a) n+^{55}Mn and (b) p+^{55}Cr (at equivalent neutron energy).

To optimize the models and parameters used in Talys-1.9, we performed calculations using six different level density models and eight different gamma ray strength functions available in Talys-1.9 which are compared with available experimental data (Paul *et al.*, 1953; Kumabe, 1958; Weigold, 1960; Nix *et al.*, 1961; Kaul, 1962; Gabbard and Kern, 1962; Peil, 1965; Khurana and Govil, 1965; Bormann *et al.*, 1965; Frevert, 1965; Minetti and Pasquarelli, 1967; Zupranska, 1980; Ngoc, 1980; Vanska and Rieppo, 1980; Florek, 1984; Bostan and Qaim, 1994; Fessler *et al.*, 2000; Zhang *et al.*, 2012; Filatenkov, 2016) taken from EXFOR database (Otuka *et al.*, 2014) and evaluated data taken from evaluated nuclear data libraries TENDL-2017(Koning *et al.*, 2017) and ENDF/B-VII.0 (Chadwick *et al.*, 2006) which is shown in Fig. 4.4. It can be seen that the reference cross section obtained using LDM4 best match the available experimental data and the evaluated nuclear data files of TENDL-2017 and ENDF/B-VII.0 whereas the gamma ray strength functions do not have significant effects for a given level density model. Therefore, the Talys-1.9 calculation with level density model 4 (LDM4) and the default gamma ray strength function (strength 1) are chosen as the 'Reference Model' or "benchmark" and this is compared with the extracted cross section. The same model and model parameters are adopted for all the reactions considered in this work.

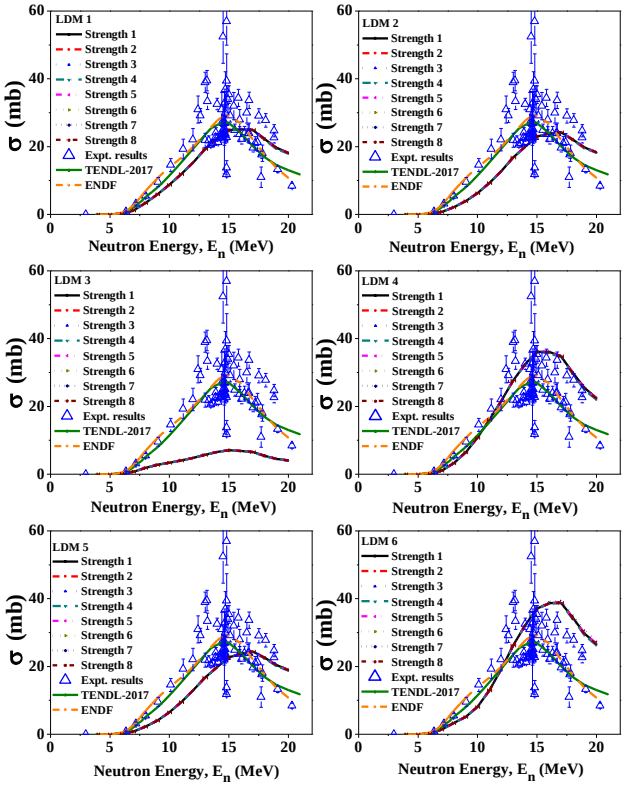

Figure 4.4: Comparison between the reference $^{55}Mn(n,\alpha)^{52}V$ reaction cross section calculated using all the available level density models and gamma ray strength functions in TALYS-1.9, the available experimental data taken from EXFOR database and the evaluation data of TENDL-2017 and ENDF/B-VII.0.

Fig. 4.5 shows comparison between the alpha decay branching ratios of the ^{56}Mn compound nuclei formed by the neutron and proton induced reactions using the reference model. It can be seen that the alpha decay branching ratios obtained from the ^{56}Mn compound nuclei formed by these two reactions match perfectly throughout the energy ranged considered. These results show that although ^{56}Mn compound nuclei were formed by the neutron and proton induced reactions with the averaged

angular momentum mismatch less than 2ħ throughout the energy range considered, this mismatch do not show significant influence on the alpha decay probabilities.

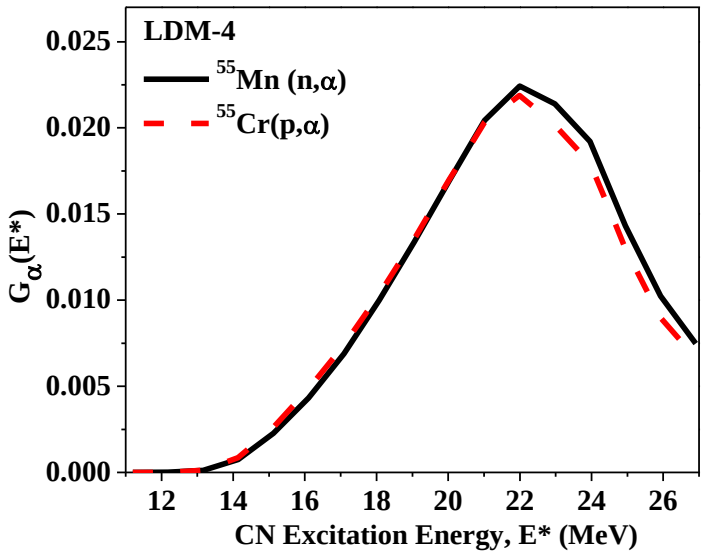

Fig. 4.5: Comparison between the alpha decay branching ratio of the ^{56}Mn compound nuclei from the ^{55}Mn(n,α)^{52}V and ^{55}Cr(p,α)^{52}V reactions.

Fig. 4.6 shows comparison between the reference (n,α) reaction cross section including both compound nucleus and preequilibrium contributions and the extracted (n,α) reaction cross sections from the proton induced alpha decay branching ratio using Eq. (2.53). As is already obvious from Fig. 4.5, we observed good agreement between the reference ^{55}Mn(n,α)^{52}V reaction cross sections with the extracted neutron induced reaction cross sections from the ^{55}Cr(p,α)^{52}V reaction which also agrees well with the experimental cross sections. This result shows that reliable and accurate ^{55}Mn(n,α)^{52}V reaction cross section can be measured or extracted with the ^{55}Cr(p,α)^{52}V reaction and vice versa. ^{55}Cr is unstable ($T_{1/2}$ = 3.497 mins), and can be produced in reactor environments using ^{54}Cr(n,γ), ^{53}Cr(n,γ)^{54}Cr(n,γ), ^{52}Cr(n,γ)^{53}Cr(n,γ)^{54}Cr(n,γ) etc. channels. Since Chromium is structural elements in

fission and fusion reactors, accurate knowledge of neutron or proton induced reaction cross sections for its stable as well as unstable isotopes is very important. It is also worth noting that due to the availability of sufficient experimental cross sections for $^{55}Mn(n,\alpha)^{52}V$ reaction, this information can be utilized to validate or use as evaluation tool for the $^{55}Cr(p,\alpha)^{52}V$ reaction cross section for the evaluated nuclear data libraries as shown in the present work.

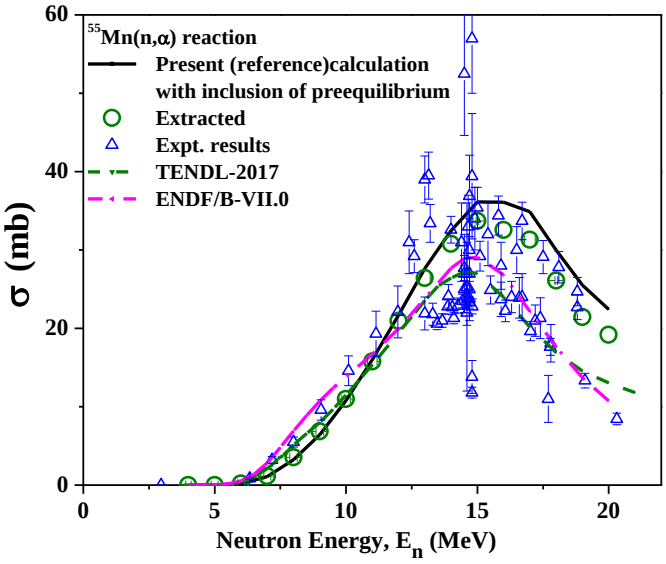

Figure 4.6: Comparison between the reference $^{55}Mn(n,\alpha)^{52}V$ reaction cross section including both compound nucleus and preequilibrium contributions calculated using LDM4, and the extracted neutron induced reaction cross sections from the proton induced reactions using Eq. (2.53) labelled as "Extracted", the available experimental data taken from EXFOR and the evaluation data of TENDL-2017 and ENDF/B-VII.0.

4.3. The $^{55}Fe(n,\alpha)^{52}Cr$ reaction

In this case, the reaction of interest is the $^{55}Fe(n,\alpha)^{52}Cr$ reaction. Similar to the previous case, since the target ^{55}Fe is unstable, an alternative $^{55}Mn(p,\alpha)^{52}Cr$ reaction will be used to extract the $^{55}Fe(n,\alpha)^{52}Cr$ reaction cross section. On conversion of the proton energy to its equivalent neutron energy, the proton energy scale has been shifted by ~1.032 MeV with respect to the neutron energy scale. The important physical information necessary for theoretical calculations between the reactions under considered are given in Table 4.4.

Table 4.4: General information of $^{55}Mn(p,\alpha)^{52}Cr$ and $^{55}Fe(n,\alpha)^{52}Cr$ reactions

Sl. No.	**Physical quantity**	**$^{55}Mn(p,\alpha)^{52}Cr$**	**$^{55}Fe(n,\alpha)^{52}Cr$**
1	Projectile spin (s)	0.5	0.5
2	Projectile parity	+1	+1
3	Projectile mass	1.00782503223 a.m.u.	1.008665 a.m.u.
4	Target spin (I)	2.5	1.5
5	Target parity	-1	-1
6	Target mass	54.93804391 a.m.u.	54.938291994 a.m.u.
7	Q-value	2.57042 MeV	3.58386 MeV
8	Separation Energy of projectile	10.18367 MeV	11.1971 MeV
9	Reaction Threshold	0	0

Similar to Fig. 4.1, Figure 4.7 shows the neutron and proton transmission coefficients on ^{55}Fe and ^{55}Mn targets respectively calculated using global optical potential by Koning and Delaroche for several partial waves ranging from l = 0 to 9. The solid curves represent the neutron transmission coefficients on the ^{55}Fe target, and the dash lines are for the proton transmission coefficients on the ^{55}Mn target. The list of possible states of the J^{π} population of the compound nucleus ^{56}Mn formed via n+^{55}Mn and p+^{55}Cr are given in Table 4.5 and 4.6 respectively.

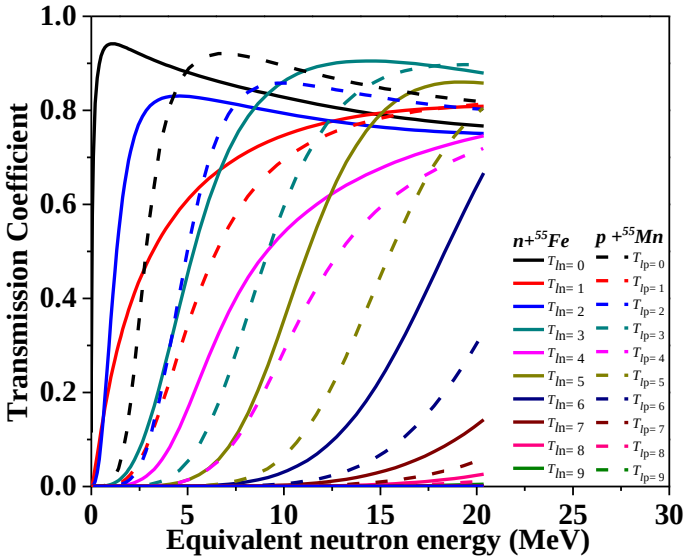

Figure 4.7: Transmission coefficients of neutron on ^{55}Fe and proton on ^{55}Mn.

Table 4.5: Possible J^{π} states of the compound nucleus ^{56}Fe formed via n + ^{55}Fe

l	**Designation**	**Spin and Parity of Projectile (neutron)** ***s***	**Spin of target (^{55}Fe)** ***I***	**Possible Spin and Parity of the Compound Nucleus (^{56}Fe)** J^{π}
0	s	0.5^{+}	1.5^{-}	$1^{-}, 2^{-}$
1	p			$0^{+}, 1^{+}, 2^{+}, 3^{+}$
2	d			$0^{-}, 1^{-}, 2^{-}, 3^{-}, 4^{-}$
3	f			$1^{+}, 2^{+}, 3^{+}, 4^{+}, 5^{+}$
4	g			$2^{-}, 3^{-}, 4^{-}, 5^{-}, 6^{-}$
5	h			$3^{+}, 4^{+}, 5^{+}, 6^{+}, 7^{+}$
6	i			$4^{-}, 5^{-}, 6^{-}, 7^{-}, 8^{-}$

Table 4.6: Possible J^{π} states of the compound nucleus ^{56}Fe formed via p + ^{55}Mn

l	**Designation**	**Spin and Parity of Projectile (proton)** ***s***	**Spin of target (^{55}Mn)** ***I***	**Possible Spin and Parity of the Compound Nucleus (^{56}Fe)** J^{π}
0	s	0.5^{+}	2.5^{-}	$2^{-}, 3^{-}$
1	p			$1^{+}, 2^{+}, 3^{+}, 4^{+}$
2	d			$0^{-}, 1^{-}, 2^{-}, 3^{-}, 4^{-}, 5^{-}$
3	f			$0^{+}, 1^{+}, 2^{+}, 3^{+}, 4^{+}, 5^{+}, 6^{+}$
4	g			$1^{-}, 2^{-}, 3^{-}, 4^{-}, 5^{-}, 6^{-}, 7^{-}$
5	h			$2^{+}, 3^{+}, 4^{+}, 5^{+}, 6^{+}, 7^{+}, 8^{+}$
6	i			$3^{-}, 4^{-}, 5^{-}, 6^{-}, 7^{-}, 8^{-}, 9^{-}$

Again, similar to Fig. 4.2, Fig. 4.9 shows the J^{π} distributions of the ^{56}Fe compound nuclei formed by the ^{55}Fe(n,α)^{52}Cr and ^{55}Mn(p,α)^{52}Cr reactions at equivalent incident neutron energies 5, 10, 15 and 20 MeV. Again, calculations are

carried out from 1-20 MeV in the steps of 1 MeV. It can be seen from Fig. 4.8 that the angular momentum distributions of the ^{56}Fe compound nuclei formed by the neutron and proton induced reactions are very similar and the average angular momentum difference is less than 0.5ħ for all the positive and negative parities, throughout the energy range considered. Again as in the case of ^{55}Mn(n,α)^{52}V and ^{55}Cr(p,α)^{52}V reactions, this similar angular momentum distribution is a result of the features of partial waves in Fig. 4.7. In Fig. 4.8, at 5 MeV incident energy, the J^{π} population of ^{56}Fe after neutron absorption on ^{55}Fe(3/2$^-$) is dominated by 0$^-$, 1$^-$, 2$^-$, 3$^-$, 4$^-$, 5$^-$, 6$^-$ and 0$^+$, 1$^+$, 2$^+$, 3$^+$, 4$^+$, 5$^+$, 6$^+$,7$^+$. These J^{π} states of the compound nucleus are populated predominantly after neutron absorption that can be reached by s, p, d, f, g and h-waves capture which can be seen from Fig. 4.7. Similarly, at the same equivalent energy of 5 MeV, the J^{π} population of ^{56}Fe after proton absorption on ^{55}Mn(5/2$^-$) is dominated by 0$^-$, 1$^-$, 2$^-$, 3$^-$, 4$^-$, 5$^-$, 6$^-$, 7$^-$ and 0$^+$, 1$^+$, 2$^+$, 3$^+$, 4$^+$, 5$^+$, 6$^+$,7$^+$ after s, p, d, f, g and h-waves capture shown in Fig. 4.8. The averaged J^{π} distribution of the ^{56}Fe compound nucleus formed is almost similar from the neutron and proton induced reactions even at low incident energies compared to the previous case where the difference in <J$^+$> at 5 MeV incident energy is 1.6ħ. Although the Projectile-Target spins and parity are very similar in both the cases, the much lower difference in <J$^+$> for the ^{55}Fe(n,α)^{52}Cr and ^{55}Mn(p,α)^{52}Cr reactions compared to ^{55}Mn(n,α)^{52}V and ^{55}Cr(p,α)^{52}V reactions may be attributed to the much higher neutron and proton separation energies, 11.197 MeV and 10.184 MeV in n + ^{55}Fe -> ^{56}Fe* and p + ^{55}Mn -> ^{56}Fe* systems respectively whereas the neutron and proton separation energies are 7.270 MeV and 9.091 MeV for n + ^{55}Mn -> ^{56}Mn* and p + ^{55}Cr -> ^{56}Mn* systems respectively. Therefore, even at low incident energies, the compound nuclei formed

are populated at high excitation energies resulting into similar J^{π} distributions of compound nucleus.

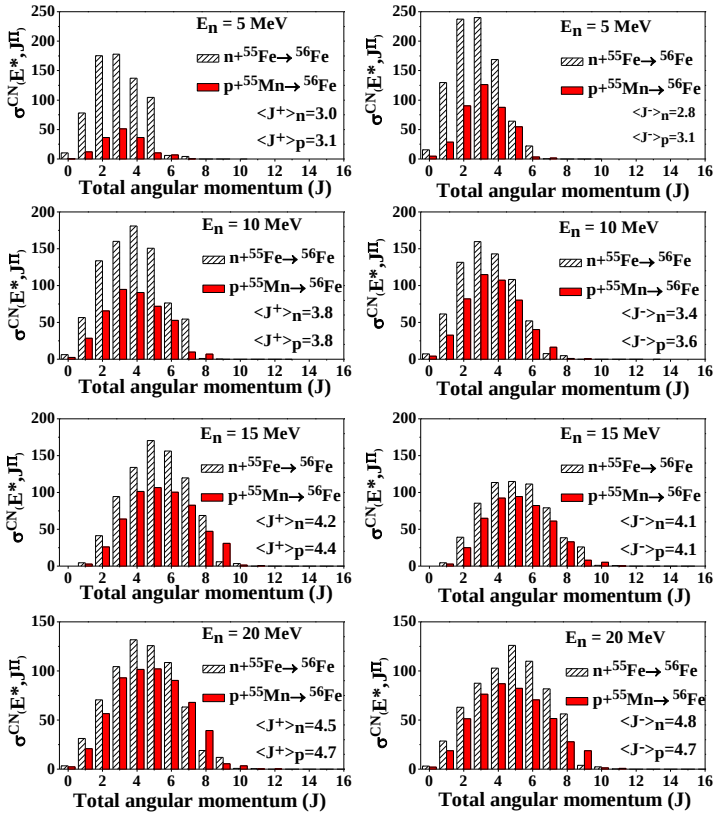

Fig. 4.8: Comparison of the $J\pi$ distributions of the ^{56}Fe compound nuclei formed by neutron and proton induced reactions (a) for the positive parity and (b) for the negative parity.

Similar to Fig. 4.3, Fig. 4.9 (a) & (b) shows the reaction cross sections for all the opening channels in both the neutron and proton induced reactions on the target nuclei ^{55}Fe and ^{55}Mn respectively in the energy range considered. The figure on the left panel is for the n+^{55}Fe channel and the right panel is for the p+^{55}Mn channel. Similar to the previous case, the only opening channels in this case are neutron,

proton, gamma and alpha below ~8 MeV in both the channels. As the incident energy increases, the number of opening channels increased in both the case. It can also be seen that the alpha emission channel is again maximum at ~15 MeV. However, since there are many opening channels above ~15 MeV, the cross sections for ^{55}Fe(n,α)^{52}Cr and ^{55}Mn(p,α)^{52}Cr reactions is expected to decrease beyond this energy.

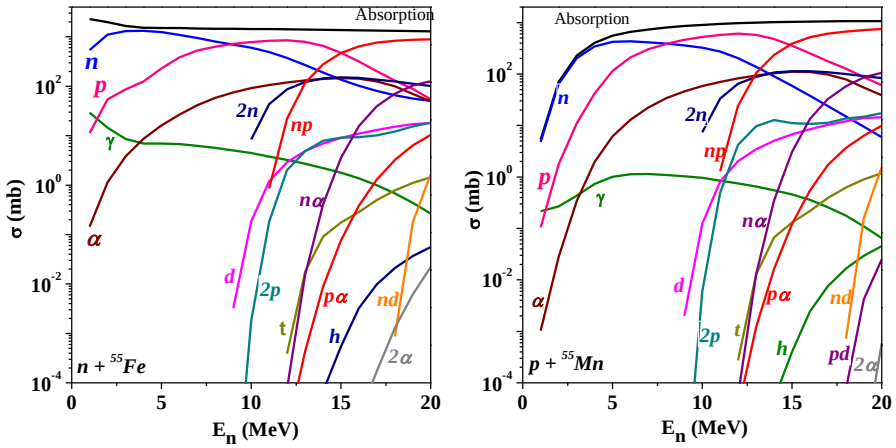

Figure 4.9: A plot of all the opening channels induced by neutron energy from thresholds up to 20 MeV for the entrance channels: (a) n+^{55}Fe and (b) p+^{55}Mn (at equivalent neutron energy).

Fig. 4.10 shows the alpha decay branching ratios of the ^{56}Fe compound nuclei formed by the ^{55}Fe(n,α)^{52}Cr and ^{55}Mn(p,α)^{52}Cr reactions. Again the branching ratios from this two different entrance channels match perfectly throughout the energy ranged considered. These results again show that the small J^{π} difference in the compound nuclei formed by the neutron and proton induced reactions do not exhibit significant influence in the alpha decay probabilities of the ^{56}Fe compound nucleus.

As is again obvious from Fig. 4.10, we observed a very good match between the reference cross sections and the extracted cross sections using Eq. (2.53) as shown in Fig. 4.11. The agreement between the decay branching ratios in the case of ^{55}Fe(n,α)^{52}Cr and ^{55}Mn(p,α)^{52}Cr reactions is better compared to ^{55}Mn(n,α)^{52}V and ^{55}Cr(p,α)^{52}V reactions which is a result of a much lower J^{π} mismatch in the former case.

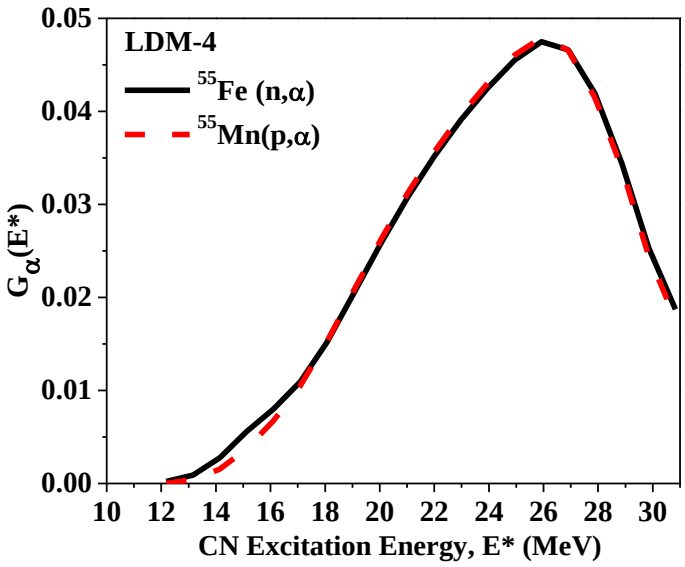

Fig. 4.10: Comparison between the alpha decay branching ratios of the ^{56}Fe compound nuclei formed by the ^{55}Fe(n,α)^{52}Cr and ^{55}Mn(p,α)^{52}Cr reactions.

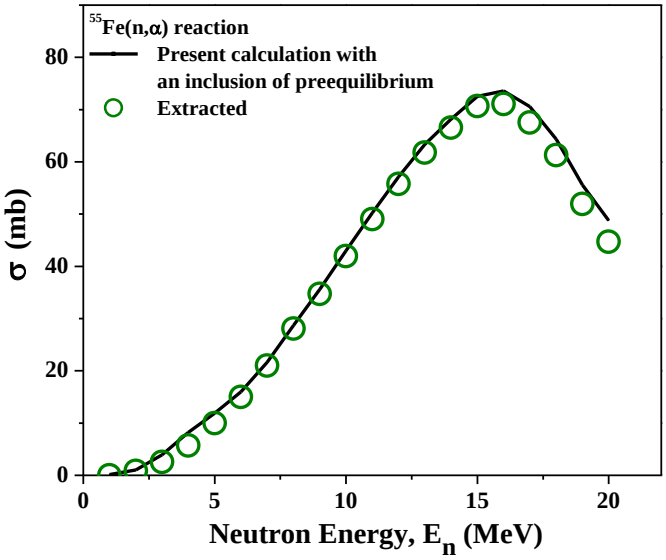

Fig. 4.11: Comparison between the reference $^{55}Fe(n,\alpha)^{52}Cr$ reaction cross section including both compound nucleus and preequilibrium contributions calculated using LDM4 and the extracted cross section obtained using Eq. (2.53) labelled as "Extracted".

4.4. Study on the dependence of the alpha branching ratios on the level structure of residual nuclei

In the present work, the influence of the level structure of the nuclei produced after alpha emission has been studied. The residual nucleus ^{52}Cr is stable. However the residual nucleus ^{52}V is unstable. Both the decay data and level structures are well known and are available in ENSDF. The plots of cumulative energy levels/MeV in the discrete region also show a good exponential growth without any abrupt break showing that the discrete energy levels are complete.

^{52}V has many low lying energy levels, the first excited state is 17.2 keV whereas ^{52}Cr has very low number of low lying energy levels, the first excited state is 1.434 MeV. Although the J^{π} mismatch is large within 2ħ in ^{55}Mn(n,α)^{52}V and ^{55}Cr(p,α)^{52}V reactions, however, due to large number of low lying states in the residual nucleus ^{52}V, the alpha decay probability do not depend much on the CN J^{π}. However, in the case of ^{55}Fe(n,α)^{52}Cr and ^{55}Mn(p,α)^{52}Cr reactions, although the number of low lying energy states are low, the J^{π} distribution of the CN ^{56}Fe is almost similar within 0-0.3 ħ difference even at low incident energies resulting in almost similar alpha decay branching ratio.

To study the dependence on the level structure of the residual nuclei at low energy, we performed calculations in which we force the TALYS code to adopt level structure of ^{52}Cr (which has very low number of low lying energy levels) for ^{52}V rather the the existing level structure of ^{52}V(which has large number of low lying energy levels) for ^{55}Mn(n,α)^{52}V and ^{55}Cr(p,α)^{52}V reactions which are shown in the Fig. 4.12 given below. We observe that the alpha decay branching ratio very much depend on the level structure of the residual nucleus. One can also observe that the discrepancy reduces as the excitation energy increases, and the decay branching ratio is almost independent on the low lying level structure at high excitation energies.

In Fig. 4.13, we show the comparison between alpha decay branching ratio for ^{55}Mn(n,α)^{52}V and ^{55}Cr(p,α)^{52}V reactions where ^{55}Cr(p,α)^{52}V is forced to use level structure of ^{52}Cr. We see large difference in the alpha decay branching ratio between the two. This indicates that the alpha decay branching ratio depend on the level structure of the low lying energy levels of the residual nucleus.

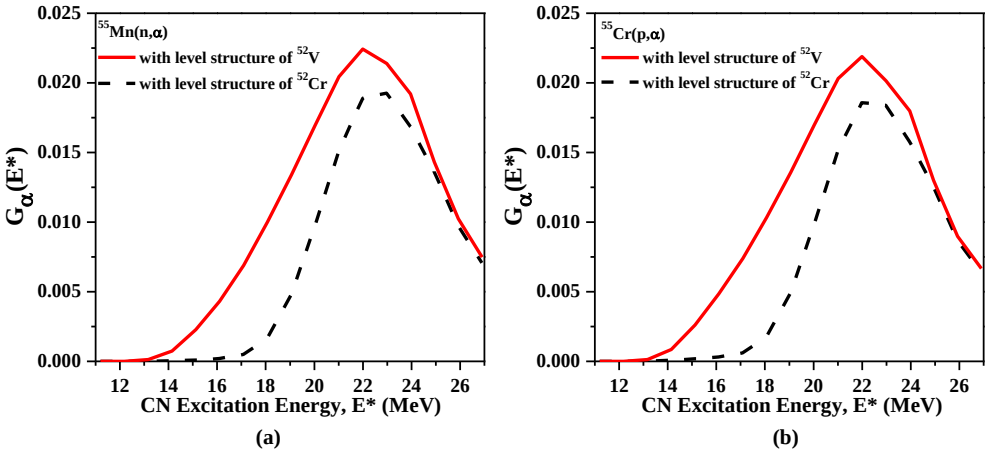

Fig. 4.12: Comparison of alpha decay branching ratio for ^{55}Mn(n,α)^{52}V and ^{55}Cr(p,α)^{52}V reactions with the level structure of ^{52}V and ^{52}Cr respectively.

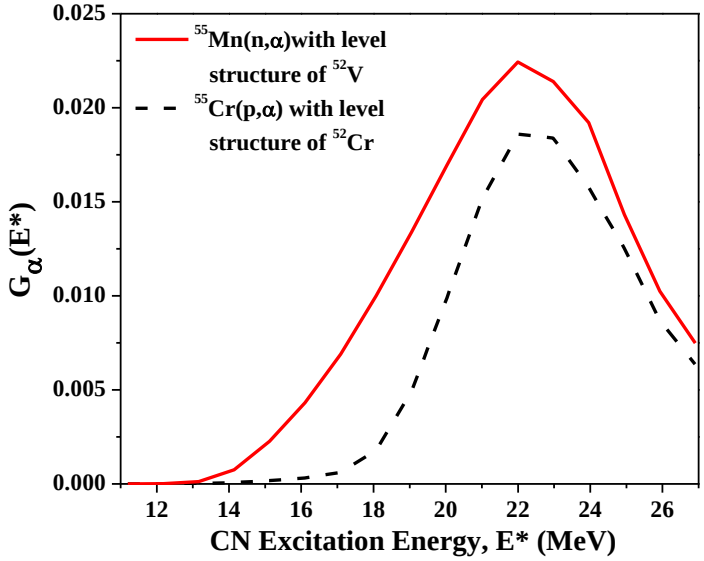

Fig. 4.13: Comparison of alpha decay branching ratio for ^{55}Mn(n,α)^{52}V and ^{55}Cr(p,α)^{52}V reactions where ^{55}Cr(p,α)^{52}V is forced to use level structure of ^{52}Cr.

4.5. Operating conditions of RF oscillator

Figure 3.1 shows the circuit diagram of RF oscillator using twin beam-power tetrode 829B. The oscillator is basically a push-pull Hartley oscillator employing grid-leak biasing method. It has an operating frequency of 102 MHz, which corresponds to the fundamental frequency as all the even harmonics are cancelled out in push-pull oscillator. The oscillation frequency of the oscillator is primarily determined by the resonance frequency of the RF coil forming LC tank circuit and is given by

$$f = 1/2\pi\sqrt{(LC)}, \qquad (4.1)$$

At 102 MHz, calculation using current-sheet coil geometrical formula gives L = 0.36 μH and C = 2.46 pF, where C is the stray capacitance of the coil. Therefore the self-resonance frequency of the tank coil according to Eq. (4.1) is 169 MHz. But this is far above the observed frequency of oscillation. To get oscillation at 102 MHz with L = 0.36 μH, the value of C has to be 6.76 p. The 4.3pF difference in capacitance is very close to the inter-electrode capacitance of the tube, which is 4.4 pF according to calculation from the tube data sheet. This observation suggests that contribution from the inter-electrode capacitance should not be neglected while designing an RF coil to obtain operating frequency of desired value.

The values of R_g and C_g in the grid leak network determine the control grid biased voltage and hence the operating point of the tube. The amount of biased voltage depends on the amplitude, frequency of the signal and grid leak time constant (Terman, 1955). In high power RF oscillator, the RC time constant has to be kept at low value relative to the cycle time of the signal (Pridham, 1972). In our case, the grid leak time constant is 6.8 ns which is about one-half cycle of the operating

frequency. When the value of grid leak resistor is changed from 6.8 kΩ to 22 kΩ, the frequency is observed to decrease by about 47 MHz. The decrease in frequency is due to occurrence of intermittent oscillation caused by large value of R_g. At high value of R_g and hence RC time, the biased voltage developed is too large that oscillation stops, and restarts after the capacitor has discharged through R_g till proper grid biasing voltage is reached again (Pridham, 1972). Intermittent oscillation has frequency lower than the operating frequency.

Frequency and power stability are other important characteristics to consider in the operation of the oscillator. In the present oscillator, the operating frequency is found to decrease by about 1% as a result of loading, as well as tank coil oxidation. Tank coil oxidation is the formation of copper oxide layer on the surface of the RF coil. It increases the effective dielectric constant between the coil windings constituting the capacitive part of the tank circuit. Since the tank circuit determines the frequency of oscillation, any variation in the conditions of the external circuit will be coupled back into the frequency determining portion of the oscillator. These variations result in the above observed frequency instability. Tank coil oxidation is also found to reduce the output power by about 10% when compared with freshly polished tank coil. This is due to the higher electrical resistance of copper oxide layer leading to lower Q value of the coil. Thus to avoid power reduction due to tank coil oxidation all power measurements were conducted after cleaning the copper tank coil external surface with sander paper. The efficiency of the oscillator including power supply unit is also measured and found to be 37%.

4.6. RF output power and measurements

The variation of output power with plate voltage of the 829B tube is investigated using two different techniques - a modified form of photometric method and RF peak voltage detection method. The modification made in the present photometric setup is the application of LDR as light sensor to improve the sensitivity and accuracy level of the relative power measurement. LDR is semiconductor device whose resistance decreases with the intensity of light incident on it. However, the dependence of LDR resistance on light intensity is not linear and varies as bL^{-a} (Regtien *et al.*, 2004), where L is the incident power per unit area, *a* and *b* are constants that depend on the material and shape of the resistor. LDR has spectral response almost similar to human eye and the low temperature coefficient. According to our measurement, the change in LDR current per degree Celsius is only about 0.02 mA. But incandescent light bulb wasted most part of the input energy in the form of heat and only less than 5% is converted into visible light. Therefore, RF power converted into heat will not be detected by LDR. However, the calibration method eliminates all the needs to consider the undetected part of the RF power dissipated in the filament except light.

Figure 4.14 shows the dependence of RF output power levels on plate voltages according to the two measurement methods for 829B and its equivalent, GI30. It can be seen that as the plate voltage increases the RF output power also increases accordingly and so saturation is seen within the range of measurement. However, the variation of output power with plate voltage is non-linear and can be described by quadratic function. The nature of the power curve is attributed to LDR and diode detector responses towards the intensity of light and RF signal

respectively. The RF power directly indicated by the present measurement technique is 79 ± 2% watts at 900V. This is higher than the value reported by Moak et al., 1951, which is 60 watts for the same circuit configuration and plate voltage. even though the power measurement technique or instrument used by Moak is not known.

However, when compared with peak voltage method, the photometric result is lower by about 11 watts on the average. The discrepancy between the two power readings cannot be due to the tube characteristics of 829B as similar result is observed with its equivalent GI30. As stated before, the power measured by photometric method corresponds to RF power that actually dissipated in the form of heat and light by the filament of the incandescent lamp. However, due to the imperfection (not pure inductive reactance) of the filament, there is always some amount of RF power that is neither converted into heat nor light even under the condition of perfect impedance matching. On the other hand, the dummy load used in the peak voltage method is purely resistive and there is no complication from inductance. Therefore, the discrepancy between power readings of the two methods is attributed to arise from the inductive reactance of the filament of light bulb load in photometric technique. To further confirm this, the inductive reactance of the filament is calculated directly from its physical dimension and the amount of RF power attenuated by it is estimated from the variation of 50 Hz AC power consumed by 100 watt light bulb in the presence of different series inductors.

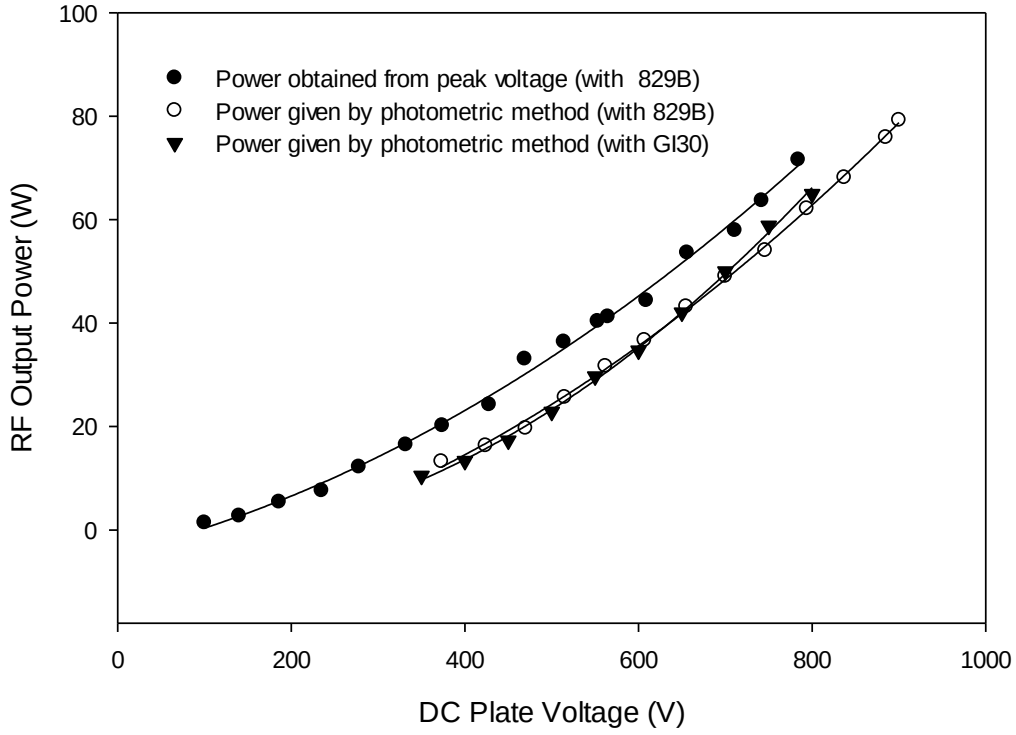

Fig. 4.14: Variation of RF output power with plate voltages (350-900 V) for 829B and GI30 according to photometric and peak voltage measurements.

Figure 4.15 shows the plot of ac power vs inductive reactance in a 50 Hz AC circuit for different inductances, with linear fittings to the data points. Each curve corresponds to a given value of applied AC voltage to the light bulb load. The different curves appear to be parallel suggesting that the inductor attenuation coefficient represented by the slope of the curve is independent of the applied voltages. Therefore, the relationship between AC power and inductive reactance can be described by the following linear equation

$$P = P_d - 0.13X_L, \qquad (4.2)$$

where P is the ac power in watt and X_L is the series inductive reactance in the circuit. The slope in Eq. (4.2) is the average of the four straight line fits to the experimental

data. P_d is the intercept on power axis which corresponds to ac power consumed by the load without series inductor. Assuming the inductor attenuation coefficient to be the same in RF region, the amount of power correction required to apply in photometric method will be $0.13X_L$, where X_L is the inductive reactance of the filament at 102 MHz.

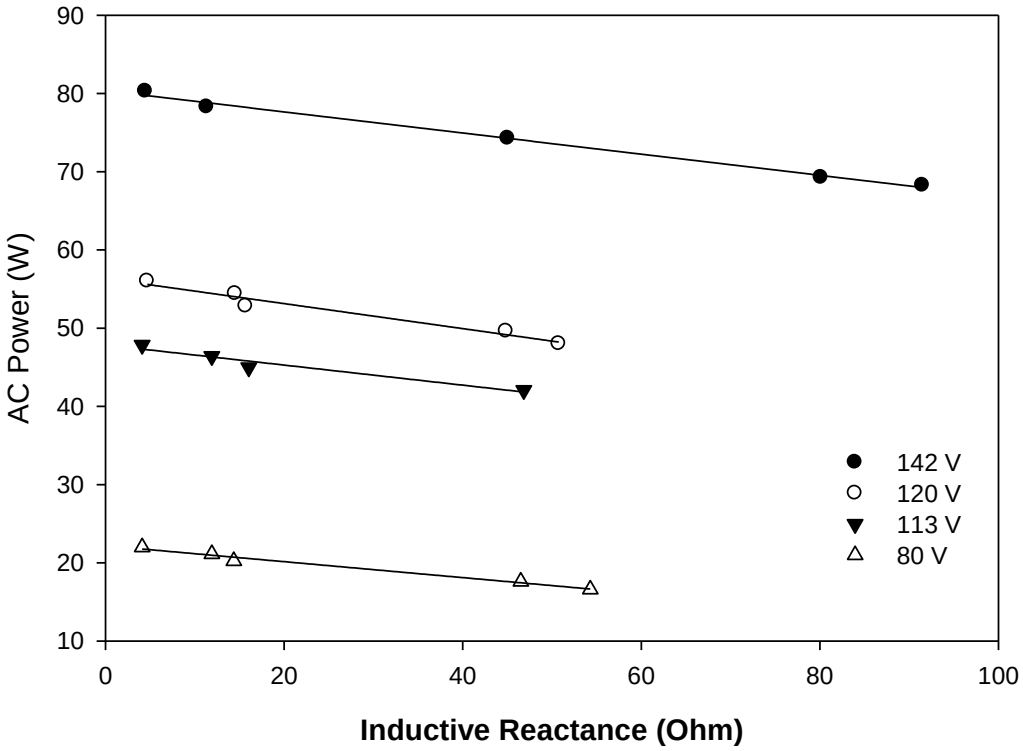

Figure 4.15: Variation of AC power dissipated by 100 watt incandescent lamp at different values of inductive reactance and applied voltages.

The inductance of the filament calculated according to straight solenoid approximations are 141 nH and 284 nH respectively for the bigger and smaller coil of the filament. As the two inductances are in series in the filament structure, the equivalent inductance of 425 nH for the series combination can also be the effective

inductance of the filament as a whole. Toroidal approximation is also applied but gives the same inductance as that of the inner coil. Thus, we have three different possible values of inductance for the filament, which can result in power attenuation of 12, 24 and 35 watts.

In Figure 4.16, comparison is made again between power calculated from RF peak value and photometric result after applying the above possible power corrections. It can be seen that among the different possible photometric power curves, the one having 12 watts power correction is closest to the power curve obtained from peak voltage measurement methods. Therefore, we can conclude that the power difference of about 11 watts observed between the two measurement methods in Figure 4.14 is due to the fact that the filament is not a perfect inductor. Thus the power level directly indicated by photometric method using 100 watt filament light bulb as RF signal detector in the measurement has to be further corrected for about 12 watts to bring its accuracy level to that of peak voltage measurement. Accordingly the total output power of the oscillator at 900 V plate voltages would be 90 watts instead of 79 watts. Power correction of 12 watts comes from the inductive reactance X_L of the bigger coil alone having inductance 141 nH, further suggesting that the effective inductance of the filament in incandescent lamp is largely determined by the inductance of the bigger coil. It is also interesting to see that the corrected total output power is in very good agreement with the reported maximum power rating of 90 watts for Class C push pull oscillator using 829B tube under natural cooling according to the tube data sheet.

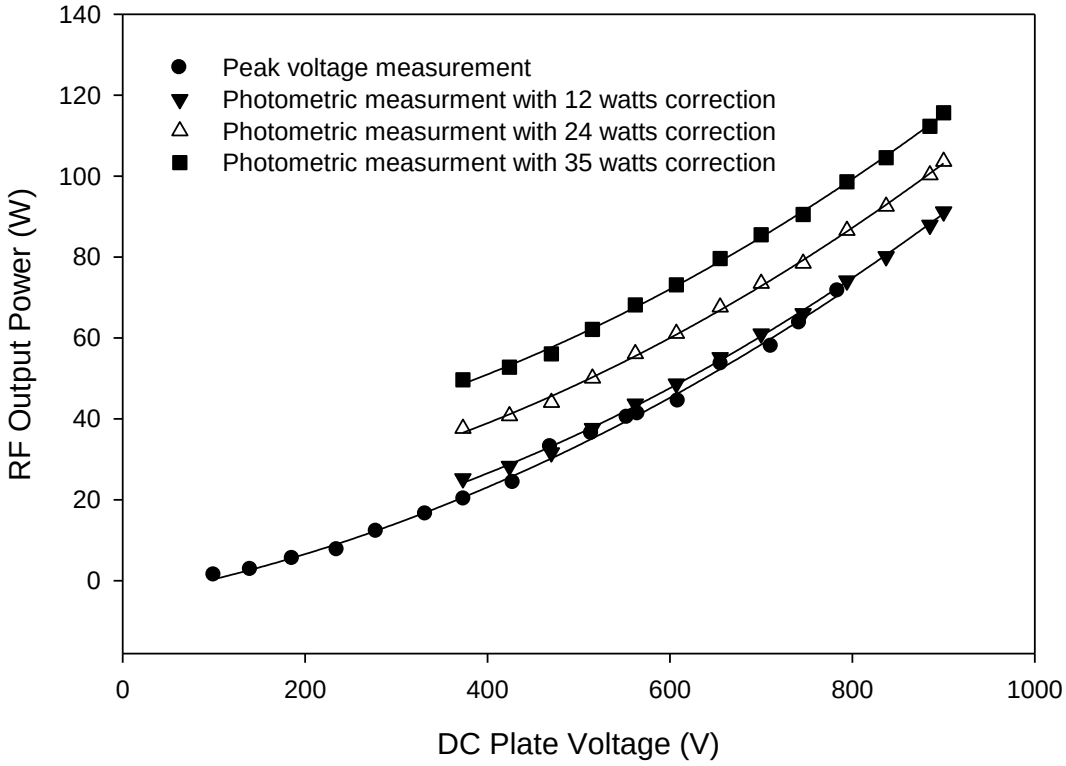

Figure 4.16: Comparison of RF power measured by peak voltage and photometric methods after correction for the effect of filament inductive reactance.

4.7. Performance of RF oscillator for different RF Coils

In the present work, four different RF coils are constructed using copper tube by winding it to 3 turns. The copper tube diameter is 6 mm and the length of pitch is 10 mm. A schematic diagram of the RF coil is shown in Figure 3.4. As the oscillation frequency is primarily determined by the coil diameter, four different coils with different diameters are constructed with the same pitch length and same number of turns to study the variation of operating frequency against the RF output power. The diameters of the four different RF coils along with their corresponding observed operating frequency is listed in table 4.7. Since the RF output power is decreased by

about 10% as a result of tank coil oxidation, the tank coils are freshly polished for each measurement. It has been found that the frequency of RF signal is quite stable and the fluctuation is found to be within ±0.1%.

Table 4.7: Description of RF coils and the observed operating frequency

Sl. No.	Diameter of the coil 'D' (mm)	Observed Frequency (MHz)
1	70	89.90
2	85	81.20
3	90	76.30
4	153	51.43

Figure 4.17 shows the variation of RF output power on the operating frequency of the RF oscillator at different DC plate voltages. Each set of measurement includes the RF power measurement at DC plate voltages 500V, 600V and 700V. At each plate voltages, the RF power is found to decrease with increase in the operating frequency of the RF oscillator accordingly as already discussed. The variation of RF power with operating frequency can be fitted using a common linear function with a slope of -0.38 for each different plate voltages. The fluctuation in the plate voltages may be observed at the time when one RF coil is removed for the next set of measurements. However, these fluctuations are negligible and found to be within ±1%.

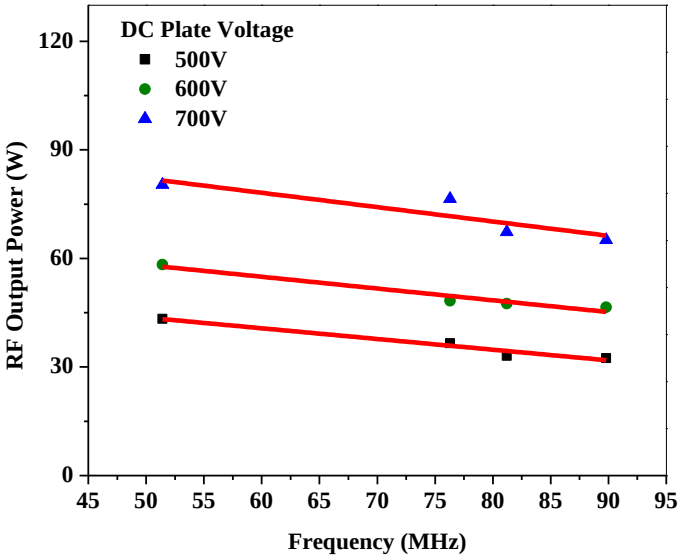

Figure 4.17: Variation of RF output power with operating frequency at different DC plate voltages.

Figure 4.18 shows the dependence of RF power levels on the DC plate voltage at different operating frequencies. It can be seen that as the plate voltage increases, the RF output power also increases accordingly. In the present study, power correction is not applied since the study is mainly focused on the variation of RF power with different operating frequencies. The RF output power reported in this work is directly the exact result of the modified form of the photometric method without applying any correction factor.

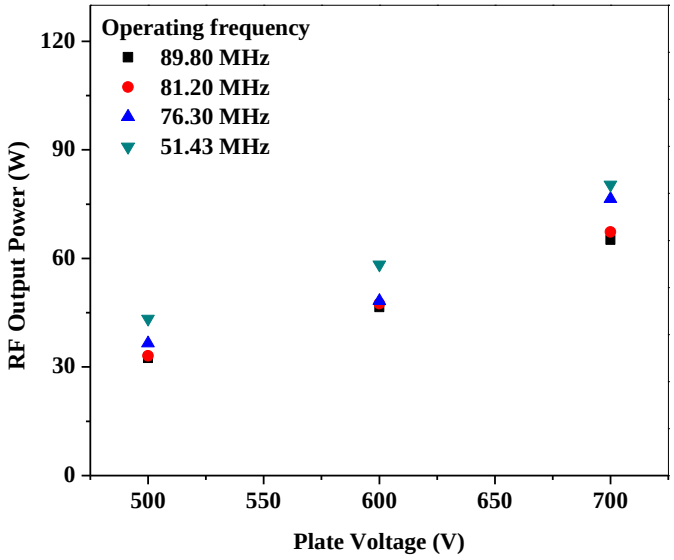

Figure 4.18: Variation of RF output power with plate voltage at different operating frequency.

CHAPTER 5

SUMMARY AND CONCLUSIONS

5. SUMMARY AND CONCLUSIONS

In the present work, we explore the possibility of using a simple (p,α) reactions to extract reliable (n,α) reactions using statistical nuclear reaction model simulation in the incident energy range from above 1 MeV up to 20 MeV. We investigate how the same compound nucleus at the same excitation energy produced by different entrance channels with different J^{π} distributions influence the alpha decay channel. In particular, we studied two combinations, (i) ^{55}Fe(n,α)^{52}Cr and ^{55}Mn(p,α)^{52}Cr, (ii) ^{55}Mn(n,α)^{52}V and ^{55}Cr(p,α)^{52}V reactions. It can be seen that both the ^{55}Fe(n,α)^{52}Cr and ^{55}Mn(p,α)^{52}Cr reactions form the same compound nucleus ^{56}Fe. The projectiles neutron and proton are spin ½ particles, and the target spins are 3/2 and 5/2 for ^{55}Fe and ^{55}Mn respectively and they both have negative parity. Similarly, ^{55}Mn(n,α)^{52}V and ^{55}Cr(p,α)^{52}V reactions also produced the same compound nucleus, which is ^{56}Mn. The target spins are 5/2 and 3/2 for ^{55}Mn and ^{55}Cr respectively and they both have negative parity. There are no measured cross sections for ^{55}Fe(n,α)^{52}Cr and ^{55}Mn(p,α)^{52}Cr reactions to validate our theoretical results. However, there are sufficient number of experimental cross sections for ^{55}Mn(n,α)^{52}V reactions in the EXFOR Database (Otuka *et al.*, 2014), to validate our extracted theoretical results for ^{55}Mn(n,α)^{52}V reaction using the ^{55}Cr(p,α)^{52}V reaction.

It is observed that the averaged angular momentum difference are within 2ħ between the compound nuclei ^{56}Mn formed by neutron induced reaction on ^{55}Mn and proton induced reaction on ^{55}Cr throughout the energy range considered. Similarly, a

very similar J^{π} distributions with the averaged angular momentum difference within 0–0.3ħ is observed between the compound nuclei ^{56}Fe formed by neutron induced reaction on ^{55}Fe and proton induced reaction on ^{55}Mn throughout the energy range considered. It is also found that a small difference in the J^{π} distributions of the compound nuclei do not influence significantly the alpha decay probabilities in the energy range and reactions considered. We therefore concluded that (p,α) reactions can be used to extract (n,α) reaction cross sections and vice versa for the target isotopes studied in the present work.

In the systems under study, Projectile-Target spin-parity systems are very similar, resulting in very similar J^{π} distributions of compound nucleus. Moreover, the projectile separation energies in these systems are high, 11.197 MeV and 10.184 MeV in n + ^{55}Fe → ^{56}Fe* and p + ^{55}Mn → ^{56}Fe* systems respectively whereas the neutron and proton separation energies are 7.270 MeV and 9.091 MeV for n + ^{55}Mn → ^{56}Mn* and p + ^{55}Cr → ^{56}Mn* systems respectively resulting in population of compound nucleus at high excitation energies even at low incident energies. Moreover, as already explained, ^{52}V has many low lying energy levels, the first excited state is 17.2 keV whereas ^{52}Cr has very low number of low lying energy levels, and the first excited state is 1.434 MeV. Although the J^{π} mismatch is large within 2ħ in ^{55}Mn(n,α)^{52}V and ^{55}Cr(p,α)^{52}V reactions, however, due to large number of low lying states in the residual nucleus ^{52}V, the alpha decay probability do not depend much on the compound nucleus J^{π}. However, in the case of ^{55}Fe(n,α)^{52}Cr and ^{55}Mn(p,α)^{52}Cr reactions, although the number of low lying energy states are low, the J^{π} distribution of the compound nucleus ^{56}Fe is almost similar within 0-0.3 ħ

difference even at low incident energies resulting in almost similar alpha decay branching ratio. All these contributed to the validity of W-E approximation in the systems we studied.

A comparison of the gamma branching ratio has also been made, between the neutron and proton induced reactions on the target isotopes under studied, as shown below in Fig. 5.1. As also observed by Boutoux et al. (2012) and Scielzo et al. (2010), it is also observed in the present study that even a small compound nucleus J^{π} mismatch results in large difference in the gamma branching ratios between the neutron induced and proton induced reactions on the targets ^{55}Mn and ^{55}Cr, and on the targets ^{55}Fe and ^{55}Mn respectively. As mentioned before, the averaged J^{π} difference is very small in the case of ^{56}Fe* CN, however, large difference is still observed. However, it can be seen that the gamma decay branching difference is much lower in the case of ^{56}Fe* CN compared to ^{56}Mn* CN. In the case of ^{55}Fe(n,α)^{52}Cr and ^{55}Mn(p,α)^{52}Cr reactions, the J^{π} mismatch at 5 MeV and 20 MeV is almost similar as shown in Fig. 4.9, however, the discrepancy in the branching ratio is large in the low incident energy region and it reduces as the incident energy increases, this is also a clear indication of the dependence on the low lying energy states at low excitation energy.

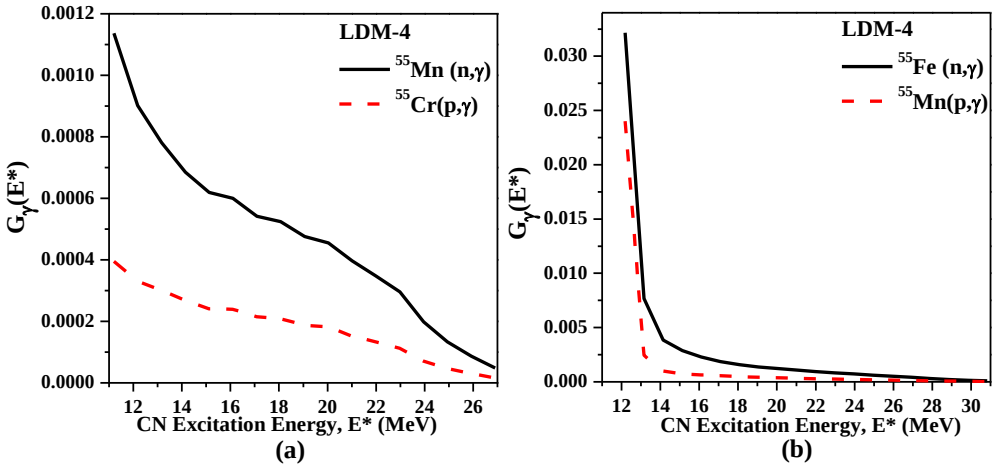

Fig. 5.1: Comparison of gamma decay branching ratio (a) ^{55}Mn(n,γ)^{56}Mn and ^{55}Cr(p,γ)^{56}Mn reactions, (b) ^{55}Fe(n,γ)^{56}Fe and ^{55}Mn(p,γ)^{56}Fe reactions

At this juncture, with limited systems and results presented in the present work, it is not possible to generalize the conclusion we made above, and it is not possible to give a range of target masses and J^{π}mismatch unless we perform such studies. This will be part of our future scope. However, at this point, due to the motivations that we mentioned in our Introduction, from the point of view of reactor applications in which ^{55}Cr and ^{55}Fe are produced which are both unstable, we restrict our studies and manuscript only for these four reactions. And the results are practically applicable since ^{55}Mn is stable and there are many experimental results. What we can mention is based on the results we obtained, and within 2 ħ of J^{π} mismatch, for the systems we studied, we observe similar alpha decay branching ratio. However, we also observe that the alpha decay branching ratio is also sensitive to the level structure of the low lying energy states of the residual nucleus; this therefore suggested that each reaction should be considered on a case by case basis.

In the present work, a self-excited push pull RF oscillator is constructed using 829B vacuum tube. The oscillator has operating frequency of 102 MHz which is quite stable with respect to loading and tank coil oxidation. However, copper oxide layer formation on RF coil surface could result in a decrease of RF output power as much as 10%. The variation of RF output power with plate voltage is studied using two power measurement techniques- photometric and RF peak voltage methods. As the plate voltage increases, the output power increases in a non- linear fashion which can be best described by quadratic function. However, inductive component present in the load/detector of photometric method is found to cause decrease in power readings. The effective inductance of the filament appears to be largely determined by the bigger coil structure and the resulting power attenuation is estimated to be about 12 watts when compared with power value obtained from peak voltage measurement. Therefore, the total output power of the oscillator comes out to be ~ 91 watts at 900 V plate voltage which is about 31 watts higher than the power value reported by Moak *et al.*, 1951.

The operating frequency of the Oscillator is primarily determined by the resonance frequency of RF coil forming LC tank circuit. Four different RF coils are constructed for studying the RF power variation. The operating frequency for each different RF coils are found to be quite stable.

The RF power variations on the operating frequency of the RF oscillator are studied. The RF power is measured using a modified form of the photometric method. It has been found that the RF output power has a linear dependence on the operating frequency of the RF Oscillator as shown in Fig. 4.17. The RF power decreases with increases in the operating frequency of coil forming LC tank circuit.

With increase in the diameter of the RF coil, the operating frequency of the RF coil is found to decrease and hence increases the RF output power. Furthermore, the variation of RF power with the DC plate voltage at different operating frequency confirms that the RF power decreases with increase in the operating frequency as shown in Fig. 4.18. As the RF power vs. Frequency plot of Fig. 4.17 can be fitted with a common linear function, it can also be concluded that the RF power dependence on the operating frequency of the RF oscillator is not affected by the change in the plate voltage.

REFERENCES

REFERENCES

Ajay Kumar, (2014), "Study of angular momentum variation due to entrance channel effect in heavy ion fusion reactions", *J. Phys. Conf. Ser.* **515**, 012011(1-9).

Allmond J.M., Bernstein L.A., Beausang C.W., Phair L., Bleuel D.L., Burke J.T., Escher J.E., Evans K.E., Goldblum B.L., Hatarik R., Jeppesen H.B., Lesher S.R., McMahan M.A., Rasmussen J.O., Scielzo N.D., Wiedeking M., (2009), "Relative ^{235}U(n,γ) and (n,f) cross sections from ^{235}U(d,pγ) and (d,pf)", *Phys. Rev. C* **79**, 054610 (1-9).

Anastasi A., Mandaglio G., Curciarello F., Nasirov A.K., Fazio G., Giardina G., (2018), "Entrance channel effects on the deexcitation ways of the same compound nucleus at a fixed excitation energy", *J. Phys.: Conf. Ser.*, **1014**, 012007 (1-9).

Axel P., (1962), "Electric dipole ground-state transition width strength function and 7-MeV photon interactions", Phys. Rev., 126, 671-683.

Bass R., (1973), "Threshold and angular momentum limit in the complete fusion of heavy ions", *Phys. Lett. B* **47**, 139 – 142.

Basunia M.S., Clark R.M., Goldblum B.L., Bernstein L.A., Phair L., Burke J.T., Beausang C.W., Bleuel D.L., Darakchieva B., Dietrich F.S., Evtimova M., Fallon P., Gibelin J., Hatarik R., Jewett C.C., Lesher S.R., McMahan M.A., Rodriguez-Vieitez E., Wiedeking M., (2009), "The (^{3}He,tf) as a surrogate reaction to determine (n,f) cross sections in the 10–20 MeV energy range", *Nucl. Instrum. Methods Phys. Res., Sect. B* 267, 1899-1903.

Bernstein L.A., Burke J.T., Ahle L., Church J.A., Escher J., Dietrich F.S., Lyles B.F., Norman E.B., Phair L.W., Bleuel D.L., Clark R.M., Fallon P., Lee I.Y.,

Macchiavelli A.O., McMahan M.A., Moretto L.G., Rodriguez-Vieitez E., Ai H.C., Beausang C.W., Crider B., (2006), "Deducing the ^{237}U destruction cross-sections using the Surrogate Ratio Method", Technical Report, Lawrence Livermore National Laboratory, Livermore, CA.

Bhawna Pandey, Desai V.V., Suryanarayana S.V., Nayak B.K., Saxena A., Mirgule E.T., Santra S., Mahata K., Makawana R., Abhangi M., Basu T.K., Rao C.V.S., Jakhar S., Vala S., Sarkar B., Agrawal H.M., Kaur G., Prajapati P.M., Asim Pal, Sarkar D., Kundu A., (2016), "Measurement of ^{55}Fe(n, p) cross sections by the surrogate-reaction method for fusion technology applications", *Phys. Rev. C* **93**, 021602(R) (1-6).

Bissem H.H., Georgi R., Scobel W., (1980), "Entrance and exit channel phenomena in d- and ^{3}He-induced preequilibrium decay", *Phys. Rev. C* **22**, 1468-1483.

Boger J., John M. Alexander, Roy A. Lacey, and Narayanan A., (1994), "Tests for equilibration of ^{149}Tb* composite nuclei produced in the reactions 337 MeV ^{40}Ar+^{nat}Ag and 640 MeV ^{86}Kr+^{63}Cu", *Phys. Rev. C* **49 (3)**, 1587-1596.

Bormann M., Fretwurst E., Schehka P., Wrege G., Buttner H., Lindner A., Meldner H., (1965), "Some excitation functions of neutron induced reactions in the energy range 12.6–19.6 MeV", *Nucl. Phys.* **63**, 438-448.

Bostan M., Qaim S.M., (1994), "Excitation functions of threshold reactions on ^{45}Sc and ^{55}Mn induced by 6 to 13 MeV neutrons", *Phys. Rev. C* **49**, 266-271.

Boutoux G., Jurado B., Méot V., Roig O., Mathieu L., Aïche M., Barreau G., Capellan N., Companis I., Czajkowski S., Schmidt K.-H., Burke J.T., Bail A., Daugas J.M., Faul T., Morel P., Pillet N., Théroine C., Derkx X., Sérot O.,

Matéa I., Tassan-Got L., (2012), “Study of the surrogate-reaction method applied to neutron-induced capture cross sections”, *Phys. Lett. B* **712**, 319-325.

Boyer S., Dassié D., Wilson J.N., Aïche M., Barreau G., Czajkowski S., Grosjean C., Guiral A., Haas B., Osmanov B., Aerts G., Berthoumieux E., Gunsing F., Theisen Ch., Thiollière N., Perrot L., (2006), “Determination of the ^{233}Pa(n,γ) capture cross section up to neutron energies of 1 MeV using the transfer reaction $^{232Th}(^{3}He,p)^{234}Pa*$”, *Nucl. Phys. A* **775**, 175- 187.

Brink D.M., (1957), “Individual particle and collective aspects of the nuclear photoeffect”, Nucl. Phys., 4, 215-220.

Britt H.C., Wilhelmy J.B., (1979), “Simulated (n,f) Cross Sections for Exotic Actinide Nuclei”, *Nucl. Sci. Eng.* 72, 222-229.

Brown I.G., (2004), “The Physics and Technology of Ion Sources”, Second Edition., Berlin: Wiley-VCH.

Burke J.T., Bernstein L.A., Escher J., Ahle L., Church J.A., Dietrich F.S., Moody K. J., Norman E.B., Phair L., Fallon P., Clark R.M., Deleplanque M.A., Descovich M., Cromaz M., Lee I.Y., Macchiavelli A.O., McMahan M.A., Moretto L.G., Rodriguez-Vieitez E., Stephens F.S., Ai H., Plettner C., Beausang C., Crider B., (2006), “Deducing the ^{237}U(n, f) cross section using the surrogate ratio method”, *Phys. Rev. C* **73**, 054604 (1-8).

Capote R., Herman M., Obloz̆insky P., Young P.G., Goriely S., Belgya T., Ignatyuk A.V., Koning A.J., Hilaire S., Plujko V., Avrigeanu M., Bersillon O., Chadwick M.B., Fukahori T., Kailas S., Kopecky J., Maslov V.M., Reffo G., Sin M., Soukhovitskii E., Talou P., Han Y.L., Ge Z.G., (2009), “RIPL –

Reference Input Parameter Library for Calculation of Nuclear Reactions and Nuclear Data Evaluations", *Nucl. Data Sheets* **110 (12)**, 3107-3214.

Chadwick M.B., Obložinský P., Herman M., Greene N.M., McKnight R.D., Smith D.L., Young P.G., MacFarlane R.E., Hale G.M., Frankle S.C., Kahler A.C., Kawano T., Little R.C., Madland D.G., Moller P., Mosteller R.D., Page P.R., Talou P., Trellue H., White M.C., Wilson W.B., Arcilla R., Dunford C.L., Mughabghab S.F., Pritychenko B., Rochman D., Sonzogni A.A., Lubitz C.R., Trumbull T.H., Weinman J.P., Brown D.A., Cullen D.E., Heinrichs D.P., McNabb D.P., Derrien H., Dunn M.E., Larson N.M., Leal L.C., Carlson A.D., Block R.C., Briggs J.B., Cheng E.T., Huria H.C., Zerkle M.L., Kozier K.S., Courcelle A., Pronyaev V., van der Marck S.C., (2006), "ENDF/B-VII.0: Next Generation Evaluated Nuclear Data Library for Nuclear Science and Technology", *Nucl. Data Sheets* **107 (12)**, 2931–3060.

Cinausero M., Prete G., Fabris, D., Nebbia G., Viesti G., Dai G.X., Hagel K., Li J., Lou Y., Natowitz J.B., Utley D., Wada R., Gelli N., Lucarelli F., Colonna M., (1996), "Entrance channel mass asymmetry and the decay of hot nuclei", *Phys. Lett. B* **383**, 372-376.

Conhaim R.L., (1963), "R.F. power output measurements", *Electronics world* **70**, 53–56.

Cramer J.D., Britt H.C., (1970), "Neutron Fission Cross Sections for ^{231}Th, ^{233}Th, ^{235}U, ^{237}U, ^{239}U, ^{241}Pu, ^{243}Pu from 0.5 to 2.25 MeV using (t,pf) Reactions", *Nucl. Sci. Eng.* **41**, 177-187.

Desai V.V., Nayak B.K., Saxena A., Mirgule E.T., Suryanarayana S.V.,(2013), "Determination of the ^{239}Np (n,f) and ^{240}Np(n,f) cross sections using the surrogate reaction method", *Phys. Rev. C* **88**,014613 (1-6).

Desai V.V., Nayak B.K., Saxena A., Biswas D.C., Mirgule E.T., Bency John, Santra S., Gupta Y.K., Danu L.S., Prajapati G.K., Joshi B.N., Mukhopadhyay S., Kailas S., Pujari P.K., Kumar A., Patel D., Mukherjee S., Prajapati P.M., (2013), "Determination of ^{241}Pu(n,f) cross sections by the surrogate-ratio method", *Phys. Rev. C* **87**, 034604 (1-4).

Escher J.E., Burke J.T., Dietrich F.S., Scielzo N.D., Thompson I.J., Younes W., (2012), "Compound-nuclear reaction cross sections from surrogate measurements", *Rev. Mod. Phys.* **84**, 353-394.

Eubank H.P., Peck Jr. R.A., Truell R., (1954), "Operating Characteristics of a High Yield Rf Ion Source", *Rev. Sc. Instr.* **25**, 989–995.

Fantz U., Franzen P., Kraus W., Berger M., Christ-Koch S., Fröschle M., Gutser R., Heinemann B., Martens C., McNeely P., Riedl R., Speth E., Wünderlich D., (2007), "Negative ion RF sources for ITER NBI: status of the development and recent achievements", *Plasma Phys. Control. Fusion* **49**, B563–B580.

Fessler A., Plompen A.J.M., Smith D.L., Meadows J.W., Ikeda Y., (2000), "Neutron Activation Cross-Section Measurements from 16 to 20 MeV for Isotopes of F, Na, Mg, Al, Si, P, Cl, Ti, V, Mn, Fe, Nb, Sn, and Ba", *Nucl. Sci. Eng.* **134**, 171-200.

Filatenkov A.A., (2016), "Neutron activation cross sections measured at KRI in neutron energy region 13.4 - 14.9 MeV", Report No. INDC(CCP)-0460 Rev., International Atomic Energy Agency.

Florek M., Oravec J., Szarka I., Holy K., Jahn U., Helfer H., (1984), "Study of (n,α) Reactions on the ^{55}Mn and ^{60}Ga isotopes with 3 MeV neutrons", *Czech. J. Phys.* **34**, 30.

Forssen C., Dietrich F.S., Escher J., Hoffman R.D., Kelley K., (2007), "Determining neutron capture cross sections via the surrogate reaction technique", *Phys. Rev. C* **75**, 055807 (1-14).

Frevert E., (1965), "Bestimmung des wirkungsquerschnittes fur den (n, he3)-prozess an ^{55}Mn, ^{59}Co, ^{75}As und ^{103}Rh fur 14.8 MeV-neutronen", *Acta Phys. Austriaca* **20**, 304.

Gabbard F., Kern B.D., (1962), "Cross Sections for Charged Particle Reactions Induced in Medium Weight Nuclei by Neutrons in the Energy Range 12-18 MeV", *Phys. Rev.* **128**, 1276-1281.

Ganguly A.K., Bakhru H., (1963), "Operational Characteristics of a Radio Frequency Ion-Source", Nucl. Instrum. Methods Phys. Res **21**, 56 – 64.

Ghoshal S. N., (1950), "An Experimental Verification of the Theory of Compound Nucleus", *Phys. Rev.* ***80*** **(6)**, 939-942.

Gilbert A. and Cameron A.G.W., (1965), "A composite nuclear-level density formula with shell corrections", *Can. J. Phys.*, **43**, 1446-1496.

Goldblum B.L., Prussin S.G., Agvaanluvsan U., Bernstein L.A., Bleuel D.L., Younes W., Guttormsen M., (2008), "Determination of (n,γ) cross sections in the rare-earth region using the surrogate ratio method", *Phys. Rev. C* **78**, 064606 (1-6).

Goldblum B.L., Prussin S.G., Bernstein L.A., Younes W., Guttormsen M., Nyhus H.T., (2010), "Surrogate ratio methodology for the indirect determination of neutron capture cross sections", *Phys. Rev. C* **81**, 054606 (1-7).

Goldblum B.L., Stroberg S.R., Allmond J.M., Angell C., Bernstein L.A., Bleue D.L., Burke J.T., Gibelin J., Phair L., Scielzo N.D., Swanberg E., Wiedeking M., Norman E.B., (2009), "Indirect determination of the ^{230}Th(n,f) and ^{231}Th(n,f) cross sections for thorium-based nuclear energy systems", *Phys. Rev. C* **80**, 044610 (1-6).

Goodwin L.K., (1953), "Design and Performance of a Radio Frequency Ion Source.", *Rev. Sc. Instr.* **24**, 635–638.

Goriely S., (1998), "Radiative neutron captures by neutron-rich nuclei and the r-process nucleosynthesis", *Phys. Lett. B* **436**, 10-18.

Goriely S., Hilaire S., Koning A.J.,(2008), "Improved microscopic nuclear level densities within the HFB plus combinatorial method", *Phys. Rev. C* **78**, 064307.

Govil I.M., Singh R., Kumar A., Datta S.K., Kataria S.K., (2000), "Search for entrance channel effects in the decay of compound nucleus", *Nucl. Phys. A* **674**, 377-393.

Gunsing F., Aberle O., Andrzejewski J., Becares L.A.V., Bacak M., Balibrea-Correa J., Barbagallo M., Barros S., Becvar F., Beinrucker C., Belloni F., Berthoumieux E., Billowes J., Bosnar D., Brugger M., Caamano M., Calvino F., Calviani M., Cano-Ott D., Cardella R., Castelluccio D.M., Cerutti F., Chen Y., Chiaveri E., Colonna N., Cortes-Giraldo M.A., Cortes G., Cosentino L., Damone L., Deo K., Diakaki M., Domingo-Pardo C., Dupont R.D.E., Duran I., Fernandez-Dominguez B., Ferrari A., Ferreira P., Finocchiaro P., Frost R.W., Furman V., Ganesan S., Gawlik A., Gheorghe I., Glodariu T., Goncalves I.F., Gonzalez E., Goverdovski A., Griesmayer E., Guerrero C.,

Gobel K., Harada H., Heftrich T., Heinitz S., Hernandez-Prieto A., Heyse J., Jenkins G., Jericha E., Kappeler F., Kadi Y., Katabuchi T., Kavrigin P., Ketlerov V., Khryachkov V., Kimura A., Kivel N., Kokkoris M., Krticka M., Leal-Cidoncha E., Lederer C., Leeb H., Lerendegui J., Licata M., Meo S.L., Losito R., Macina D., Marganiec J., Martinez T., Massimi C., Mastinu P., Mastromarco M., Matteucci F., Maugeri E.A., Mendoza E., Mengoni A., Milazzo P.M., Mingrone F., Mirea M., Montesano S., Musumarra A., Nolte R., Oprea A., Pinto F.R.P., Paradela C., Patronis N., Pavlik A., Perkowski J., Porras J.I., Praena J., Quesada J.M., Rauscher T., Reifarth R., Riego-Perez A., Robles M., Rubbia C., Ryan J.A., Sabate-Gilarte M., Saxena A., Schillebeeckx P., Schmidt S., Schumann D., Sedyshev P., Smith A.G., Stamatopoulos A., Suryanarayana S., Tagliente G., Tain J.L., Tarifeno-Saldivia A., Tassan-Got L., Tsinganis A., Valenta S., Vannini G., Variale V., Vaz P., Ventura A., Vlachoudis V., Vlastou R., Wallner A., Warren S., Weigand M., Weiss C., Wolf C., Woods P.J., Wright T., Zugec P., (2015), "Nuclear data measurements at the upgraded neutron time-of-flight facility n TOF at CERN", 14th International Conference on Nuclear Reaction Mechanisms, *https://cds.cern.ch/record/2115398,* 323-330.

Hall R.N., (1948), "High Frequency Proton Source", *Rev. Sci. Instrum*.**19**, 905–910.

Hatarik R., Bernstein L.A., Cizewski J.A., Bleuel D.L., Burke J.T., Escher J.E., Gibelin J., Goldblum B.L., Hatarik A.M., Lesher S.R., O'Malley P.D., Phair L., Rodriguez-Vieitez E., Swan T., Wiedeking M., (2010), "Benchmarking a surrogate reaction for neutron capture", *Phys. Rev. C* **81**, 011602 (1-5).

Hauser W., Feshbach H., (1952), “The Inelastic Scattering of Neutrons”, *Phys. Rev.* **87**, 366-373.

Hilaire S., Girod M., S. Goriely, A.J. Koning, (2012), “Temperature-dependent combinatorial level densities with the D1M Gogny force”, *Phys. Rev. C* **86**, 064317.

Houk R.S., Fassel V.A., Flesch G.D., Svec H.J., Gray A.L., Taylor C.E., (1980), “Inductively Coupled Argon Plasma as an Ion Source for Mass Spectrometric Determination of Trace Elements”, *Anal. Chem.* **52**, 2283-2289.

Huo Junde, (2008), “Nuclear Data Sheets for A = 55”, *Nucl. Data Sheets* **109**, 787-942.

Kaufman H.R., Cuomo J.J., Harper J.M.E., (1982), “Technology and applications of broadbeam ion sources used in sputtering. Part I. Ion source technology”, *J. Vac. Sci. Technol.* **21**, 725–736.

Kaul O.N., (1962), “α-Particles emitted from 14 MeV neutron interactions with light and medium-weight nuclei”, *Nucl. Phys.* **39**, 325-334.

Kessedjian G., Jurado B., Aiche M., Barreau G., Bidaud A., Czajkowski S., Dassié D., Haas B., Mathieu L., Audouin L., Capellan N., Tassan-Got L., Wilson J.N., Berthoumieux E., Gunsing F., Theisen Ch., Serot O., Bauge E., Ahmad I., Greene J.P., Janssens R.V.F., (2010), “Neutron-induced fission cross sections of short-lived actinides with the surrogatereaction method”, *Phys. Lett. B* **692**, 297-301.

Khurana C.S., Govil I.M., (1965), “The (n, α), (n, p) and (n, t) cross-sections at 14.8 MeV”, *Nucl. Phys.* **69**, 153-157.

Koning A.J., Hilaire S., Goriely S., (released in December, 2017), computer code TALYS, version 1.9, *http://www.talys.eu*.

Koning A.J., Delaroche J.P., (2003), "Local and global nucleon optical models from 1 keV to 200 MeV", *Nucl. Phys. A* **713**, 231-310.

Kopecky J. and Uhl M., (1990), "Test of gamma-ray strength functions in nuclear reaction model calculations", Phys. Rev. C, 41, 1941-1955.

Kumabe I., (1958), "Alpha Particles from the Interaction of 14.8-MeV Neutrons with Medium Weight Nuclei", *J. Phys. Soc. Jpn.* **13**, 325-334.

Lalremruata B., Dhole S.D., Ganesan S., Bhoraskar V.N., (2009), "Double differential cross-sections of (n,α) reactions in aluminium and nickel at 14.77 MeV neutrons", *Nucl. Phys. A* **821**, 23-35.

Lesher S.R., Burke J.T., Bernstein L.A., Ai H., Beausang C.W., Bleuel D.L., Clark R.M., Dietrich F.S., Escher J.E., Fallon P., Gibelin J., Goldblum B.L., Lee I.Y., Macchiavelli A.O., McMahan M.A., Moody K.J., Norman E.B., Phair L., Rodriguez-Vieitez E., Scielzo N.D., Wiedeking M., (2009), "Surrogate ratio method in the actinide region using the (α,α'f) reaction", *Phys. Rev. C* **79**, 044609 (1-7).

Lyles B. F., Bernstein L. A., Burke J. T., Dietrich F. S., Escher J., Thompson I., (2007), "Absolute and relative surrogate measurements of the ^{236}U(n,f) cross section as a probe of angular momentum effects", *Phys. Rev. C* **76**, 014606 (1-8).

Lyles B. F., Bernstein L. A., Burke J. T., Dietrich F. S., Escher J., Thompson I., (2007), "Publisher's Note: Absolute and relative surrogate measurements of

the ^{236}U(n,f) cross section as a probe of angular momentum effects", *Phys. Rev. C* **76**, 019905-1 (2007).

Minetti B., Pasquarelli A., (1967), "Cross sections of the (n, p) and (n, α) reactions induced in Manganese by 14.7 MeV neutrons", *Z. Phys.* **199**, 275-279.

Moak C.D., Reese Jr. H., Good, W.M., (1951), "Design and Operation of a Radio-Frequency Ion Source for Particle Accelerators", *Nucleonics* **9 (3)**, 18.

Nayak B.K., Saxena A., Biswas D.C., Mirgule E.T., John B.V., Santra S., Vind R.P., Choudhury R.K., Ganesan S., (2008), "Determination of the ^{233}Pa(n,f) reaction cross section from 11.5 to 16.5 MeV neutron energy by the hybrid surrogate ratio approach", *Phys. Rev. C* **78**, 061602 (1-5).

Ngoc P.N., Gueth S., Deak F., Kiss A., (1980), Ph.D Thesis (Ngoc), "Investigations of (n,p), (n,α) and (n,2n) reactions around 14 MeV", Hungarian Institute for Experimental Physics.

Nix J., Chittenden D., Gardner D.G., (1961), Oak Ridge Operations Office, Contract report **367**, 6.

Otuka N., Dupont E., Semkova V., Pritychenko B., Blokhin A.I., Aikawa M., Babykina S., Bossant M., Chen G., Dunaeva S., Forrest R.A., Fukahori T., Furutachi N., Ganesan S., Ge Z., Gritzay O.O., Herman M., Hlavač S., Katō K., Lalremruata B., Lee Y.O., Makinaga A., Matsumoto K., Mikhaylyukova M., Pikulina G., Pronyaev V.G., Saxena A., Schwerer O., Simakov S.P., Soppera N., Suzuki R., Takács S., Tao X., Taova S., Tárkányi F., Varlamov V.V., Wang J., Yang S.C., Zerkin V., Zhuang Y., (2014), "Towards a More Complete and Accurate Experimental Nuclear Reaction Data Library

(EXFOR): International Collaboration Between Nuclear Reaction Data Centres (NRDC)", *Nucl. Data Sheets* **120**, 272-276.

Paul E.B., Clarke R.L., (1953), "Cross-section measurements of reactions induced by neutrons of 14.5 MeV energy", *Can. J. Phys.* **31(2)**, 267-277.

Peil A., (1965), "Über die wirkungsquerschnitte einiger (n,α)- und (n,2n)- reaktionen für 14 MeV neutronen", *Nucl. Phys.* **66**, 419-428.

Petit M., Aiche M., Barreau G., Boyer S., Carjan N., Czajkowski S., Dassié D., Grosjean C., Guiral A., Haas B., Karamanis D., Misicu S., Rizea C., Saintamon F., Andriamonje S., Bouchez E., Gunsing F., Hurstel A., Lecoz Y., Lucas R., Theisen Ch., Billebaud A., Perrot L., Bauge E., (2004), "Determination of the ^{233}Pa(n,f) reaction cross section from 0.5 to 10 MeV neutron energy using the transfer reaction ^{232}Th(^{3}He,p)^{234}Pa*, *Nucl. Phys. A* **735**, 345-371.

Plettner C., Ai H., Beausang C.W., Bernstein L.A., Ahle L., Amro H., Babilon M., Burke J.T., Caggiano J.A., Casten R.F., Church J.A., Cooper J.R., Crider B., Gurdal G., Heinz A., McCutchan E.A., Moody K., Punyon J.A., Qian J., Ressler J.J., Schiller A., Williams E., Younes W., (2005), "Estimation of (n,f) cross sections by measuring reaction probability ratios", *Phys. Rev. C* **71**, 051602(R) (1-5).

Ressler J.J., Caggiano J.A., Francy C.J., Peplowski P.N., Allmond J.M., Beausang C.W., Bernstein L.A., Bleuel D.L., Burke J.T., Fallon P., Hecht A.A., Jordan D.V., Lesher S.R., McMahan M.A., Palmer T.S., Phair L., Scielzo N.D., Swearingen P.G., Warren G.A., Wiedeking M., (2010), "Fission fragment isomers populated via ^{6}Li + ^{232}Th", *Phys. Rev. C* **81**, 014301 (1-9).

Ressler J.J., Burke J.T., Escher J.E., Angell C.T., Basunia M.S., Beausang C.W., Bernstein L.A., Bleuel D.L., Casperson R.J., Goldblum B.L., Gostic J., Hatarik R., Henderson R., Hughes R.O., Munson J., Phair L.W., Ross T.J., Scielzo N.D., Swanberg E., Thompson I.J., Wiedeking M., (2011), "Surrogate measurement of the ^{238}Pu(n,f) cross section", *Phys. Rev. C* **83**, 054610 (1-7).

Rodriguez P., Krishnan R., Sundaram C.V., (1984), "Radiation effects in nuclear reactor materials—correlation with structure", *Bull. Mater. Sci.* **6 (2)**, 339–367.

Ruckelshausen A., Fischer R.D., Kuhn W., Metag V., Muhlhans R., Novotny R., (1986), "Unexpected Entrance-Channel Effects in the Decay of the Compound Nucleus ^{156}Er", *Phys. Rev. Lett.* **56**, 2356-2359.

S.R. Lesher, L.Phair, L.A.Bernstein, D.L.Bleuel, J.T.Burke, J.A.Church, P.Fallon, J.Gibelin, N.D. Scielzo, , M.Wiedeking, (2010), "STARS/LiBerACE: Segmented silicon and high-purity germanium detector arrays for low-energy nuclear reaction and structure studies", *Nucl. Instrum. Methods Phys. Res., Sect. A* **621**, 286-291.

Schardt D., Elsässer T., Schulz-Ertner D., (2010), "Heavy-ion tumor therapy: Physical and radiobiological benefits", *Rev. Mod. Phys.* **82**, 383–417.

Scielzo N.D., Escher J.E., Allmond J.M., Basunia M.S., Beausang C.W., Bernstein L.A., Bleuel D.L., Burke J.T., Clark R.M., Dietrich F.S., Fallon P., Gibelin J., Goldblum B.L., Lesher S.R., McMahan M.A., Norman E.B., Phair L., Rodriquez-Vieitez E., Sheets S. A., Thompson I. J., Wiedeking M., (2010), "Measurement of γ-emission branching ratios for ^{154,156,158}Gd compound

nuclei: Tests of surrogate nuclear reaction approximations for (n,γ) cross sections", *Phys. Rev. C* **81**, 034608 (1-12).

Steven J. Zinkle and Jeremy T. Busby, (2009), "Structural materials for fission & fusion energy", *Materials Today* **12 (11)**, 12–19.

Thoennessen M. *et al.*, (1991), "Nuclear Structure and Heavy-ion Reaction Dynamics 1990", Eds. R.R. Betts and J.J. Kolata, IOP Publish., *Inst. Phys. Conf. Ser. No.* **109**, 135.

Thoneman P.C., (1946), "High-frequency Discharge as an Ion Source", Nature **158**, 61.

Thonemann P.C., Moffat J., Roaf O., Saunders J.H., (1948), "The Performance of a New Radio-Frequency Ion Source", *Proc. Phys. Soc., London* **61**, 483–485.

TM 11-685/TO 31R-1-9, (1961), "Fundamentals of single-side band communication", Technical Manual, Departments of the Army and the Air Force, Washington DC, 119.

Tripathi S.K.P., Pribyl P., Gekelman W., (2011), "Development of a radio-frequency ion beam source for fast-ion studies on the large plasma device", *Rev. Sci. Instrum.* **82**, 93501.

Vanska R., Rieppo R., (1980), "On the simultaneous use of a Ge(Li) semiconductor and a NaI(Tl) scintillation detector in neutron activation cross-section measurements", *Nucl. Instrum. Methods* **171**, 281-287.

Voznyi V., Miroshnichenko V., Mordyk S., Shulha D., Storizhko V., Tokman V., (2013), "Development of the RF Ion Sources for Focused Ion Beam Accelerators", *J. Nano- Electron. Phys.* **5 (4)**, 04060 (1 – 4).

Wallner A., Buczak K., Lederer C., Vonach H., Faestermann T., Korschinek G., Poutivtsev M., Rugel G., Klix A., Seidel K., Plompen A., Semkova V., (2011), "Production of Long-lived Radionuclides ^{10}Be, ^{14}C, ^{53}Mn, ^{55}Fe, ^{59}Ni and ^{202g}Pb in a Fusion Environment", *J. Korean Phy. Soc.* **59**, 1378-1381.

Weigold E., (1960), "Cross Sections for the Interaction of 14·5 MeV Neutrons with Manganese and Cobalt", *Aust. J. Phys.* **13(2)**, 186-188.

Yanbin Zhang, Liangyong Zhao, Xiangzhong Kong, Rong Liu, Li Jiang, (2012), "Cross-sections for (n,2n), and (n,α) reactions on ^{55}Mn isotope around neutron energy of 14 MeV", *Radiat. Phys. Chem.* **81**, 1563-1567.

Younes W., Britt H.C., (2003), "Neutron-induced fission cross sections simulated from (t,pf) results", *Phys. Rev. C* **67**, 024610 (1-13).

Younes W., Britt H.C., (2003), "Simulated neutron-induced fission cross sections for various Pu, U, and Th isotopes", *Phys. Rev. C* **68**, 034610-(1-9).

Zhu X.-M., Chen W.-C., Zhang S., Guo Z.-G., Hu D.-W., Pu Y.-K., (2007), "Electron density and ion energy dependence on driving frequency in capacitively coupled argon plasmas", *J. Phys. D: Appl. Phys.* **40**, 7019–7023.

Zupranska E., Rusek K., Turkiewicz J., Zupranski P., (1980), "Excitation functions for (n, α) reactions in the neutron energy range from 13 to 18 MeV", *Acta Phys. Pol.* **11**, 853-861.

Research Publications

(A) Referred Journals

1. **Hlondo L. R.**, Lalremruata B., Punte L.R.M., Rebecca L., Lalnunthari J., Thanga H. H., (2016), "A revisit to self-excited push pull vacuum tube radio frequency oscillator for ion sources and power measurements", *Review of Scientific Instruments*, **87**, 045101: 1-6.
2. **Hlondo L.R.**, Lalremruata B., Thanga H.H., (2016), "Study of operational characteristics of self-excited push-pull vacuum tube oscillator for R.F. Ion sources", *Science and Technology Journal*, **4**, 60 – 64.
3. Pachuau Rebecca, Lalremruata B., Otuka N., **Hlondo L.R.**, Punte L.R.M., Thanga H.H., (2017), "Thick and thin target ^{7}Li(p,n)^{7}Be neutron spectra below the three-body break up reaction threshold", *Nuclear Science and Engineering*, **187**, 70 – 80.
4. Pachuau R., Lalremruata B., Otuka N., Suryanarayana S.V., Punte L.R.M., **Hlondo L.R.**, Desai V.V., Satheesh B., Kailas S., Ganesan S, Nayak B.K., Saxena A., (2018), "Energy dependence of the neutron capture cross section on ^{70}Zn near the inelastic scattering threshold", *Phys. Rev. C*, **97**, 064617.
5. Punte L.R.M., Lalremruata B., Otuka N., Suryanarayana S.V., Iwamoto Y., Pachuau R., Satheesh B., Thanga H.H., Danu L.S., Desai V.V., **Hlondo L.R.**, Kailas S., Ganesan S., Nayak B.K., Saxena A., (2017), "Measurements of neutron capture cross sections on ^{70}Zn at 0.96 and 1.69 MeV", *Phys. Rev. C*, **95**, 024619.

6. Lalremruata B., Punte L.R.M., Otuka N., Pachuau R., Iwamoto Y., Suryanarayana S.V., Nayak B.K., Satheesh B., Thanga H.H., Danu L.S., Desai V.V., **Hlondo L.R.**, Ganesan S., Saxena A., (March, 2017), "Measurements of neutron capture cross sections on 70Zn at 0.96 and 1.69 MeV", INDC(IND)-**0049**, International Atomic Energy Agency.
7. **Hlondo L.R.**, Lalremruata B., (2020), "Entrance channel effects on the alpha decay probabilities of neutron and proton induced reactions for target mass A= 55", *Nucl. Phys. A*, **1000**, 121844.

(B) Conference Proceedings

1. Pachuau R., Lalremruata B., Otuka N., **Hlondo L.R.**, Punte L.R.M., Thanga H.H., (2017), "A tool for calculation of 7Li(p, n)7Be neutron source spectra below the three body break-up reaction threshold", *Proceedings of the DAE-BRNS Symp. on Nucl. Phys*, **61**, 430-431.
2. Pachuau R., Lalremruata B., Otuka N., **Hlondo L.R.**, Punte L.R.M., and Thanga H.H., (2016), "A tool for calculation of 7Li(p, n)7Be neutron source spectra below the three body break-up reaction threshold", EPJ Web of Conferences **146**, 12016-12019.

Conferences/Workshops/Schools Attended

1. Two days workshop on Physics teaching in Higher Secondary Scho1ols of Mizoram, Department of Physics, Mizoram University, Aizawl, Mizoram, *8 – 9th May, 2014.*
2. Theme meeting cum workshop on Nuclear reaction code – EMPIRE, Department of Physics, University of Calicut, Kerala, India, *10 – 13th November, 2014*.
3. Sixth DAE-BRNS Workshop cum Theme meeting on EXFOR compilation, Bangalore University, Bangalore, *20 - 24th January, 2015*.
4. Condensed Matter Days – 2016, Department of Physics, Mizoram University, Aizawl, Mizoram, *29 – 31st August, 2016*.
5. National conference on Nuclear and accelerator physics (NCNAP-2016), Center for Applied Physics, Central University of Jharkhand, Ranchi, 4 – 6th October, 2016.
6. NDPCI-BRNS School on Nuclear Reactions and Applications, BARC, *Mumbai, 2 - 12th November, 2016.*
7. SERC School on nuclear physics: Nuclear Physics from new perspectives, Department of Physics, Bharathiar university, Coimbatore, Tamilnadu, *7 – 27th February, 2017.*
8. Joint ICTP-IAEA Workshop on the evaluation of nuclear reaction data for applications, International Centre for Theoretical Physics, Trieste, Italy, *2 – 13th October, 2017*.
9. Two days National Workshop on Error Propagation in Nuclear Reaction Data Measurement, Mizoram University, Aizawl, *13 – 14th March, 2017*.

10. National workshop on 'Ethics in research and preventing plagiarism (ERPP 2019), Department of Physics, Mizoram University, Aizawl, 3rd October, 2019.

11. Online Webinar on 'Research Publications and Citations Perspective of a Highly Cited Researcher', Department of Physics, Mizoram University, Aizawl, 16th June, 2020.

PARTICULARS OF THE CANDIDATE

NAME OF CANDIDATE : **H. Lalremruata**

DEGREE : **Ph.D**

DEPARTMENT : **Physics**

TITLE OF THESIS : ***Entrance channel effects on the alpha decay probabilities of neutron and proton induced reactions for target mass A=55 and characterization of RF oscillator for low energy charged particle accelerator***

DATE OF ADMISSION : **11th March, 2014**

APPROVAL OF RESEARCH PROPOSAL :

1. **BOS** : **15th October, 2014.**
2. **SCHOOL BOARD** : **20th October, 2014.**

REGISTRATION NO. & DATE : **MZU/Ph.D./690 of 20.10.2014**

EXTENSION : **NIL**

(Prof. R.C. TIWARI)
Head

BIODATA

Name	**:**	H. Lalremruata
Father's Name	**:**	H. Dothuama
Address	**:**	Middle School Road, High School Veng, Zemabawk, Mizoram; India-7960
Subject of Specialization	**:**	Electronics
Date of Birth	**:**	1st December 1989

Educational Qualifications:

▪ **HSLC**	2004	Distinction
▪ **HSSLC**	2006	Third Division
▪ **B.Sc (Physics)**	2009	Second Division
▪ **M.Sc (Physics)**	2013	First Division
▪ **Pre-Ph.D**	2014	Grade 'O'

Research Experience:

- Completed M.Sc Project work on Construction of RF Oscillator under the supervision of Dr. Hranghmingthanga, Department of Physics, Mizoram University.
- Joined the Nuclear Laboratory under the supervision of Dr. B. Lalremruata in August, 2013 and got admitted in the Department of Physics, Mizoram University as a Ph.D. Scholar in January 2014.
- Started research work in Characterization of RF Oscillator for ion sources under the supervision of Dr. B. Lalremruata and Joint Supervision of Dr. Hranghmingthanga, Department of Physics, Mizoram University, Aizawl, Mizoram till date.
- Development of a modified form of photometric method for measuring RF power.
- Development of the neutron energy spectrum code Energy of Proton Energy of Neutron (EPEN).
- Had experience in a nuclear reaction simulation software Talys.

- Studied entrance channel effect on the decay of a compound nucleus for targets of mass A=55 and developed a technique for extracting $^{55}Cr(p,\alpha)^{52}V$ and $^{55}Fe(n,\alpha)^{52}Cr$ reaction cross sections using $^{55}Mn(n,\alpha)^{52}V$ and $^{55}Mn(p,\alpha)^{52}Cr$ reactions respectively.

Reprint of research papers

AIP | Review of Scientific Instruments

A revisit to self-excited push pull vacuum tube radio frequency oscillator for ion sources and power measurements

L. R. Hlondo, B. Lalremruata, L. R. M. Punte, L. Rebecca, J. Lalnunthari, and H. H. Thanga

Citation: Review of Scientific Instruments **87**, 045101 (2016); doi: 10.1063/1.4944943
View online: http://dx.doi.org/10.1063/1.4944943
View Table of Contents: http://scitation.aip.org/content/aip/journal/rsi/87/4?ver=pdfcov
Published by the AIP Publishing

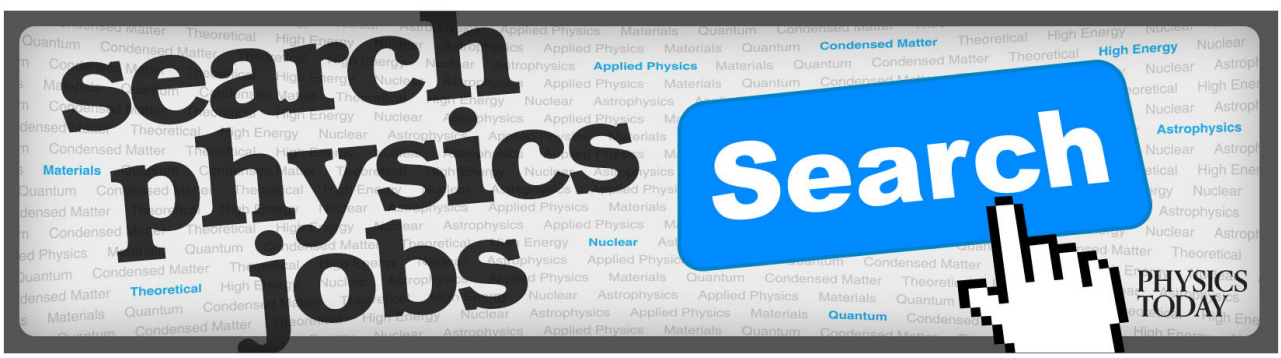

A revisit to self-excited push pull vacuum tube radio frequency oscillator for ion sources and power measurements

L. R. Hlondo, B. Lalremruata, L. R. M. Punte, L. Rebecca, J. Lalnunthari, and H. H. Thanga[a)]
Nuclear & Hydrogen Energy Research Group, Department of Physics, Mizoram University, Tanhril, Aizawl, Mizoram 796004, India

(Received 4 August 2015; accepted 16 March 2016; published online 1 April 2016)

Self-excited push-pull vacuum tube oscillator is one of the most commonly used oscillators in radio frequency (RF)-ion plasma sources for generation of ions using radio frequency. However, in spite of its fundamental role in the process of plasma formation, the working and operational characteristics are the most frequently skip part in the descriptions of RF ion sources in literatures. A more detailed treatment is given in the present work on the RF oscillator alone using twin beam power tetrodes 829B and GI30. The circuit operates at 102 MHz, and the oscillation conditions, stability in frequency, and RF output power are studied and analyzed. A modified form of photometric method and RF peak voltage detection method are employed to study the variation of the oscillator output power with plate voltage. The power curves obtained from these measurements are quadratic in nature and increase with increase in plate voltage. However, the RF output power as measured by photometric methods is always less than the value calculated from peak voltage measurements. This difference is due to the fact that the filament coil of the ordinary light bulb used as load/detector in photometric method is not a perfect inductor. The effect of inductive reactance on power transfer to load was further investigated and a technique is developed to estimate the amount of power correction needed in the photometric measurement result. © *2016 AIP Publishing LLC.* [http://dx.doi.org/10.1063/1.4944943]

I. INTRODUCTION

The use of radio frequency (RF) voltage to create plasma in ion sources dates back to the late 1940s.[1,2] Ion sources have widespread applications in industrial plasmas,[3] neutral-beam injection (NBI) systems for fusion devices,[4] bio-medical sciences,[5] particle accelerators,[6] and mass-spectrometry.[7] In an RF driven ion source, the high frequency electric field accelerates free electrons to energies that are high enough to ionize atoms or molecules with which they collide. The density of the plasma thus created depends on the RF signal frequency and power, and plays crucial role in the performance of the ion source.[8,9] Numerous works have been seen in the literature on the design and construction of RF ion sources.[6,9] However, these studies are mainly devoted to the extraction and different characteristics of plasma, and little attention has been paid towards RF oscillator itself.

Among the various design available, vacuum tube self-excited push-pull oscillator is one of the most commonly used RF signal generator in RF driven plasma source. Even though there are now more efficient semi-conductor based RF power sources, vacuum tube oscillator, especially self-excited push-pull RF generator, continues to occupy important place in the design and construction of RF ion sources due to its circuit simplicity, robustness, compactness, and ease of maintenance. However, electron tubes are high voltage devices and have operating conditions different from that of semiconductor devices. Therefore, proper understanding of the performance of such device is important for their application in ion sources. The present work aimed at providing a more detailed description of the oscillator system and operational characteristics of a self-excited push-pull oscillator using twin beam-power tetrode, constructed for operation at around 100 MHz.

In the operation of vacuum tube RF oscillator, the only parameter used to adjust the total output power level is the DC plate voltage. Thus, understanding the relationship between the two parameters is important for proper operation of the oscillator. To measure the output power of the oscillator, two simple and inexpensive techniques, namely, a modified form of photometric method and RF peak voltage detection method, were used. Photometric method is one of the oldest methods of RF power measurement in history. It is based on the ability of incandescent lamp to convert RF power into light which is then measured with a photometer.[10,11] However, this method is rather classified as power indicator than absolute power measurement due to the inductive reactance of the load at high frequency. On the other hand, the latter method is one of the standard and well-known methods where RF power is made to be absorbed by a purely resistive load and the electrical energy consumed is calculated from the RF signal peak voltage.

II. MATERIALS AND METHODS

A. Circuit description

Schematic circuit diagram of an RF oscillator used in this study is shown in Figure 1. The oscillator is based on the design reported by Moak *et al.*[12] The amplifying stage of the oscillator is an 829B twin beam-power tetrode connected in

a)Author to whom correspondence should be addressed. Electronic mail: hhthanga@yahoo.com

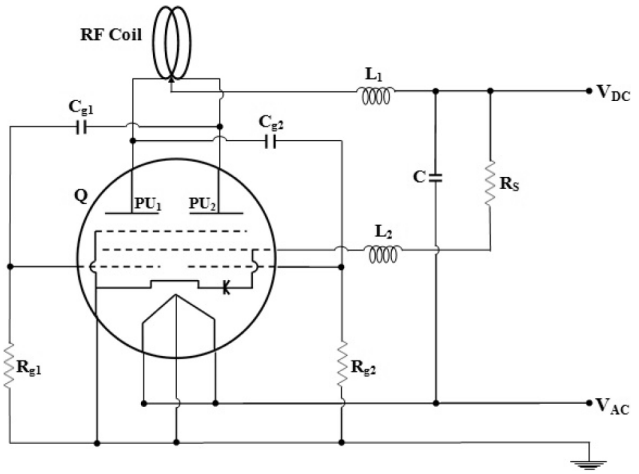

FIG. 1. Circuit diagram of RF oscillator. Q = 829B twin beam-power tetrode; RF coil: tube diameter = 0.6 cm, pitch = 1 cm, coil diameter = 7 cm; R_S = 20 kΩ, 20 W; $R_{g1} = R_{g2}$ = 6.8 kΩ, 1 W; $C_{g1} = C_{g2}$ = 1 pF, 1 kV; C = 50 μF; L_1 = 586 μH; L_2 = 589.5 μH.

push-pull arrangement with capacitive coupling to the control grid. The grid leak resistors R_{g1} and R_{g2} together with coupling capacitors C_{g1} and C_{g2} provide the necessary biasing to the grid. The LC frequency selector, also called RF coil or tank circuit, is made of copper tubing winded into two turns of coil. The parasitic or stray capacitance between the windings serves as the capacitive part of the LC tank circuit. The inductance and other parameter of the tank coil are calculated using a web-based calculator employing current-sheet coil geometrical formula[13,14] corrected for field non-uniformity and round wire.

In Figure 1, L_1, L_2, and C are the RF chokes and capacitor to prevent the dc source from RF signal interference. Resistor R_S provides the necessary biasing voltage to the screen grid, and it has to be of high wattage resistor not less than 20 W. Low wattage below 15 W results in excessive heating of the screen grid resistor and thus changing the resistance value and operating point of the tube.

DC power supply for the tube is obtained from a full-wave rectifier with centre-tapped 230 V–1 kV step-up transformer and RC filtering circuit as shown in Figure 2. Separate ac supply of proper voltage is employed to heat the filament. The applied plate voltage of the tube can be varied using a Variac (0-270 V) connected at the input of the step-up transformer.

The oscillator is naturally air cooled during operation, and the frequency of the RF signal is directly measured with frequency counter FC 2400. Conventional digital multimeters are used to measure voltage and current.

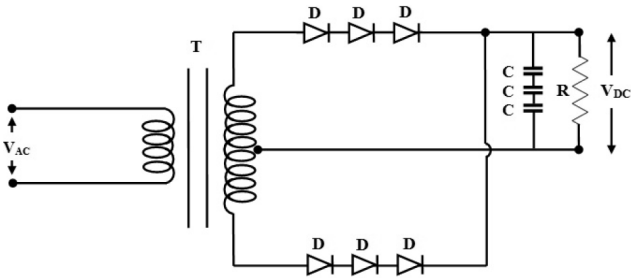

FIG. 2. Circuit diagram of 1 kV DC power supply. T = 100 VA step-up transformer; D = IN 4007, 700 V (PIV); C = 330 μF, 450 V; R = 1.18 MΩ.

III. POWER MEASUREMENT

A. Photometric method

The experimental setup for RF power measurement is shown in Figure 3. The method is based on the ability of incandescent light bulb to convert RF power directly into heat and light. The setup consists of an ordinary 100 Watt, 230 V light bulb "B" directly coupled to the RF tank coil using two parallel open wires of length 50 cm. Light emitted by the incandescent lamp is detected with a cadmium sulphide LDR (light-dependent resistor) photometer. For all measurements, LDR is kept at distance of 5 cm from the center of the bulb and V_{LDR} is fixed at 7 V. To achieve impedance matching between the source and the load, the positions of the two output tapping points in the RF coil are adjusted till maximum LDR current reading is indicated by the ammeter. With 100 W light bulb load, impedance matching is observed at 1/3rd of the coil center tapped point.

The LDR current reading at different light intensity is next calibrated into power with standard 50 Hz AC source using the following relation:

$$P = VI. \quad (1)$$

In the calibration process, the transmitter is replaced by a variable standard ac source and the brightness of the bulb is adjusted to give LDR current reading equal to that recorded with RF power. With this modified form of photometric method, the relative RF output power can be obtained at a more precise level.

However, the filament of incandescent lamp is coiled coil in structure, and as a result, the power value indicated by this measurement method will not be same if the load is purely resistive. To estimate the amount of power attenuated by the filament, inductors of different inductances are connected in series with a 100 W light bulb in a 50 Hz AC circuit, and the variation of AC power with inductive reactance is first studied at different applied voltage. The inductance of the external inductors used in this study varies from 14 mH to 415 mH according to direct measurement with Fluke PM6303A RCL meter at 1 kHz. From the relationship between inductive reactance and power delivered to the load, the amount of RF power attenuated by the filament reactance can be calculated as explained in Section III B.

The inductance of the filament is calculated from its physical dimension using Lundin's formula[15] as the 1 kHz RCL meter cannot be used for direct measurement. Following are the dimension of the filament obtained with a travelling

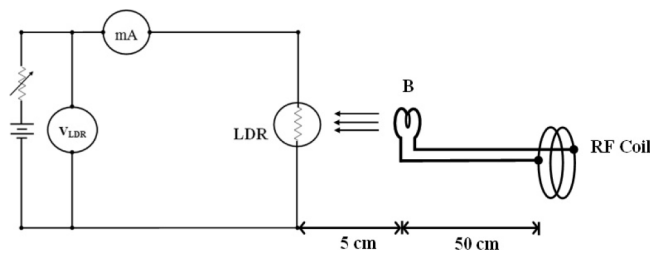

FIG. 3. Experimental setup for photometric method of RF power measurement.

microscope (VC = 0.001): length = 35 mm; bigger coil diameter = 0.8 mm (outer), pitch = 0.27 mm; smaller coil diameter = 0.12 mm; filament wire thickness = 0.05 mm; number of turns (bigger coil) = 96; number of smaller coil turns in the bigger coil = 22.

All power measurements using photometric method are conducted in a dark room to avoid interference from background light. Each measurement was repeated at least three times to check the consistency in our results, and the maximum uncertainty in power measurement is calculated to be about 2%.

B. Peak voltage detection method

In this method, the RF power is transferred to a purely resistive load of 50 Ω through a coaxial cable, and the voltage developed across the load is detected with a high speed diode as shown in Fig. 4. The diode rectifies the RF signal and converts it to a DC voltage, which can be read by a multimeter with good accuracy; the 1 nF capacitor is there to smooth the rectified DC signal presented to the meter. The voltage thus measured corresponds to the peak RF voltage and related to the RF power by the equation

$$P = V_p^2/2R, \text{ (W)} \quad (2)$$

where V_p = measured peak voltage + diode forward voltage drop which is 0.7 V for silicon, and R is 50 Ω. The high speed diode used to detect and rectify RF signal is 1N4148 having reverse recovery time of 4 ns. The 50 Ω dummy load is constructed out of 20 number of 1000 (1 W) carbon resistors connected in parallel between two circular copper coated PCB. The whole unit is then immersed in paraffin oil to further increase the power handling capacity. No appreciable change in temperature of the paraffin oil was observed during operation. Peak voltage measurement cannot be performed beyond 800 V due to the interference of the digital voltage measuring device by the high field RF signal.

IV. RESULTS AND DISCUSSION

A. Operating conditions

Figure 1 shows the circuit diagram of RF oscillator using twin beam-power tetrode 829B. The oscillator is basically a push-pull Hartley oscillator employing grid-leak biasing method. It has the operating frequency of 102 MHz, which corresponds to the fundamental frequency as all the even harmonics are cancelled out in push-pull oscillator. The oscillation frequency of the oscillator is primarily determined by the resonance frequency of the RF coil forming LC tank circuit and is given by

$$f = 1/2\pi\sqrt{(LC)}. \quad (3)$$

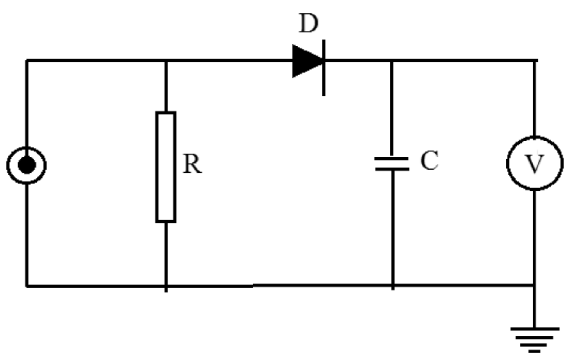

FIG. 4. Circuit diagram for peak voltage measurement with diode detector and dummy load (R = 50 Ω; D = 1N4148, 100 V PIV; C = 1 μF).

At 102 MHz, calculation using current-sheet coil geometrical formula[13] gives L = 0.36 μH and C = 2.46 pF, where C is the stray capacitance of the coil. Therefore the self-resonance frequency of the tank coil according to Eq. (1) is 169 MHz. But this is far above the observed frequency of oscillation. To get oscillation at 102 MHz with L = 0.36 μH, the value of C has to be 6.76 pF. The 4.3 pF difference in capacitance is very close to the inter-electrode capacitance of the tube, which is 4.4 pF according to calculation from the tube data sheet. This observation suggests that contribution from the inter-electrode capacitance should not be neglected while designing an RF coil to obtain operating frequency of desired value.

The values of R_g and C_g in the grid leak network determine the control grid biased voltage and hence the operating point of the tube. The amount of biased voltage depends on the amplitude, frequency of the signal, and grid leak time constant.[16] In high power RF oscillator, the RC time constant has to be kept at low value relative to the cycle time of the signal.[17] In our case, the grid leak time constant is 6.8 ns which is about one-half cycle of the operating frequency. When the value of grid leak resistor is changed from 6.8 kΩ to 22 kΩ, the frequency is observed to decrease by about 47 MHz. The decrease in frequency is due to occurrence of intermittent oscillation caused by large value of R_g. At high value of R_g and hence RC time, the biased voltage developed is too large that oscillation stops and restarts after the capacitor has discharged through R_g till proper grid biasing voltage is reached again.[17] Intermittent oscillation has frequency lower than the operating frequency.

Frequency and power stability are other important characteristics to consider in the operation of the oscillator. In the present oscillator, the operating frequency is found to decrease by about 1% as a result of loading, as well as tank coil oxidation. Tank coil oxidation is the formation of copper oxide layer on the surface of the RF coil. It increases the effective dielectric constant between the coil windings constituting the capacitive part of the tank circuit. Since the tank circuit determines the frequency of oscillation, any variation in the conditions of the external circuit will be coupled back into the frequency determining portion of the oscillator. These variations result in the above observed frequency instability. Tank coil oxidation is also found to reduce the output power by about 10% when compared with freshly polished tank coil. This is due to the higher electrical resistance of copper oxide layer leading to lower Q value of the coil. Thus to avoid power reduction due to tank coil oxidation, all power measurements were conducted after cleaning the copper tank coil external surface with sander paper. The efficiency of the oscillator including power supply unit is also measured and found to be 37%.

B. RF output power and measurements

The variation of output power with plate voltage of the 829B tube is investigated using two different techniques—a modified form of photometric method and RF peak voltage detection method. The modification made in the present photometric setup is the application of LDR as light sensor to improve the sensitivity and accuracy level of the relative power measurement. LDR is semiconductor device whose resistance decreases with the intensity of light incident on it. However, the dependence of LDR resistance on light intensity is not linear and varies as bL^{-a},[18] where L is the incident power per unit area; a and b are constants that depend on the material and shape of the resistor. LDR has spectral response almost similar to human eye and the low temperature coefficient. According to our measurement, the change in LDR current per degree Celsius is only about 0.02 mA. But incandescent light bulb wasted most part of the input energy in the form of heat and only less than 5% is converted into visible light. Therefore, RF power converted into heat will not be detected by LDR. However, the calibration method eliminates all the needs to consider the undetected part of the RF power dissipated in the filament except light.

Figure 5 shows the dependence of RF output power levels on plate voltages according to the two measurement methods for 829B and its equivalent, GI30. It can be seen that as the plate voltage increases, the RF output power also increases accordingly and so saturation is seen within the range of measurement. However, the variation of output power with plate voltage is non-linear and can be described by quadratic function. The nature of the power curve is attributed to LDR and diode detector responses towards the intensity of light and RF signal, respectively. The RF power directly indicated by the present measurement technique is 79% ± 2% watts at 900 V. This is higher than the value reported by Moak *et al.*,[12] which is 60 W for the same circuit configuration and plate voltage, even though the power measurement technique or instrument used by Moak is not known.

However, when compared with peak voltage method, the photometric result is lower by about 11 W on the average. The discrepancy between the two power readings cannot be due to the tube characteristics of 829B as similar result is observed with its equivalent GI30. As stated before, the power measured by photometric method corresponds to RF power that actually dissipated in the form of heat and light by the filament of the incandescent lamp. However, due to the imperfection (not pure inductive reactance) of the filament, there is always some amount of RF power that is neither converted into heat nor light even under the condition of perfect impedance matching. On the other hand, the dummy load used in the peak voltage method is purely resistive and there is no complication from inductance. Therefore, the discrepancy between power readings of the two methods is attributed to arise from the inductive reactance of the filament of light bulb load in photometric technique. To further confirm this, the inductive reactance of the filament is calculated directly from its physical dimension, and the amount of RF power attenuated by it is estimated from the variation of 50 Hz AC power consumed by 100 W light bulb in the presence of different series inductors.

Figure 6 shows the plot of ac power vs inductive reactance in a 50 Hz AC circuit for different inductances, with linear fittings to the data points. Each curve corresponds to a given value of applied AC voltage to the light bulb load. The different curves appear to be parallel suggesting that the inductor attenuation coefficient represented by the slope of the curve is independent of the applied voltages. Therefore, the relationship between AC power and inductive reactance can be described by the following linear equation:

$$P = P_d - 0.13X_L, \tag{4}$$

where P is the ac power in watt and X_L is the series inductive reactance in the circuit. The slope in Eq. (3) is the average of the four straight line fits to the experimental data. P_d is the intercept on power axis which corresponds to ac power consumed by the load without series inductor. Assuming the inductor attenuation coefficient to be the same in RF region, the amount of power correction required to apply in photometric method will be $0.13X_L$, where X_L is the inductive reactance of the filament at 102 MHz.

The inductance of the filament calculated according to straight solenoid approximations is 141 nH and 284 nH,

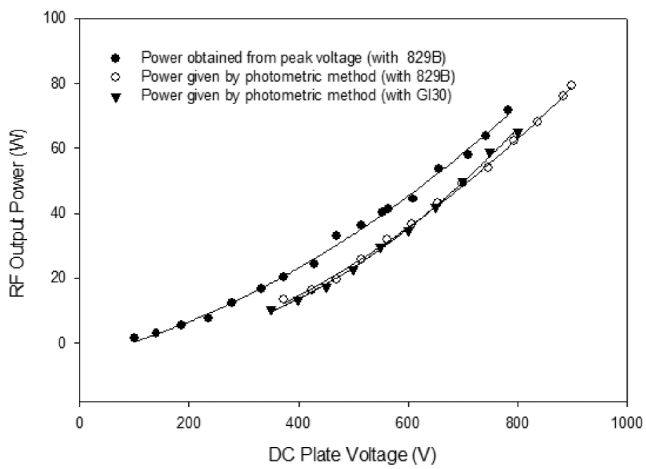

FIG. 5. Variation of RF output power with plate voltages (350-900 V) for 829B and GI30 according to photometric and peak voltage measurements.

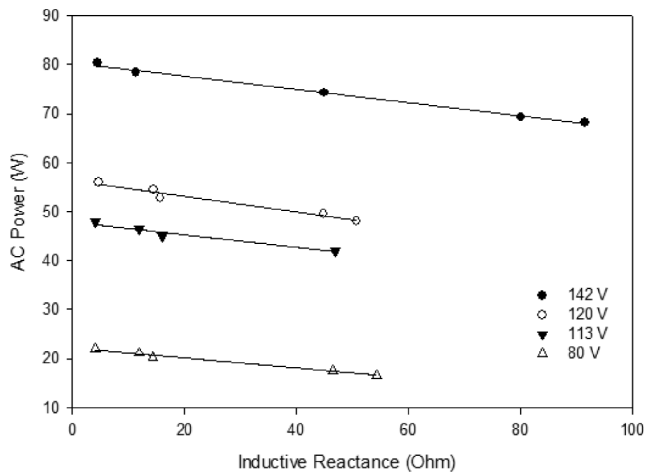

FIG. 6. Variation of AC power dissipated by 100 W incandescent lamp at different values of inductive reactance and applied voltages.

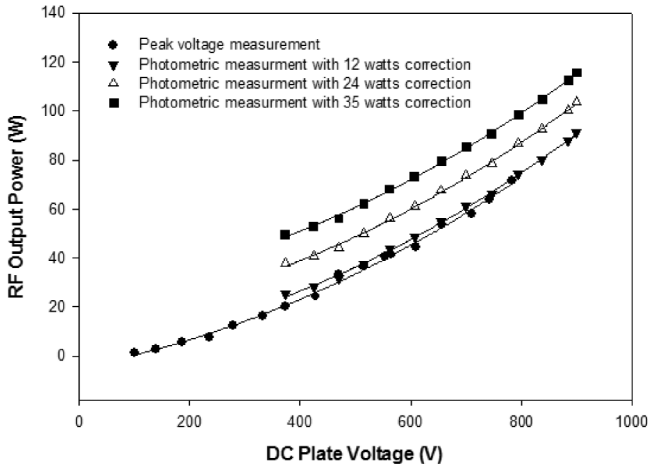

FIG. 7. Comparison of RF power measured by peak voltage and photometric methods after correction for the effect of filament inductive reactance.

respectively, for the bigger and smaller coil of the filament. As the two inductances are in series in the filament structure, the equivalent inductance of 425 nH for the series combination can also be the effective inductance of the filament as a whole. Toroidal approximation is also applied but gives the same inductance as that of the inner coil. Thus, we have three different possible values of inductance for the filament, which can result in power attenuation of 12, 24, and 35 W.

In Figure 7, comparison is made again between power calculated from RF peak value and photometric result after applying the above possible power corrections. It can be seen that among the different possible photometric power curves, the one having 12 W power correction is closest to the power curve obtained from peak voltage measurement methods. Therefore, we can conclude that the power difference of about 11 W observed between the two measurement methods in Fig. 5 is due to the fact that the filament is not a perfect inductor. Thus, the power level directly indicated by photometric method using 100 W filament light bulb as RF signal detector in the measurement has to be further corrected for about 12 W to bring its accuracy level to that of peak voltage measurement. Accordingly, the total output power of the oscillator at 900 V plate voltages would be 90 W instead of 79 W. Power correction of 12 W comes from the inductive reactance X_L of the bigger coil alone having inductance 141 nH, further suggesting that the effective inductance of the filament in incandescent lamp is largely determined by the inductance of the bigger coil. It is also interesting to see that the corrected total output power is in very good agreement with the reported maximum power rating of 90 W for class C push pull oscillator using 829B tube under natural cooling according to the tube data sheet.

V. CONCLUSION

In the present work, a self-excited push pull RF oscillator is constructed using 829B vacuum tube. The oscillator has operating frequency of 102 MHz, which is quite stable with respect to loading and tank coil oxidation. However, copper oxide layer formation on RF coil surface could result in a decrease of RF output power as much as 10%. The variation of RF output power with plate voltage is studied using two power measurement techniques—photometric and RF peak voltage methods. As the plate voltage increases, the output power increases in a non-linear fashion, which can be best described by quadratic function. However, inductive component present in the load/detector of photometric method is found to cause decrease in power readings. The effective inductance of the filament appears to be largely determined by the bigger coil structure, and the resulting power attenuation is estimated to be about 12 W when compared with power value obtained from peak voltage measurement. Therefore, the total output power of the oscillator comes out to be ~91 W at 900 V plate voltage, which is about 31 W higher than the power value reported by Moak.

[1]P. C. Thonemann, J. Moffat, O. Roaf, and J. H. Saunders, Proc. Phys. Soc., London **61**, 483 (1948).
[2]R. N. Hall, Rev. Sci. Instrum. **19**, 905 (1948).
[3]H. R. Kaufman, J. J. Cuomo, and J. M. E. Harper, J. Vac. Sci. Technol. **21**, 725 (1982).
[4]U. Fantz, P. Franzen, W. Kraus, M. Berger, S. Christ-Koch, M. Fröschle, R. Gutser, B. Heinemann, C. Martens, P. McNeely, R. Riedl, E. Speth, and D. Wünderlich, Plasma Phys. Controlled Fusion **49**, B563 (2007).
[5]D. Schardt, T. Elsässer, and D. Schulz-Ertner, Rev. Mod. Phys. **82**, 383 (2010).
[6]I. G. Brown, *The Physics and Technology of Ion Sources*, 2nd ed. (Wiley-VCH, Berlin, 2004).
[7]R. S. Houk, V. A. Fassel, G. D. Flesch, H. J. Svec, A. L. Gray, and C. E. Taylor, Anal. Chem. **52**, 2283 (1980).
[8]X.-M. Zhu, W.-C. Chen, S. Zhang, Z.-G. Guo, D.-W. Hu, and Y.-K. Pu, J. Phys. D: Appl. Phys. **40**, 7019 (2007).
[9]S. K. P. Tripathi, P. Pribyl, and W. Gekelman, Rev. Sci. Instrum. **82**, 93501 (2011).
[10]R. L. Conhaim, Electronics World **70**(4), 53 (1963).
[11]Fundamentals of single-side band communication, Departments of the Army and the Air Force, Washington DC, Technical Manual TM 11-685/TO 31R-1-9, 119, 1961.
[12]C. D. Moak, H. Reese, Jr., and W. M. Good, Nucleonics **9**(3), 18 (1951).
[13]See http://www.hamwaves.com/antennas/inductance.html for RFinductance calculator.
[14]K. L. Corum and J. F. Corum, IEEE Microwave Rev. **7**(2), 36 (2001).
[15]R. Lundin, Proc. IEEE **73**(9), 1428 (1985).
[16]F. E. Terman, *Electronic and Radio Engineering*, 4th ed. (McGraw Hill Book Company, 1955), p. 489.
[17]G. J. Pridham, *Electronic Devices and Circuits* (Pergamon Press, 1972), p. 305.
[18]P. Regtien, F. van der Heijden, M. J. Korsten, and W. Otthius, *Measurement Science for Engineers* (Kogan Page Science, 2004), p. 188.

Science and Technology Journal, Vol. 4 Issue: I ISSN: 2321-3388

Study of the Operational Characteristics of Self-excited Push–Pull Vacuum Tube Oscillator for R.F. Ion Sources

L.R. Hlondo, B. Lalremruata and H.H. Thanga*
Nuclear & Hydrogen Energy Research Group, Department of Physics,
Mizoram University, Tanhril–796004, Aizawl, Mizoram, India
E-mail: *hthanga@yahoo.com

ABSTRACT—In the present work, we report the construction and analysis of a very simple radio-frequency (RF) generator suitable for use in ion sources. It is a self-excited push-pull RF oscillator constructed using 829B or GI30 twin beam-power tetrode valve. As RF oscillator is one of the most frequently skip part in the descriptions of RF ion sources in literatures, we conducted systematic study on the working of the oscillator to understand its operational characteristics. The oscillation conditions, stability in frequency and variation of RF output power with plate voltage are investigated to understand its operational characteristics. A modified form of photometric is employed to measure the RF output power of the oscillator. At 102 MHz and 900V plate voltage, the power delivered to the load is measured to be79 watts which is 19 watts higher than the value reported earlier in literature for similar circuit configuration.

Keywords: RF Oscillator, Self-excited Push Pull Oscillator, Twin Beam Power Tetrode, Operating Conditions, Power Measurement, Photometric Method

INTRODUCTION

The use of RF voltage to create plasma in ion sources dates back to the late 1940s [1,2]. Ion sources have widespread applications in industrial plasmas [3], neutral-beam injection (NBI) systems for fusion devices [4], bio-medical sciences [5], particle accelerators [6], and mass-spectrometry [7]. In an RF driven ion source, the high frequency electric field accelerates free electrons to energies that are high enough to ionize atoms or molecules with which they collide. The density of the plasma thus created depends on the RF signal frequency and power, and plays crucial role in the performance of the ion source [8,9]. Numerous works have been reported in literature on the design and construction of RF ion sources [6,9]. However, these studies are mainly devoted to the extraction and different characteristics of plasma, and little attention has been paid towards RF oscillator.

Among the various design available, vacuum tube self-excited push-pull oscillator is one of the most commonly used RF signal generator in radio frequency (RF) driven plasma source. Even though there are now more efficient semi-conductor based RF power sources, vacuum tube oscillator, especially self-excited push-pull RF generator continues to occupy important place in the design and construction of RF ion sources due to its circuit simplicity, robustness, compactness and ease of maintenance. As electron tubes are high voltage devices and have operating conditions different from that of semiconductor devices, proper understanding of the performance of such device is important for their application in ion sources. Therefore, in the present work, we have constructed self-excited push-pull oscillator using twin beam-power tetrode for operation at around 100 MHz and study the different operational characteristics of the oscillator.

MATERIAL AND METHODS

Circuit Description

Schematic circuit diagram of an RF oscillator used in this study is shown in Fig. 1. The oscillator is based on the

design reported by Moak *et al*. [10]. The amplifying stage of the oscillator is a twin beam-power tetrode connected in push-pull arrangement with capacitive coupling to the control grid. The grid leak resistors R_{g1} and R_{g2}together with coupling capacitors C_{g1} and C_{g2} provide the necessary biasing to the grid. The LC frequency selector, also called RF coil or tank circuit, is made of copper tubing winded into two turns of coil. The parasitic or stray capacitance between the windings serves as the capacitive part of the LC tank circuit. The inductance and other parameter of the tank coil are calculated using a web-based calculator [11] employing current-sheet coil geometrical formula that is corrected for field non-uniformity and round wire [12,13].

In Fig. 1, L_1, L_2, C are the RF chokes and capacitor to prevent the dc source from RF signal interference. Resistor R_S provides the necessary biasing voltage to the screen grid and it has to be of high wattage resistor not less than 20W. Low wattage below 15W results in excessive heating of the screen grid resistor, and thus changing the resistance value and operating point of the tube.

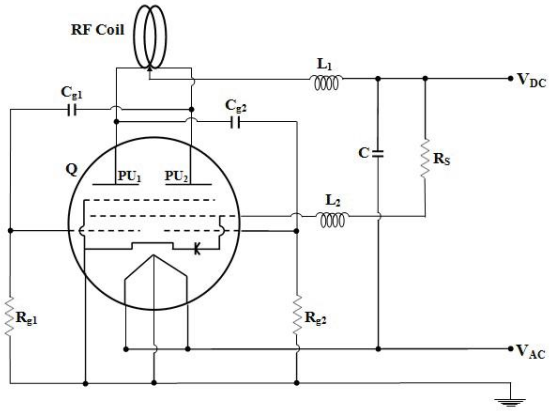

Fig. 1: Circuit Diagram of RF Oscillator. Q = 829B/GI30 Twin Beam-Power Tetrode; RF Coil: Tube Diameter = 0.6 cm, pitch = 1 cm, coil diameter = 7 cm; R_S = 20 kΩ, 20 W; $R_{g1} = R_{g2}$ = 6.8 kΩ, 1 W; $C_{g1} = C_{g2}$ = 1 pF, 1 kV; C = 50 µF, L_1= 586 µH; L_2= 589.5 µH.

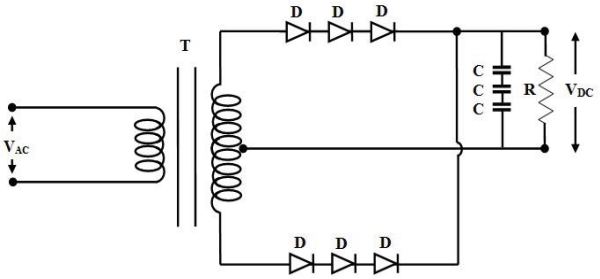

Fig. 2: Circuit Diagram of 1 kV DC Power Supply. T = 100 VA Step-Up Transformer; D = IN 4007, 700 V (PIV); C = 330 µF, 450 V; R = 1.18 MΩ.

DC power supply for the tube is obtained from a full-wave rectifier with centre-tapped 230V to 1kV step-up transformer and RC filtering circuit as shown in Fig. 2. Separate ac supply of proper voltage is employed to heat the filament. The applied plate voltage of the tube can be varied using a Variac (0-270 V) connected at the input of the step-up transformer.

The oscillator is naturally air cooled during operation and the frequency of the RF signal is directly measured with frequency counter FC 2400. Standard digital multimeters were used measured voltage and current.

PHOTOMETRIC METHOD OF RF POWER MEASUREMENT

To measure the RF output power, a modified form of photometric method is employed. The method is based on the ability of incandescent lamp to convert RF power into light that is then measured with a photometer [14,15].The modification made in the present setup is the application of LDR as light sensor to improve the sensitivity and precision level of the measurement method. LDR is semiconductor device whose resistance decreases with the intensity of light incident on it. However, the dependence of LDR resistance on light intensity is not linear and varies as bL^{-a} [16], where L is the incident power per unit area, *a* and *b* being constants that depend on the material and shape of the resistor

The experimental setup for RF power measurement is shown in Fig. 3. The setup consists of an ordinary 100 Watt, 230 V light bulb 'B' directly coupled to the RF tank coil using two parallel open wires of length 50 cm. Light emitted by the incandescent lamp is detected with a cadmium sulphide LDR (light-dependent resistor) photometer. For all measurements, LDR is kept at distance of 5 cm from the center of the bulb and V_{LDR} is fixed at 7 V. To achieve impedance matching between the source and the load, the positions of the two output tapping points in the RF coil are adjusted till maximum LDR current reading is indicated by the ammeter. With 100 watt light bulb load, impedance matching is observed at 1/3rdof the coil center tapped point.

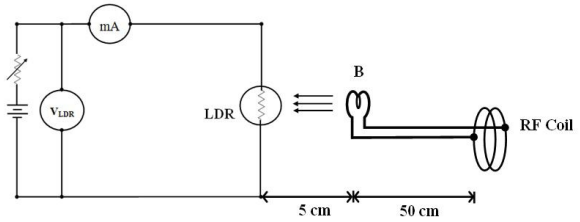

Fig. 3: Experimental Setup for RF Power Measurement

The LDR current reading at different light intensity is then calibrated using standard ac source of 50 Hz. In the calibration method, the transmitter is replaced by a variable standard ac source and the brightness of the bulb is adjusted to give LDR current reading equal to that recorded with RF power. After brightness adjustment is done, the value of ac power calculated from P=VI is then just equal to the RF power absorbed by the filament.

All power measurements were conducted in a dark room to avoid interference from background light. Each measurement was repeated at least three times to check the consistency in our results and the maximum uncertainty in power measurement is calculated to be about 2%. Moreover, all measurements were conducted after the copper tank coil was first polished with sander paper to avoid the effect of tank coil oxidation.

RESULTS AND DISCUSSION

Operating Conditions

Fig. 1 shows the circuit diagram of RF oscillator using twin beam-power tetrode 829B. The oscillator is basically a push-pull Hartley oscillator employing grid-leak biasing method. It has the operating frequency of 102 MHz, which corresponds to the fundamental frequency as all the even harmonics are cancelled out in push-pull configuration. The oscillation frequency of the oscillator is primarily determined by the resonance frequency of the RF coil forming LC tank circuit andis given by

$$f = 1/2\pi\sqrt{(LC)}, \quad (1)$$

At 102 MHz calculation using current-sheet coil geometrical formula [11] gives L = 0.36 μH and C = 2.46 pF, where C is the stray capacitance of the coil. Therefore the self-resonance frequency of the tank coil according to Eq. (1) is 169 MHz. But this is far above the observed frequency of oscillation. To get oscillation at 102 MHz with L = 0.36 μH, the value of C has to be 6.76 p. The 4.3pF difference in capacitance is very close to the inter-electrode capacitance of the tube, which is 4.4 pF according to calculation from the tube data sheet [17]. This observation suggests that contribution from the inter-electrode capacitance should not be neglected while designing an RF coil to obtain operating frequency of desired value.

The values of R_g and C_g in the grid leak network determine the control grid bias voltage and hence the operating point of the tube. The amount of bias voltage depends on the amplitude, frequency of the signal and grid leak time constant [18]. In high power RF oscillator, the RC time constant has to be kept at low value relative to the cycle time of the signal [19]. In our case, the grid leak time constant is 6.8 ns which is about one-half cycle of the operating frequency. When the value of grid leak resistor is changed from 6.8 kΩ to 22 kΩ, the observed frequency decreased by about 47 MHz. The decrease in frequency is due to occurrence of intermittent oscillation caused by large value of R_g. At high value of R_g and hence RC time, the bias voltage developed is too large that oscillation stops, and restarts after the capacitor has discharged through R_g till proper grid biasing voltage is reached again [17]. Intermittent oscillation has frequency lower than the operating frequency.

Frequency and power stability are other important characteristics to consider in the operation of the oscillator. In the present oscillator, the operating frequency is found to decrease by about 1% as a result of loading, as well as tank coil oxidation. Tank coil oxidation is the formation of copper oxide layer on the surface of the RF coil. It increases the effective dielectric constant between the coil windings constituting the capacitive part of the tank circuit. Since the tank circuit determines the frequency of oscillation, any variation in the conditions of the external circuit will be coupled back into the frequency determining portion of the oscillator. These variations result in the above observed frequency instability. Tank coil oxidation is also found to reduce the output power by about 10%. This is due to the higher electrical resistance of copper oxide layer leading to lower Q value of the coil. The efficiency of the oscillator including power supply unit is also measured and found to be 37%.

RF OUTPUT POWER

LDR has spectral response almost similar to human eye and the low temperature coefficient. According to our measurement, the change in LDR current per degree Celsius is only about 0.02 mA. But incandescent light bulb wasted most part of the input energy in the form of heat and only less than 5% is converted into visible light. Therefore, RF power converted into heat will not be detected by LDR. However, the calibration method eliminates all the needs to consider the undetected part of the RF power dissipated in the filament except light.

Fig. 4 shows the plot of RF output power at different plate voltages using 829B and its equivalent, GI30. It can be seen that both tubes have almost the same performance within their respective operating conditions. As the plate

voltage increases the RF output power also increases accordingly and no saturation is seen within the range of measurement. However, the variation of output power with plate voltage is not linear and can be best described by a quadratic function. The nature of the power can be attributed to the characteristic of LDR response towards the intensity of light. The RF power directly indicated by the present measurement technique is 79 ± 2% watts at 900V. This is much higher than the value reported by Moak *et al*. [10], which is 60 watts for the same circuit configuration and plate voltage. However, the method or device used by Moak for power measurement was not shown in the report. Even then, we can say from our result that the modified technique is more sensitive than their, which could only be attributed to the introduction on LDR detector.

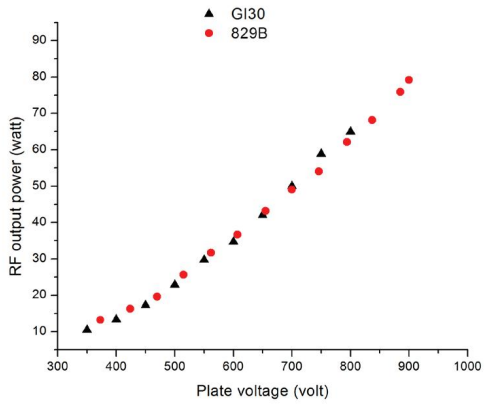

Fig. 4: Variation of RF Output Power with Plate Voltages (350-900 V) for 829B and GI30

At this power level, the oscillator is able to excite low pressurehydrogen and neon discharge tube through inductive coupling as shown below in Fig. 5.

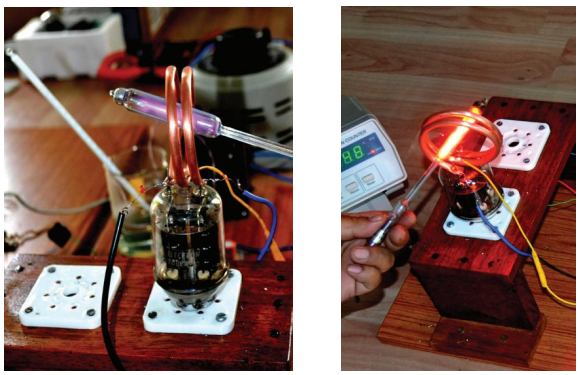

Fig. 5: Pictures Illustrating Excitation of Low Pressure (a) Hydrogen and (b) Neon Discharge Tubes by RF Field Produced by the Oscillator

CONCLUSION

In the present work, a self-excited push pull RF oscillator is constructed using 829B vacuum tube. The oscillator has operating frequency of 102 MHz and is quite stable with respect to loading, tank coil oxidation and changes of vacuum tubes of equivalent types. However, copper oxide layer formation on RF coil surface could result in a decrease of RF output power as much as 10%. The variation of RF output power with plate voltage is non-linear characteristic of LDR response. The RF power measured using our modified technique is about 79 watts that is 19 watts higher than the value reported earlier in literature for similar circuit configuration. The difference is attributed to the increase in sensitivity due to the introduction of LDR detector in the modified techniques

REFERENCES

1. Thonemann, P.C., Moffat, J., Roaf, D. and Sanders, J.H. (1948), "The Performance of a New Radio-frequency Ion Source", *Proc. Phys. Soc.,* London, Vol. 61, pp. 483–485.
2. Hall, R.N. (1948), "High Frequency Proton Source", *Rev. Sci. Instrum*., Vol. 19, pp. 905–910.
3. Kaufman, H.R., Cuomo, J.J. and Harper, J.M.E. (1982), "Technology and Applications of Broad-Beam Ion Sources used in Sputtering, Part I. Ion Source Technology", *J. Vac. Sci. Technol*., Vol. 21, pp. 725–736.
4. Fantz, U., Franzen, P., Kraus, W., Berger, M., Christ-Koch, S., Froschle, M., Gutser, R., Heinemann, B., Martens, C., McNeely, P., Riedl, R., Speth, E. and Wünderlich, D. (2007), "Negative Ion RF Sources for ITER NBI: Status of the Development and Recent Achievements", *Plasma Phys. Control. Fusion,* Vol. 49, pp. B563–580.
5. Schardt, D., Elsässer, T. and Schulz-Ertner, D. (2010), "Heavy-ion Tumor Therapy: Physical and Radiobiological Benefits", *Rev. Mod. Phys*., Vol. 82, pp. 383–425.
6. Brown, I.G. (2004), "*The Physics and Technology of Ion Sources*, Second Ed. Wiley-VCH, Berlin.
7. Houk, R.S., Fassel, V.A., Flesch, G.D., Svec,H., Gray, A.L. and Taylor, C.E. (1980), "Inductively Coupled Argon Plasma as an Ion Source for Mass Spectrometric Determination of Trace Elements", *Anal. Chem*., Vol. 52, pp. 2283–2289.
8. Zhu, Xi-Ming, Chen, Wen-Cong, Zhang, Shu, Guo, Zhi-Gang, Hu, Da-Wei and Pu, Yi-Kang (2007), "Electron Density and Ion Energy Dependence on Driving Frequency in Capacitively Coupled Argon Plasmas", *J. Phys. D: Appl. Phys*., Vol. 40, pp. 7019–7023.
9. Tripathi, S.K.P., Pribyl, P. and Gekelman, W. (2011), "Development of a Radio-frequency Ion Beam Source for Fast-ion Studies on the Large Plasma Device", *Rev. Sci. Instrum*., Vol. 82, 93501.
10. Moak, C.D., Reese, H., Jr. and Good, W.M. (1951), "Design and Operation of a Radio-Frequency Ion Source for Particle Accelerators", *Nucleonics,* Vol. 9, No. 3, pp. 18–23.

11. Single-Layer Helical Round Wire Coil Inductor Calculator [Internet], Available from: http://www.hamwaves.com/antennas/inductance.html.
12. Corum, K.L. and Corum, J.F. (2001), "RF Coils, Helical Resonators and Voltage Magnification by Coherent Spatial Modes", *Microwave Review*, *IEEE*, Vol. 7, No. 2, pp. 36–45.
13. Lundin, R. (1985), *A Handbook Formula for the Inductance of a Single-layer Circular Coil, Proc. IEEE*, Vol. 73, No. 9, pp. 1428–1429.
14. Coheim, R.L. (1963), "R.F. Power Output Measurements", *Electronics World,* Vol. 70, No. 4, pp. 53–57.
15. Fundamentals of Single-side Band Communication (1961), Departments of the Army and the Air Force, Washington DC, Technical Manual, TM 11-685/TO 31R-1-9, p. 119.
16. Regtien, P., Van Der Heijden, F., Korsten, M.J. and Otthius, W. (2004), "Measurement Science for Engineers", *Kogan Page Science*, p. 188.
17. Harrison, N.J., "Electron Tube Division", *Radio Corporation of America, 829B Twin Beam Power Tube Data*, pp. 7–63.
18. Terman, F.E. (1955), *Electronic and Radio Engineering*, Fourth Ed., McGraw Hill Book Company, p. 489.
19. Pridham, G.J. (1972), *Electronic Devices and Circuits*, Pergamon Press, p. 305.

Available online at www.sciencedirect.com

ScienceDirect

Nuclear Physics A ••• (••••) ••••••

NUCLEAR PHYSICS A

www.elsevier.com/locate/nuclphysa

Entrance channel effects on the alpha decay probabilities of neutron and proton induced reactions for target mass A=55

L.R. Hlondo, B. Lalremruata *

Department of Physics, Mizoram University, Tanhril-796004, Aizawl, Mizoram, India

Received 1 June 2019; received in revised form 13 January 2020; accepted 2 April 2020

Abstract

In the present work, we investigate the entrance channel effects on the alpha decay probabilities for the neutron and proton induced reactions for target mass A=55 from few MeV up to 20 MeV. In particular, we studied two combinations, ^{55}Fe(n,α)^{52}Cr and ^{55}Mn(p,α)^{52}Cr; ^{55}Mn(n,α)^{52}V and ^{55}Cr(p,α)^{52}V reactions. Each combination is producing the same compound nucleus at the same excitation energy, but with different J^{π} distributions. We investigate how the difference in the J^{π} distributions of the compound nuclei at the same excitation energy formed by the neutron and proton induced reactions influence the alpha decay channel. The theoretical simulation is done using the nuclear reaction code TALYS-1.9. The results are compared with experimental results whenever available, and are discussed in detail.

Keywords: Entrance channel effects; J^{π} mismatch; Alpha decay probability; Weisskopf-Ewing limit

1. Introduction

A complete nuclear data for all isotopes are desirable for nuclear astrophysics, safe reactor design, transmutation, understanding nuclear structure and reaction dynamics, improving existing nuclear model parameters for better predictivity, industrial and medical applications. However,

* Corresponding author.
E-mail address: marema08@gmail.com (B. Lalremruata).

https://doi.org/10.1016/j.nuclphysa.2020.121844
0375-9474/

Please cite this article in press as: L.R. Hlondo, B. Lalremruata, Entrance channel effects on the alpha decay probabilities of neutron and proton induced reactions for target mass A=55, Nucl. Phys. A (2020), https://doi.org/10.1016/j.nuclphysa.2020.121844

due to the fact that some isotopes are unstable and short-lived, or the reaction cross section itself is very small, it is sometimes impossible or difficult to measure their cross sections directly with the present technology.

Ghoshal in 1950 [1] performed an experiment to study the excitation functions of ^{64}Zn formed between proton and alpha particle induced reactions on ^{63}Cu and ^{60}Ni respectively. He established the validity of Bohr's independent hypothesis that the decay of compound nucleus does not depend on its mode of formation.

Since the 1970's, surrogate method had been utilized successfully for neutron induced fission cross section measurements [2–22]. Recently, the surrogate ratio method was also used to measure the ^{55}Fe(n,p) reaction cross section in the incident energy range 7.9–20.1 MeV [23]. A lot of efforts have also been given to extend the surrogate method for other reaction channels such as for neutron capture cross sections and theoretical investigations have been performed [24]. Experimental investigations have also been performed for well known neutron capture reactions [25–29]. Recently, Boutoux et al. [30] performed experiment for ^{172}Yb(n,γ) and ^{175}Lu(n,γ) with ^{174}Yb(^{3}He,$\alpha\gamma$)^{173}Yb and ^{174}Yb(^{3}He,pγ)^{176}Lu reactions as their surrogates respectively. They observed large discrepancies in the gamma decay branching ratio between the surrogate and the desired neutron induced reactions. This large discrepancy is attributed to the fact that gamma decay probabilities are very sensitive to the mismatch in the J^{π} distributions between the compound nucleus formed by the surrogate and desired reaction. They reported that the average compound nucleus spin is 3–4$\hbar$ higher in the surrogate reaction than the neutron induced reaction. Scielzo et al. [31] also performed experiments to investigate the reliability of ^{153,155,157}Gd(n,γ) reactions using the surrogate reactions ^{154,156,158}Gd(p,p'). They also observed large deviation in the gamma emission probabilities from the direct and surrogate reactions. They concluded that in order to extract reliable (n,γ) cross sections, a more sophisticated analysis should be developed that takes into account angular momentum differences between the neutron induced and surrogate reactions.

In nuclear reactor developments, the generation of hydrogen and helium through neutrons have always been a very serious problem. In addition to the production of hydrogen and helium, the other processes such as atomic displacements and transmutations, etc. can produce microstructural defects in the material. The structural material, generally stainless steel, comprises of Fe, Ni, Cr, Mn, Co and Nb. The high production rate of ^{55}Fe ($T_{1/2} = 2.744$ yr [32]) from the neutron exposure of natural iron via the threshold reaction ^{56}Fe(n,2n)^{55}Fe is of main concern as an activation product during the lifetime of an operating reactor [33]. The neutron induced reactions on ^{55}Fe and other long-lived radionuclides, however, are difficult to measure using the standard activation techniques due to their low activities. For this purpose and other applications, the values of total cross-sections for the production of charged particles in the reactor materials through nuclear reactions induced by different projectiles in the energy range from few keV to 20 MeV are required [34].

In the present work, we explore the possibility of using a simple (p,α) reactions to extract reliable (n,α) reactions using statistical nuclear reaction model simulation in the incident energy range from above 1 MeV up to 20 MeV. We investigate how the same compound nucleus at the same excitation energy produced by different entrance channels with different J^{π} distributions influence the alpha decay channel. In particular, we are studying two combinations, i) ^{55}Fe(n,α)^{52}Cr and ^{55}Mn(p,α)^{52}Cr, ii) ^{55}Mn(n,α)^{52}V and ^{55}Cr(p,α)^{52}V reactions. It can be seen that both the ^{55}Fe(n,α)^{52}Cr and ^{55}Mn(p,α)^{52}Cr reactions form the same compound nucleus ^{56}Fe. The projectiles neutron and proton are spin 1/2 particles, and the target spins are 3/2 and 5/2 for ^{55}Fe and ^{55}Mn respectively and they both have negative parity. Similarly, ^{55}Mn(n,α)^{52}V

Please cite this article in press as: L.R. Hlondo, B. Lalremruata, Entrance channel effects on the alpha decay probabilities of neutron and proton induced reactions for target mass A=55, Nucl. Phys. A (2020), https://doi.org/10.1016/j.nuclphysa.2020.121844

and ^{55}Cr(p,α)^{52}V reactions also produced the same compound nucleus, which is ^{56}Mn. The target spins are 5/2 and 3/2 for ^{55}Mn and ^{55}Cr respectively and they both have negative parity. There are no measured cross sections for ^{55}Fe(n,α)^{52}Cr and ^{55}Mn(p,α)^{52}Cr reactions to validate our theoretical results. However, there are sufficient number of experimental cross sections for ^{55}Mn(n,α)^{52}V reactions [35–53] in the EXFOR Database [54], to validate our extracted theoretical results for ^{55}Mn(n,α)^{52}V reaction using the ^{55}Cr(p,α)^{52}V reaction.

2. Methodology

According to the compound nucleus theory, the decay of the compound nucleus is independent of how it is formed. However, it is known that due to the different J^{π} distributions of the compound nuclei formed by different entrance channels, a particle decay probabilities can be very different. In this work, we investigate how the J^{π} distributions of the compound nuclei formed by the neutron induced and proton induced reactions influence the alpha decay channel for the reactions mentioned above.

In the Weisskopf-Ewing (WE) limit of the Hauser-Feshbach compound nucleus theory, it is assumed that the decay branching ratios are independent of the compound nucleus angular momentum and parity [55]. We can therefore write the expression for the neutron induced reaction referred here as 'reference' by

$$\sigma_{n\alpha}(E_n) = \sigma_n^{CN}\left(E^*\right) G_{\alpha}\left(E^*\right) \tag{1}$$

where $\sigma_n^{CN}(E^*) = \sum_{J^{\pi}} \sigma_n^{CN}(E^*, J^{\pi})$ is the compound nucleus formation cross section at the excitation energy E^* in the neutron induced reaction which can be calculated easily with a suitable optical potential, and $G_{\alpha}(E^*)$ is the alpha branching ratio of the compound nucleus produced by neutron induced reaction.

Similarly, the proton induced reaction which produced the same compound nucleus at the same excitation energy, and decay into the same outgoing channel as the neutron induced reaction can also be expressed as

$$\sigma_{p\alpha}(E_p) = \sigma_p^{CN}\left(E^*\right) G'_{\alpha}\left(E^*\right) \tag{2}$$

where $\sigma_p^{CN}(E^*) = \sum_{J^{\pi}} \sigma_p^{CN}(E^*, J^{\pi})$ is the compound nucleus formation cross section in the proton induced reaction which can also be calculated easily with a suitable optical potential, and $G'_{\alpha}(E^*)$ is the alpha branching ratio of the compound nucleus produced by proton induced reaction.

In the WE limit, the branching ratios in Eq. (1) and Eq. (2) are similar, which is experimentally measurable alpha decay probability from the proton induced reaction. Hence, we can write the decay probability as

$$P^{decay}(E^*) = G_{\alpha}\left(E^*\right) = G'_{\alpha}\left(E^*\right) \tag{3}$$

By utilizing Eq. (3), the neutron induced reaction cross section can be extracted by using the proton induced reaction referred as 'extracted' by

$$\sigma'_{n\alpha}(E_n) = \sigma_n^{CN}\left(E^*\right) G'_{\alpha}\left(E^*\right) \tag{4}$$

where symbols have their usual meanings.

If the neutron induced cross section given by Eq. (1) is taken as reference, and under the Hauser-Feshbach formalism of compound nucleus reaction calculation with the valid assumption

Please cite this article in press as: L.R. Hlondo, B. Lalremruata, Entrance channel effects on the alpha decay probabilities of neutron and proton induced reactions for target mass A=55, Nucl. Phys. A (2020), https://doi.org/10.1016/j.nuclphysa.2020.121844

of the WE limit, this reference cross section should be the same as the extracted (n,α) cross section from the proton induced reaction using Eq. (4).

For the reactions considered in the present work, since the preequilibrium contributions are significant especially above 7 MeV incident energy, their contributions have to be taken into account. Escher et al. [2] suggested that the best way to account for the missing preequilibrium contribution is to perform model calculations of the reference reaction with ($\sigma_{n\alpha}^{CN+PE}$) and without ($\sigma_{n\alpha}^{CN}$) preequilibrium, and to multiply the ratio of the two model calculations with the cross sections extracted using Eq. (4) of the present manuscript. This can be implemented by extending Eq. (4) as follows

$$\sigma'_{n\alpha}(E_n) = \sigma_n^{CN}\left(E^*\right) G'_{\alpha}\left(E^*\right) R \tag{5}$$

where $R = \frac{\sigma_{n\alpha}^{CN+PE}}{\sigma_{n\alpha}^{CN}}$ and other symbols have their usual meanings as in Eq. (4).

In the present work, the compound nucleus formation cross sections in both the neutron and proton induced reactions are calculated using the nuclear reaction code TALYS-1.9 [56]. In TALYS-1.9, the compound nuclear reaction calculations are done in the statistical Hauser-Feshbach formalism [55] with the optical potentials which are the local and global parameterisations of Koning and Delaroche [57]. Theoretical calculations for the neutron and proton induced reactions are performed for the same set of nuclear models and model parameters in TALYS-1.9 from few MeV to 20 MeV incident energy in the steps of 1 MeV. There are six different level density models available in TALYS-1.9. They are (1) LDM-1: the constant temperature and Fermi-gas model where the constant temperature model is used in the low excitation region and the Fermi gas model is used in the high excitation energy region. The transition energy is around the neutron separation energy, (2) LDM-2: the back-shifted Fermi gas model, (3) LDM-3: the generalized superfluid model, (4) LDM-4: the microscopic level densities (Skyrme force) from Goriely's tables [58], (5) LDM-5: the microscopic level densities (Skyrme force) from Hilaire's combinatorial tables [58], (6) LDM-6: the microscopic level densities (temperature dependent Hartree-Fock-Bolyubov, Gogny force) from Hilaire's combinatorial tables [59]. In Talys-1.9, there are eight different choices of gamma ray strength functions. They are: (1) Gamma ray strength function 1 (strength 1): Kopecky-Uhl generalized Lorentzian [60], (2) Gamma ray strength function 2 (strength 2): Brink [61] and Axel Lorentzian [62], (3) Gamma ray strength function 3 (strength 3): Hartree-Fock BCS tables [58], (4) Gamma ray strength function 4 (strength 4): Hartree-Fock-Bogolyubov tables [58], (5) Gamma ray strength function 5 (strength 5): Goriely's hybrid model [63], (6) Gamma ray strength function 6 (strength 6): Goriely temperature-dependent Hartree-Fock-Bogolyubov. (7) Gamma ray strength function 7 (strength 7): Temperature dependent relativistic mean field. (viii) Gamma ray strength function 8 (strength 8): Gogny D1M Hartree-Fock-Bogolyubov+QRPA.

Theoretical calculations are also carried out with and without width fluctuation corrections. However, we do not observe difference in the results with and without width fluctuation corrections in the energy ranged considered.

3. Results and discussion

3.1. The $^{55}Mn(n,\alpha)^{52}V$ reaction

Fig. 1 shows the neutron and proton transmission coefficients on ^{55}Mn and ^{55}Cr targets respectively calculated using local optical potential by Koning and Delaroche for several partial

Please cite this article in press as: L.R. Hlondo, B. Lalremruata, Entrance channel effects on the alpha decay probabilities of neutron and proton induced reactions for target mass A=55, Nucl. Phys. A (2020), https://doi.org/10.1016/j.nuclphysa.2020.121844

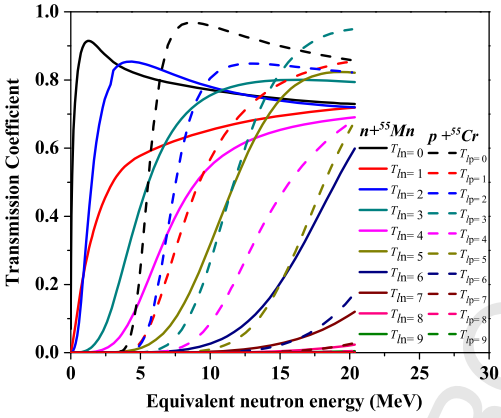

Fig. 1. Transmission coefficients of neutron on ^{55}Mn and proton on ^{55}Cr. (For interpretation of the colors in the figure(s), the reader is referred to the web version of this article.)

waves. Fig. 2 shows comparison of J^π distributions of the ^{56}Mn compound nuclei formed by the ^{55}Mn(n,α)^{52}V and ^{55}Cr(p,α)^{52}V reactions at equivalent neutron energies of 5, 10, 15 and 20 MeV. Although calculations are carried out from threshold to 20 MeV in the steps of 1 MeV, only few selected results are plotted as the trends are similar. In Fig. 2, the figures on the left panel are the angular momentum distributions for the positive parity and the figures on the right panel are for the negative parity. The figure labels also indicate the average angular momentum $< J^\pi >= \frac{\sum_J \sigma^{CN}(E^*, J^\pi) J dJ}{\sum_J \sigma^{CN}(E^*, J^\pi) dJ}$ in both the neutron and proton induced reactions. It can be seen from Fig. 2 that the angular momentum distributions of the ^{56}Mn compound nuclei formed by the neutron and proton induced reactions are very similar and the average angular momentum difference is also less than $2\hbar$ for all the positive and negative parities, throughout the energy range considered. This similar angular momentum distribution is a result of the features in Fig. 1. In Fig. 2, at 5 MeV equivalent energy, the main contributions are from s, p, d, f, g and h-waves as shown in Fig. 1, in the case of neutron absorption. The J^π population of ^{56}Mn after neutron absorption on ^{55}Mn(5/2$^-$) is therefore dominated by 0^-, 1^-, 2^-, 3^-, 4^-, 5^-, 6^-, 7^- and 0^+, 1^+, 2^+, 3^+, 4^+, 5^+, 6^+, 7^+, 8^+. Similarly, for the proton absorption in ^{55}Cr(3/2$^-$), the main contributions are from s, p and d-waves as seen in Fig. 1. The J^π population of ^{56}Mn is dominated by 1^-, 2^-, 3^-, 4^- and 1^+, 2^+, 3^+. As the incident energy increases, higher angular momenta contribute resulting in the increase of the $< J >$ value as shown in Fig. 2. The decrease of the difference in the $< J >$ between the two incident channels as the energy increases can also be understood from Fig. 1.

To optimize the models and parameters used in Talys-1.9, we performed calculations using six different level density models and eight different gamma ray strength functions available in Talys-1.9 which are compared with available experimental data [35–53] taken from EXFOR database [54] and evaluated data taken from evaluated nuclear data libraries TENDL-2017 [64] and ENDF/B-VII.0 [65] which is shown in Fig. 3. It can be seen that the reference cross section obtained using LDM4 best match the available experimental data and the evaluated nuclear data files of TENDL-2017 and ENDF/B-VII.0 whereas the gamma ray strength functions do not have significant effects for a given level density model. Therefore, the Talys-1.9 calculation with level density model 4 (LDM4) and the default gamma ray strength function (strength 1) are chosen

Please cite this article in press as: L.R. Hlondo, B. Lalremruata, Entrance channel effects on the alpha decay probabilities of neutron and proton induced reactions for target mass A=55, Nucl. Phys. A (2020), https://doi.org/10.1016/j.nuclphysa.2020.121844

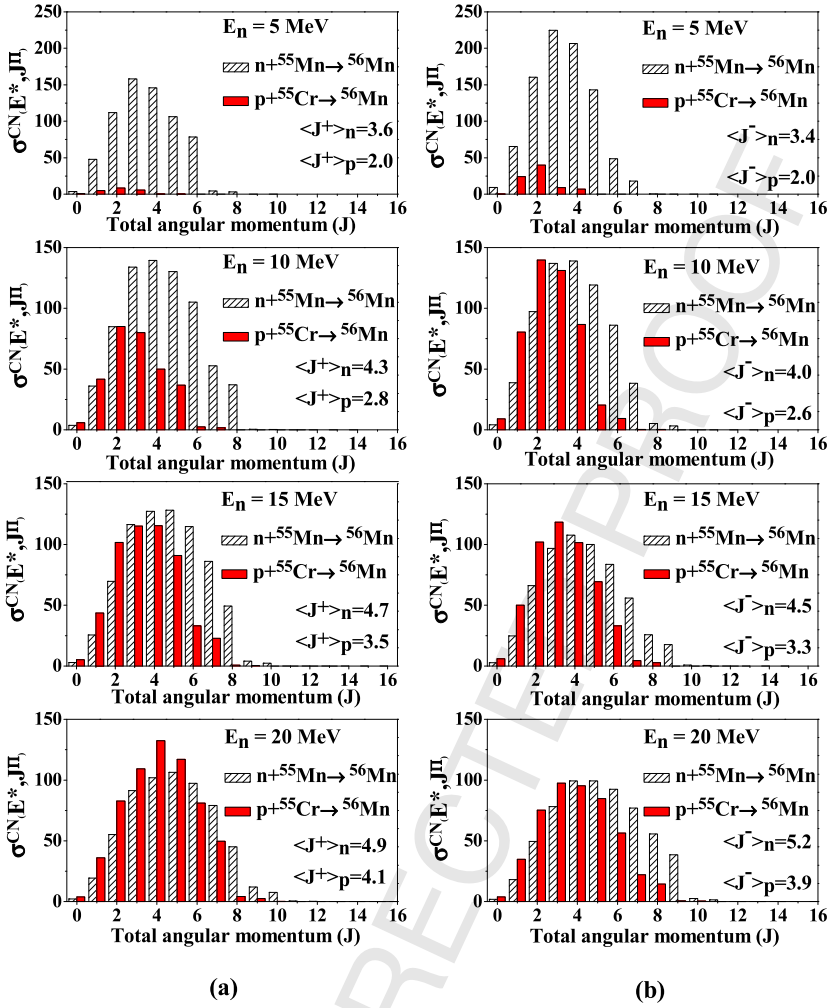

Fig. 2. Comparison of the J^{π} distributions of the ^{56}Mn compound nuclei formed by the neutron and proton induced reactions. The left panel is for positive parity and the right panel is for negative parity.

as the 'Reference Model' or "benchmark" and this is compared with the extracted cross section. The same model and model parameters are adopted for all the reactions considered in this work.

Fig. 4 shows comparison between the alpha decay branching ratios of the ^{56}Mn compound nuclei formed by the neutron and proton induced reactions using the reference model. It can be seen that the alpha decay branching ratios obtained from the ^{56}Mn compound nuclei formed by these two reactions match perfectly throughout the energy ranged considered. These results show that although ^{56}Mn compound nuclei were formed by the neutron and proton induced reactions with the averaged angular momentum mismatch less than $2\hbar$ throughout the energy range considered, this mismatch do not show significant influence on the alpha decay probabilities.

Fig. 5 shows comparison between the reference (n,α) reaction cross section including both compound nucleus and preequilibrium contributions and the extracted (n,α) reaction cross sections from the proton induced alpha decay branching ratio using Eq. (5). As is already

Please cite this article in press as: L.R. Hlondo, B. Lalremruata, Entrance channel effects on the alpha decay probabilities of neutron and proton induced reactions for target mass A=55, Nucl. Phys. A (2020), https://doi.org/10.1016/j.nuclphysa.2020.121844

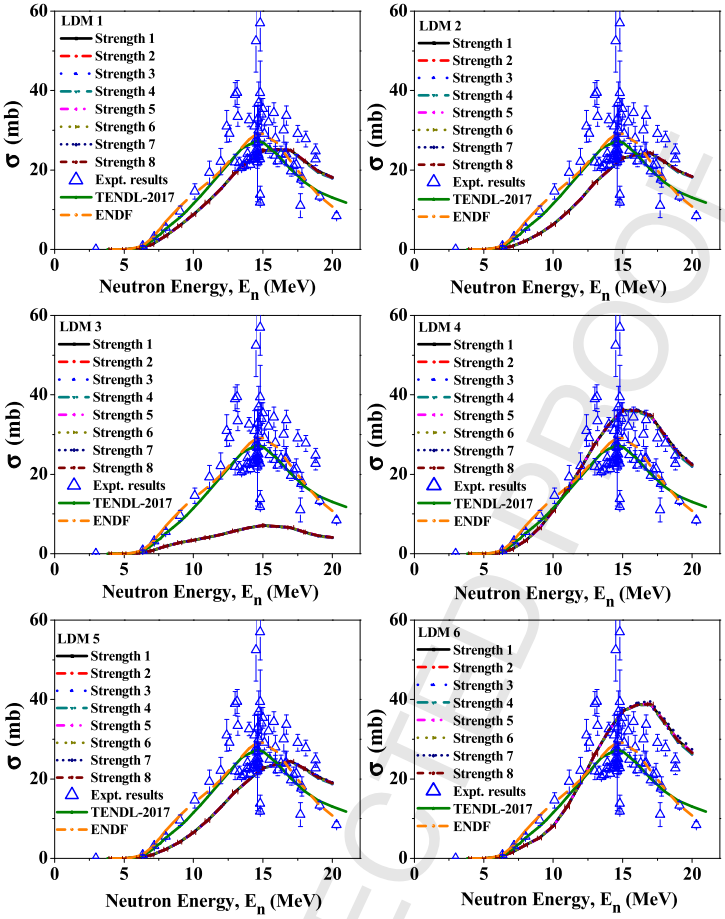

Fig. 3. Comparison between the reference ^{55}Mn(n,α)^{52}V reaction cross section calculated using all the available level density models and gamma ray strength functions in TALYS-1.9, the available experimental data taken from EXFOR database and the evaluation data of TENDL-2017 and ENDF/B-VII.0.

obvious from Fig. 4, we observed good agreement between the reference ^{55}Mn(n,α)^{52}V reaction cross sections with the extracted neutron induced reaction cross sections from the ^{55}Cr(p,α)^{52}V reaction which also agrees well with the experimental cross sections. This result shows that reliable and accurate ^{55}Mn(n,α)^{52}V reaction cross section can be measured or extracted with the ^{55}Cr(p,α)^{52}V reaction and vice versa. ^{55}Cr is unstable ($T_{1/2}$ = 3.497 mins [9]), and can be produced in reactor environments using ^{54}Cr(n,γ), ^{53}Cr(n,γ)^{54}Cr(n,γ), ^{52}Cr(n,γ)^{53}Cr(n,γ)^{54}Cr(n,γ) etc channels. Since Chromium is structural elements in fission and fusion reactors, accurate knowledge of neutron or proton induced reaction cross sections for its stable as well as unstable isotopes is very important. It is also worth noting that due to the availability of sufficient experimental cross sections for ^{55}Mn(n,α)^{52}V reaction, this information can be utilized to validate or use as evaluation tool for the ^{55}Cr(p,α)^{52}V reaction cross section for the evaluated nuclear data libraries as shown in the present work.

Please cite this article in press as: L.R. Hlondo, B. Lalremruata, Entrance channel effects on the alpha decay probabilities of neutron and proton induced reactions for target mass A=55, Nucl. Phys. A (2020), https://doi.org/10.1016/j.nuclphysa.2020.121844

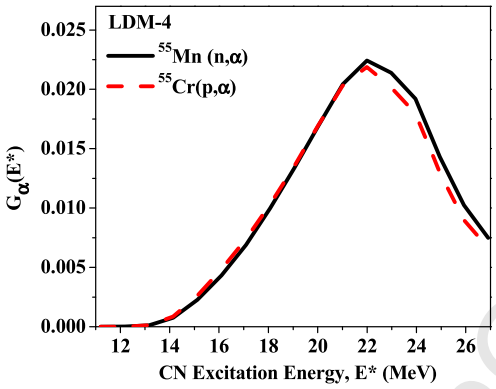

Fig. 4. Comparison between the alpha decay branching ratio of the ^{56}Mn compound nuclei from the ^{55}Mn(n,α)^{52}V and ^{55}Cr(p,α)^{52}V reactions.

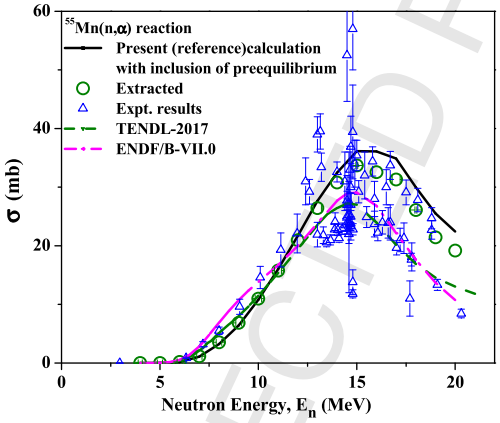

Fig. 5. Comparison between the reference ^{55}Mn(n,α)^{52}V reaction cross section including both compound nucleus and preequilibrium contributions calculated using LDM4, and the extracted neutron induced reaction cross sections from the proton induced reactions using Eq. (5) labelled as "Extracted", the available experimental data taken from EXFOR and the evaluation data of TENDL-2017 and ENDF/B-VII.0.

3.2. *The ^{55}Fe(n,α)^{52}Cr reaction*

Similar to Fig. 1 and 2, the neutron and proton transmission coefficients on ^{55}Fe and ^{55}Mn along with the J^π distributions of the ^{56}Fe compound nuclei formed by the ^{55}Fe(n,α)^{52}Cr and ^{55}Mn(p,α)^{52}Cr reactions are shown in Fig. 6 and 7 at equivalent incident neutron energies 5, 10, 15 and 20 MeV. Again, calculations are carried out from 1-20 MeV in the steps of 1 MeV. It can be seen from Fig. 7 that the angular momentum distributions of the ^{56}Fe compound nuclei formed by the neutron and proton induced reactions are very similar and the average angular momentum difference is less than 0.5$\hbar$ for all the positive and negative parities, throughout the energy range considered. Again as in the case of ^{55}Mn(n,α)^{52}V and ^{55}Cr(p,α)^{52}V reactions, this similar angular momentum distribution is a result of the features of partial waves in Fig. 6. In Fig. 7, at 5 MeV incident energy, the J^π population of ^{56}Fe after neutron absorption on ^{55}Fe(3/2$^-$) is dominated by 0$^-$, 1$^-$, 2$^-$, 3$^-$, 4$^-$, 5$^-$, 6$^-$ and 0$^+$, 1$^+$, 2$^+$, 3$^+$, 4$^+$, 5$^+$, 6$^+$,7$^+$.

Please cite this article in press as: L.R. Hlondo, B. Lalremruata, Entrance channel effects on the alpha decay probabilities of neutron and proton induced reactions for target mass A=55, Nucl. Phys. A (2020), https://doi.org/10.1016/j.nuclphysa.2020.121844

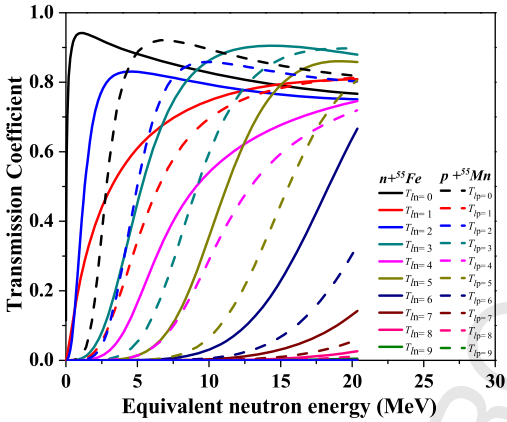

Fig. 6. Transmission coefficients of neutron on ^{55}Fe and proton on ^{55}Mn.

These J^{π} states of the compound nucleus are populated predominantly after neutron absorption that can be reached by s,p,d,f,g and h-waves capture which can be seen from Fig. 6. Similarly, at the same equivalent energy of 5 MeV, the J^{π} population of ^{56}Fe after proton absorption on ^{55}Mn(5/2$^-$) is dominated by 0^-, 1^-, 2^-, 3^-, 4^-, 5^-, 6^-,7^- and 0^+, 1^+, 2^+, 3^+, 4^+, 5^+, 6^+,7^+ after s,p,d,f,g and h-waves capture shown in Fig. 6. The averaged J^{π} distribution of the ^{56}Fe compound nucleus formed is almost similar from the neutron and proton induced reactions even at low incident energies compared to the previous case where the difference in $< J^+ >$ at 5 MeV incident energy is 1.6$\hbar$. Although the Projectile-Target spins and parity are very similar in both the cases, the much lower difference in $< J^+ >$ for the ^{55}Fe(n,α)^{52}Cr and ^{55}Mn(p,α)^{52}Cr reactions compared to ^{55}Mn(n,α)^{52}V and ^{55}Cr(p,α)^{52}V reactions may be attributed to the much higher neutron and proton separation energies, 11.197 MeV and 10.184 MeV in n + ^{55}Fe $\rightarrow$ ^{56}Fe* and p + ^{55}Mn $\rightarrow$ ^{56}Fe* systems respectively whereas the neutron and proton separation energies are 7.270 MeV and 9.091 MeV for n + ^{55}Mn $\rightarrow$ ^{56}Mn* and p + ^{55}Cr $\rightarrow$ ^{56}Mn* systems respectively. Therefore, even at low incident energies, the compound nuclei formed are populated at high excitation energies resulting into similar J^{π} distributions of compound nucleus.

Fig. 8 shows the alpha decay branching ratios of the ^{56}Fe compound nuclei formed by the ^{55}Fe(n,α)^{52}Cr and ^{55}Mn(p,α)^{52}Cr reactions. Again the branching ratios from this two different entrance channels match perfectly throughout the energy ranged considered. These results again show that the small J^{π} difference in the compound nuclei formed by the neutron and proton induced reactions do not exhibit significant influence in the alpha decay probabilities of the ^{56}Fe compound nucleus. As is again obvious from Fig. 8, we observed a very good match between the reference cross sections and the extracted cross sections using Eq. (5) as shown in Fig. 9. The agreement between the decay branching ratios in the case of ^{55}Fe(n,α)^{52}Cr and ^{55}Mn(p,α)^{52}Cr reactions is better compared to ^{55}Mn(n,α)^{52}V and ^{55}Cr(p,α)^{52}V reactions which is a result of a much lower J^{π} mismatch in the former case.

3.3. Study on the dependence of the alpha branching ratios on the level structure of residual nuclei

In the present work, the influence of the level structure of the nuclei produced after alpha emission has been studied. The residual nucleus ^{52}Cr is stable. However the residual nucleus ^{52}V

Please cite this article in press as: L.R. Hlondo, B. Lalremruata, Entrance channel effects on the alpha decay probabilities of neutron and proton induced reactions for target mass A=55, Nucl. Phys. A (2020), https://doi.org/10.1016/j.nuclphysa.2020.121844

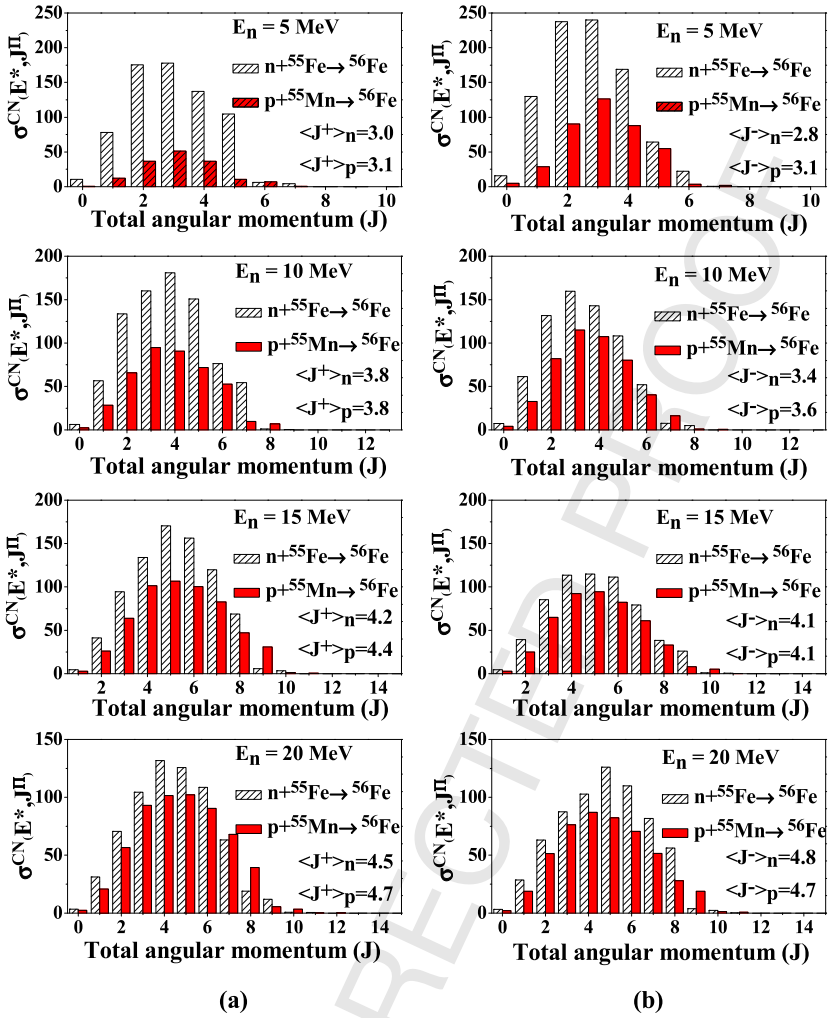

Fig. 7. Comparison of the J^{π} distributions of the ^{56}Fe compound nuclei formed by neutron and proton induced reactions (a) for the positive parity and (b) for the negative parity.

is unstable. Both the decay data and level structures are well known and are available in ENSDF. The plots of cumulative energy levels/MeV in the discrete region also show a good exponential growth without any abrupt break showing that the discrete energy levels are complete.

^{52}V has many low lying energy levels, the first excited state is 17.2 keV whereas ^{52}Cr has very low number of low lying energy levels, the first excited state is 1.434 MeV. Although the J^{π} mismatch is large within 2$\hbar$ in ^{55}Mn(n,α)^{52}V and ^{55}Cr(p,α)^{52}V reactions, however, due to large number of low lying states in the residual nucleus ^{52}V, the alpha decay probability do not depend much on the CN J^{π}. However, in the case of ^{55}Fe(n,α)^{52}Cr and ^{55}Mn(p,α)^{52}Cr reactions, although the number of low lying energy states are low, the J^{π} distribution of the CN ^{56}Fe is almost similar within 0-0.3 $\hbar$ difference even at low incident energies resulting in almost similar alpha decay branching ratio.

Please cite this article in press as: L.R. Hlondo, B. Lalremruata, Entrance channel effects on the alpha decay probabilities of neutron and proton induced reactions for target mass A=55, Nucl. Phys. A (2020), https://doi.org/10.1016/j.nuclphysa.2020.121844

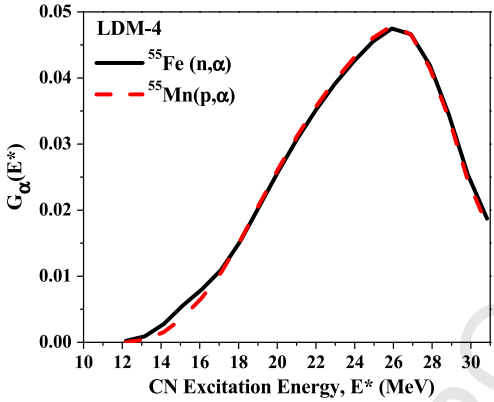

Fig. 8. Comparison between the alpha decay branching ratios of the ^{56}Fe compound nuclei formed by the ^{55}Fe(n,α)^{52}Cr and ^{55}Mn(p,α)^{52}Cr reactions.

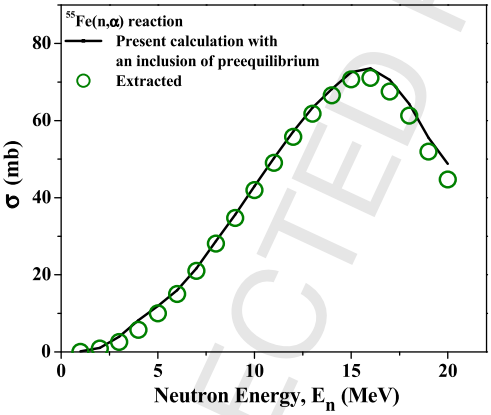

Fig. 9. Comparison between the reference ^{55}Fe(n,α)^{52}Cr reaction cross section including both compound nucleus and preequilibrium contributions calculated using LDM4 and the extracted cross section obtained using Eq. (5) labelled as "Extracted".

To study the dependence on the level structure of the residual nuclei at low energy, we performed calculations in which we force the TALYS code to adopt level structure of ^{52}Cr (which has very low number of low lying energy levels) for ^{52}V rather the existing level structure of ^{52}V (which has large number of low lying energy levels) for ^{55}Mn(n,α)^{52}V and ^{55}Cr(p,α)^{52}V reactions which are shown in the Fig. 10 given below. We observe that the alpha decay branching ratio very much depend on the level structure of the residual nucleus. One can also observe that the discrepancy reduces as the excitation energy increases, and the decay branching ratio is almost independent on the low lying level structure at high excitation energies.

In Fig. 11, we show the comparison between alpha decay branching ratio for ^{55}Mn(n,α)^{52}V and ^{55}Cr(p,α)^{52}V reactions where ^{55}Cr(p,α)^{52}V is forced to use level structure of ^{52}Cr. We see large difference in the alpha decay branching ratio between the two. This indicates that the alpha decay branching ratio depend on the level structure of the low lying energy levels of the residual nucleus.

Please cite this article in press as: L.R. Hlondo, B. Lalremruata, Entrance channel effects on the alpha decay probabilities of neutron and proton induced reactions for target mass A=55, Nucl. Phys. A (2020), https://doi.org/10.1016/j.nuclphysa.2020.121844

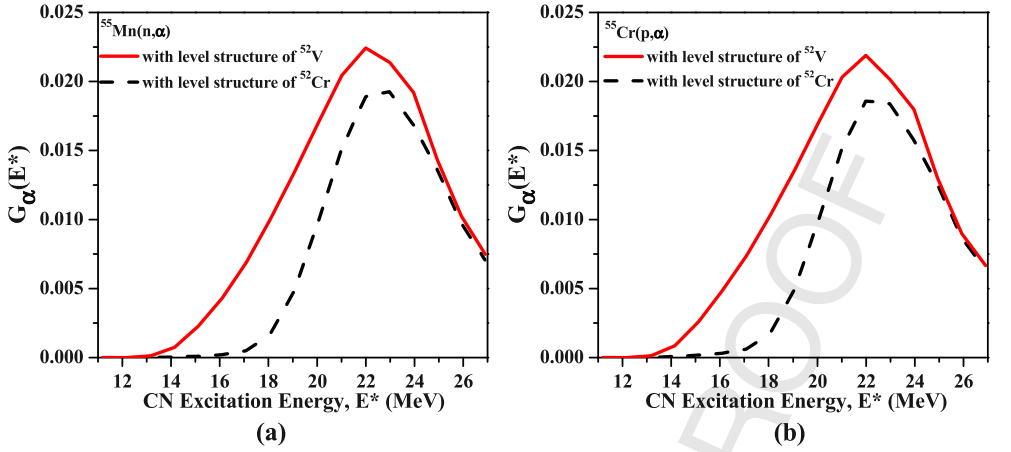

Fig. 10. Comparison of alpha decay branching ratio for ^{55}Mn(n,α)^{52}V and ^{55}Cr(p,α)^{52}V reactions with the level structure of ^{52}V and ^{52}Cr respectively.

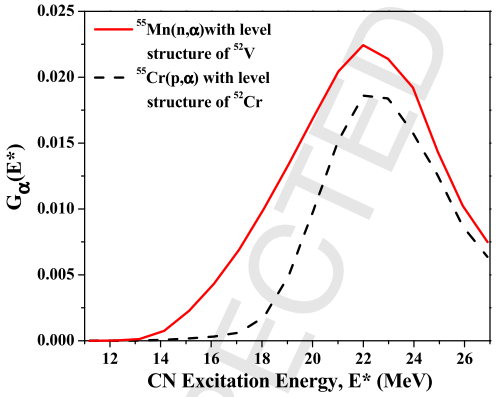

Fig. 11. Comparison of alpha decay branching ratio for ^{55}Mn(n,α)^{52}V and ^{55}Cr(p,α)^{52}V reactions where ^{55}Cr(p,α)^{52}V is forced to use level structure of ^{52}Cr.

4. Summary and conclusion

The entrance channel effect on the alpha decay probabilities for neutron and proton induced reactions has been studied for two reaction combinations (i) ^{55}Mn(n,α)^{52}V and ^{55}Cr(p,α)^{52}V, which produced the same compound nucleus ^{56}Mn, (ii) ^{55}Fe(n,α)^{52}Cr and ^{55}Mn(p,α)^{52}Cr, which produced the same compound nucleus ^{56}Fe. It is observed that the averaged angular momentum difference are within $2\hbar$ between the compound nuclei ^{56}Mn formed by neutron induced reaction on ^{55}Mn and proton induced reaction on ^{55}Cr throughout the energy range considered. Similarly, it is also observed that a very similar J^π distributions with the averaged angular momentum difference within $0.5\hbar$ between the compound nuclei ^{56}Fe formed by neutron induced reaction on ^{55}Fe and proton induced reaction on ^{55}Mn throughout the energy range considered. It is also found that a small difference in the J^π distributions of the compound nucleus do not influence significantly the alpha decay probabilities in the energy range and reactions considered.

Please cite this article in press as: L.R. Hlondo, B. Lalremruata, Entrance channel effects on the alpha decay probabilities of neutron and proton induced reactions for target mass A=55, Nucl. Phys. A (2020), https://doi.org/10.1016/j.nuclphysa.2020.121844

We therefore concluded that (p,α) reactions can be used to extract (n,α) reaction cross sections and vice versa for the target isotopes studied in the present work.

In the systems that we studied, we have very similar Projectile-Target spin-parity systems, resulting in very similar J^{π} distributions of compound nucleus. Moreover, the projectile separation energies in these systems are high, 11.197 MeV and 10.184 MeV in n + ^{55}Fe $\rightarrow$ ^{56}Fe* and p + ^{55}Mn $\rightarrow$ ^{56}Fe* systems respectively whereas the neutron and proton separation energies are 7.270 MeV and 9.091 MeV for n + ^{55}Mn $\rightarrow$ ^{56}Mn* and p + ^{55}Cr $\rightarrow$ ^{56}Mn* systems respectively resulting in population of compound nucleus at high excitation energies even at low incident energies. Moreover, as we already explained, ^{52}V has many low lying energy levels, the first excited state is 17.2 keV whereas ^{52}Cr has very low number of low lying energy levels, the first excited state is 1.434 MeV. Although the J^{π} mismatch is large within 2$\hbar$ in ^{55}Mn(n,α)^{52}V and ^{55}Cr(p,α)^{52}V reactions, however, due to large number of low lying states in the residual nucleus ^{52}V, the alpha decay probability do not depend much on the CN J^{π}. However, in the case of ^{55}Fe(n,α)^{52}Cr and ^{55}Mn(p,α)^{52}Cr reactions, although the number of low lying energy states are low, the Jpi distribution of the CN ^{56}Fe is almost similar within 0-0.3 $\hbar$ difference even at low incident energies resulting in almost similar alpha decay branching ratio. All these contributed to the validity of W-E approximation in the systems we studied.

At this juncture, with limited systems and results presented in the present work, it is not possible to generalize the conclusion we made above, and it is not possible to give a range of target masses and J^{π} mismatch unless we perform such studies. This will be part of our future scope. However, at this point, due to the motivations that we mentioned in our Introduction, from the point of view of reactor applications in which ^{55}Cr and ^{55}Fe are produced which are both unstable, we restrict our studies and manuscript only for these four reactions. And the results are practically applicable since ^{55}Mn is stable and there are many experimental results. What we can mention is based on the results we obtained, and within 2 $\hbar$ of J^{π} mismatch, for the systems we studied, we observe similar alpha decay branching ratio. However, we also observe that the alpha decay branching ratio is also sensitive to the level structure of the low lying energy states of the residual nucleus; this therefore suggested that each reaction should be considered on a case by case basis.

Declaration of competing interest

The authors declare that they have no known competing financial interests or personal relationships that could have appeared to influence the work reported in this paper.

Acknowledgement

The authors are grateful to Dr. A.J. Koning for fruitful discussions on the TALYS-1.9 calculations. One of the authors L.R. Hlondo is thankful to the University Grant Commission for providing financial support under National Fellowship for Higher Education (Sanction No.: F1-17.1/2015-16/NFST-2015-17-ST-MIZ-3585) to carry out his research work.

References

[1] S.N. Ghoshal, Phys. Rev. 80 (1950) 939.
[2] J.E. Escher, J.T. Burke, F.S. Dietrich, N.D. Scielzo, I.J. Thompson, W. Younes, Rev. Mod. Phys. 84 (2012) 353.
[3] J.D. Cramer, H.C. Britt, Nucl. Sci. Eng. 41 (1970) 177.
[4] H.C. Britt, J.B. Wilhelmy, Nucl. Sci. Eng. 72 (1979) 222.

Please cite this article in press as: L.R. Hlondo, B. Lalremruata, Entrance channel effects on the alpha decay probabilities of neutron and proton induced reactions for target mass A=55, Nucl. Phys. A (2020), https://doi.org/10.1016/j.nuclphysa.2020.121844

[5] W. Younes, H.C. Britt, Phys. Rev. C 67 (2003) 024610.
[6] W. Younes, H.C. Britt, Phys. Rev. C 68 (2003) 034610.
[7] M. Petit, et al., Nucl. Phys. A 735 (2004) 345.
[8] C. Plettner, et al., Phys. Rev. C 71 (2005) 051602(R).
[9] J.T. Burke, et al., Phys. Rev. C 73 (2006) 054604.
[10] B.F. Lyles, et al., Phys. Rev. C 76 (2007) 014606.
[11] B.F. Lyles, et al., Phys. Rev. C 76 (2007) 019905.
[12] B.K. Nayak, et al., Phys. Rev. C 78 (2008) 061602.
[13] B.L. Goldblum, et al., Phys. Rev. C 80 (2009) 044610.
[14] M. Basunia, et al., Nucl. Instrum. Methods Phys. Res., Sect. B 267 (2009) 1899.
[15] S.R. Lesher, et al., Phys. Rev. C 79 (2009) 044609.
[16] B.L. Goldblum, S.G. Prussin, L.A. Bernstein, W. Younes, M. Guttormsen, H.T. Nyhus, Phys. Rev. C 81 (2010) 054606.
[17] S.R. Lesher, et al., Nucl. Instrum. Methods Phys. Res., Sect. A 621 (2010) 286.
[18] G. Kessedjian, et al., Phys. Lett. B 692 (2010) 297.
[19] J.J. Ressler, et al., Phys. Rev. C 81 (2010) 014301.
[20] J.J. Ressler, et al., Phys. Rev. C 83 (2011) 054610.
[21] V.V. Desai, et al., Phys. Rev. C 87 (2013) 034604.
[22] V.V. Desai, B.K. Nayak, A. Saxena, E.T. Mirgule, S.V. Suryanarayana, Phys. Rev. C 88 (2013) 014613.
[23] Bhawna Pandey, et al., Phys. Rev. C 93 (2016) 021602(R).
[24] C. Forssen, F.S. Dietrich, J. Escher, R.D. Hoffman, K. Kelley, Phys. Rev. C 75 (2007) 055807.
[25] L.A. Bernstein, et al., Technical Report, Lawrence Livermore National Laboratory, Livermore, CA, 2006.
[26] S. Boyer, et al., Nucl. Phys. A 775 (2006) 175.
[27] B.L. Goldblum, S.G. Prussin, U. Agvaanluvsan, L.A. Bernstein, D.L. Bleuel, W. Younes, M. Guttormsen, Phys. Rev. C 78 (2008) 064606.
[28] J.M. Allmond, et al., Phys. Rev. C 79 (2009) 054610.
[29] R. Hatarik, et al., Phys. Rev. C 81 (2010) 011602.
[30] G. Boutoux, et al., Phys. Lett. B 712 (2012) 319.
[31] N.D. Scielzo, et al., Phys. Rev. C 81 (2010) 034608.
[32] Huo Junde, Nucl. Data Sheets 109 (2008) 787.
[33] A. Wallner, et al., J. Korean Phys. Soc. 59 (2011) 1378–1381.
[34] B. Lalremruata, S.D. Dhole, S. Ganesan, V.N. Bhoraskar, Nucl. Phys. A 821 (2009) 23.
[35] E.B. Paul, R.L. Clarke, Can. J. Phys. 31 (1953) 267.
[36] I. Kumabe, J. Phys. Soc. Jpn. 13 (1958) 325.
[37] E. Weigold, Aust. J. Phys. 13 (1960) 186.
[38] J. Nix, D. Chittenden, D.G. Gardner, Oak ridge operations office, Contract Rep. 367 (1961) 6.
[39] O.N. Kaul, Nucl. Phys. 39 (1962) 325.
[40] F. Gabbard, B.D. Kern, Phys. Rev. 128 (1962) 1276.
[41] A. Peil, Nucl. Phys. 66 (1965) 419.
[42] C.S. Khurana, I.M. Govil, Nucl. Phys. 69 (1965) 153.
[43] M. Bormann, E. Fretwurst, P. Schehka, G. Wrege, H. Buttner, A. Lindner, H. Meldner, Nucl. Phys. 63 (1965) 438.
[44] E. Frevert, Acta Phys. Austriaca 20 (1965) 304.
[45] B. Minetti, A. Pasquarelli, Z. Phys. 199 (1967) 275.
[46] E. Zupranska, K. Rusek, J. Turkiewicz, P. Zupranski, Acta Phys. Pol. 11 (1980) 853.
[47] P.N. Ngoc, S. Gueth, F. Deak, A. Kiss, Ph.D Thesis of dissertation submitted to Hungarian Institute for Experimental Physics, 1980.
[48] R. Vanska, R. Rieppo, Nucl. Instrum. Methods 171 (1980) 281.
[49] M. Florek, J. Oravec, I. Szarka, K. Holy, U. Jahn, H. Helfer, Czechoslov. J. Phys. 34 (1984) 30.
[50] M. Bostan, S.M. Qaim, Phys. Rev. C 49 (1994) 266.
[51] A. Fessler, A.J.M. Plompen, D.L. Smith, J.W. Meadows, Y. Ikeda, Nucl. Sci. Eng. 134 (2000) 171.
[52] Yanbin Zhang, Liangyong Zhao, Xiangzhong Kong, Rong Liu, Li Jiang, Radiat. Phys. Chem. 81 (2012) 1563.
[53] A.A. Filatenkov, International Atomic Energy Agency Report No. INDC(CCP)-0460, 2016.
[54] N. Otuka, E. Dupont, V. Semkova, B. Pritychenko, A.I. Blokhin, M. Aikawa, S. Babykina, M. Bossant, G. Chen, S. Dunaeva, R.A. Forrest, T. Fukahori, N. Furutachi, S. Ganesan, Z. Ge, O.O. Gritzay, M. Herman, S. Hlavač, K. Katō, B. Lalremruata, Y.O. Lee, A. Makinaga, K. Matsumoto, M. Mikhaylyukova, G. Pikulina, V.G. Pronyaev, A. Saxena, O. Schwerer, S.P. Simakov, N. Soppera, R. Suzuki, S. Takács, X. Tao, S. Taova, F. Tárkányi, V.V. Varlamov, J. Wang, S.C. Yang, V. Zerkin, Y. Zhuang, Nucl. Data Sheets 120 (2014) 272.

Please cite this article in press as: L.R. Hlondo, B. Lalremruata, Entrance channel effects on the alpha decay probabilities of neutron and proton induced reactions for target mass A=55, Nucl. Phys. A (2020), https://doi.org/10.1016/j.nuclphysa.2020.121844

[55] W. Hauser, H. Feshbach, Phys. Rev. 87 (1952) 366.
[56] A.J. Koning, S. Hilaire, M. Duijvestijn, TALYS-1.8, a Nuclear Reaction Program, NRG - 1755 ZG Petten, The Netherlands, 2008.
[57] A.J. Koning, J.P. Delaroche, Nucl. Phys. A 713 (2003) 231.
[58] R. Capote, M. Herman, P. Oblozˇinsky´, P.G. Young, S. Goriely, T. Belgya, A.V. Ignatyuk, A.J. Koning, S. Hilaire, V. Plujko, M. Avrigeanu, O. Bersillon, M.B. Chadwick, T. Fukahori, S. Kailas, J. Kopecky, V.M. Maslov, G. Reffo, M. Sin, E. Soukhovitskii, P. Talou, Y.L. Han, Z.G. Ge, Nucl. Data Sheets 110 (2009) 3107.
[59] S. Hilaire, M. Girod, S. Goriely, A.J. Koning, Phys. Rev. C 86 (2012) 064317.
[60] J. Kopecky, M. Uhl, Phys. Rev. C 41 (1990) 1941.
[61] D.M. Brink, Nucl. Phys. 4 (1957) 215.
[62] P. Axel, Phys. Rev. 126 (1962) 671.
[63] S. Goriely, Phys. Lett. B 436 (1998) 10.
[64] A.J. Koning, D. Rochman, J. Kopecky, J.C. Sublet, M. Fleming, E. Bauge, S. Hilaire, P. Romain, B. Morillon, H. Duarte, S.C. vanderMarck, S. Pomp, H. Sjostrand, R. Forrest, H. Henriksson, O. Cabellos, S. Goriely, J. Leppanen, H. Leeb, A. Plompen, R. Mills, TENDL-2017: TALYS-based evaluated nuclear data library, https://tendl.web.psi.ch/tendl_2017/tendl2017.html.
[65] M.B. Chadwick, P. Obložinský, M. Herman, et al., Nucl. Data Sheets 107 (2006) 2931–3060.

Please cite this article in press as: L.R. Hlondo, B. Lalremruata, Entrance channel effects on the alpha decay probabilities of neutron and proton induced reactions for target mass A=55, Nucl. Phys. A (2020), https://doi.org/10.1016/j.nuclphysa.2020.121844

ABSTRACT OF THESIS

ENTRANCE CHANNEL EFFECTS ON THE ALPHA DECAY PROBABILITIES OF NEUTRON AND PROTON INDUCED REACTIONS FOR TARGET MASS A=55 AND CHARACTERIZATION OF RF OSCILLATOR FOR LOW ENERGY CHARGED PARTICLE ACCELERATOR

H. LALREMRUATA

DEPARTMENT OF PHYSICS

MIZORAM UNIVERSITY

ABSTRACT

A complete nuclear data for all isotopes are desirable for nuclear astrophysics, safe reactor design, transmutation, understanding nuclear structure and reaction dynamics, improving existing nuclear model parameters for better prediction, industrial and medical applications. However, for various nuclear applications, experimentally measured nuclear data are not available to cover all the required energies. Moreover, due to the fact that some isotopes are unstable and short-lived, or the reaction cross section itself is very small, it is sometimes impossible or difficult to measure their cross sections directly with the present technology. Therefore, in such cases, incomplete or inconsistent experimental data are coupled with the optimum theoretical models to produce evaluated data (Gunsing *et al.*, 2015; Gilbert and Cameron, 2014). These evaluated data are produced such that the important data for all the nuclear reactions at all energy regions are covered. Although the existing nuclear data covers rather complete information for all the nuclear reactions, there is still a need for further improvement in the evaluation of nuclear data which may include evaluating the validity of nuclear models and the choice of parameters within it, and the technique adopted in analyzing a variety of observables related to the compound nucleus decay (Ajay Kumar, 2014).

In nuclear reactor developments, the generation of hydrogen and helium through neutrons has always been a very serious problem. In addition to the production of hydrogen and helium, the other processes such as atomic displacements and transmutations, etc. can produce micro-structural defects in the material. The structural

material, generally stainless steel, comprises of Fe, Ni, Cr, Mn, Co, Nb, etc. In the Stainless Steel of type SS316, the content of Fe and Cr are approximately 65% and 17% respectively. In the fusion reactors, the structural materials are exposed at a high fluence of 14.1 MeV neutrons. The high production rate of ^{55}Fe, having a half life of 2.744 years (Huo Junde, 2008), from the neutron exposure of natural iron via the threshold reaction ^{56}Fe(n,2n)^{55}Fe, ^{54}Fe(n,γ)^{55}Fe, ^{58}Ni(n,α)^{55}Fe and the production rate of ^{55}Cr via ^{53}Cr(n,γ)^{54}Cr(n,γ)^{55}Cr, ^{54}Cr(n,γ)^{55}Cr and ^{52}Cr(n,γ)^{53}Cr(n,γ)^{54}Cr(n,γ)^{55}Cr is of main concern as an activation product during the lifetime of an operating reactor (Wallner *et al.*, 2011). Since Chromium is structural elements in fission and fusion reactors, accurate knowledge of neutron or proton induced reaction cross sections for its stable as well as unstable isotopes is very important. The neutron induced reactions on ^{55}Fe and other long-lived radionuclides, however, are difficult to measure using the standard activation techniques due to the unstable nature of the targets and their low activities. For this purpose and other applications, the values of total cross-sections for the production of charged particles in the reactor materials through nuclear reactions induced by different projectiles in the energy range from few keV to 20 MeV are required (Lalremruata *et al.*, 2009). Recent studies have shown that there is a possibility in extracting the total cross sections of such nuclei which are impossible or difficult to measure experimentally.

In the present work, we investigate the entrance channel effects on the alpha decay probabilities for the neutron and proton induced reactions for target mass A=55 from few MeV up to 20 MeV. In particular, we studied two combinations, ^{55}Fe(n,α)^{52}Cr and ^{55}Mn(p,α)^{52}Cr; ^{55}Mn(n,α)^{52}V and ^{55}Cr(p,α)^{52}V reactions. Each combination is

producing the same compound nucleus at the same excitation energy, but with different J^{π} distributions. We investigate how the difference in the J^{π} distributions of the compound nuclei at the same excitation energy formed by the neutron and proton induced reactions influence the alpha decay channel. The dependence of the alpha decay branching ratio on the level structure of the residual nuclei is also studied. The validity of the Weisskopf-Ewing limit is also discussed in detail. An investigation has also been made to study the effect of the compound nucleus J^{π} mismatch on the gamma branching ratios between the neutron and proton induced reactions on the isotopes under study. The theoretical simulation is done using the nuclear reaction code TALYS-1.9 (Koning *et al.*, 2008). The results are compared with experimental results whenever available, and are discussed in detail.

Self-excited push-pull vacuum tube oscillator is one of the most commonly used oscillators in radio frequency (RF)-ion plasma sources for generation of ions using radio frequency. Even though there are now more efficient semi-conductor based RF power sources, vacuum tube oscillator, especially self-excited push pull RF generator, continues to occupy important place in the design and construction of RF ion sources due to its circuit simplicity, robustness, compactness, and ease of maintenance. However, electron tubes are high voltage devices and have operating conditions different from that of semiconductor devices. Therefore, proper understanding of the performance of such device is important for their application in ion sources. The present work aimed at providing a more detailed description of the oscillator system and operational characteristics of a self-excited push-pull oscillator using twin beam-power

tetrode, constructed for operation at around 100 MHz. However, in spite of its fundamental role in the process of plasma formation, the working and operational characteristics are the most frequently skip part in the descriptions of RF ion sources in literatures.

In the development of RF ion sources, the main factors to be optimized are the operating frequency and output power of the RF oscillator, extraction probe voltage and the ion current. Out of the various factors that affect the ion current extracted from ion sources, the effect of RF power on the plasma density is the main interest of the present study. Numerous works have been seen in literature on the design and construction of RF ion sources (Brown *et al.*, 2004; Tripathi *et al.*, 2011). However, these studies are mainly devoted to the extraction and different characteristics of plasma, and little attention has been paid towards RF oscillator itself.

In the operation of vacuum tube RF oscillator, the only parameter used to adjust the total output power level is the DC plate voltage. Thus understanding the relationship between the two parameters is important for proper operation of the oscillator. To measure the output power of the oscillator, two simple and inexpensive techniques, namely, a modified form of photometric method and an RF peak voltage detection method were used. Photometric method is one of the oldest methods of RF power measurement in history. It is based on the ability of incandescent lamp to convert RF power into light which is then measured with a photometer (Conhaim *et al.*, 1963; Technical Manual TM11-685/TO31R-1-9, 1961). However, this method is rather

classified as power indicator than absolute power measurement due to the inductive reactance of the load at high frequency. On the other hand the latter method is one of the standard and well known methods where RF power is made to be absorbed by a purely resistive load and the electrical energy consumed is calculated from the RF signal peak voltage. The detail procedure for RF power measurement using these two different methods is discussed. The power curves obtained from these measurements are quadratic in nature and increase with increase in plate voltage. However, the RF output power as measured by photometric methods is always less than the value calculated from peak voltage measurements. This difference is due to the fact that the filament coil of the ordinary light bulb used as load/detector in photometric method is not a perfect inductor. The effect of inductive reactance on power transfer to load was further investigated and a technique is developed to estimate the amount of power correction needed in the photometric measurement result.

As seen in literature, although it is now understood that saturation in the ion current can be achieved at a particular frequency, it is still important to understand the operational characteristics of an RF oscillator in terms of its operating frequency. Therefore, the effect of the operating frequency of an RF oscillator on its output power is studied in the present work. Since the operating frequency is basically determined by the design of the tank circuit or RF coil, used as antenna, the dependence of the operating frequency on the design of the RF coil is also discussed.

REFERENCES

Ajay Kumar, (2014), "Study of angular momentum variation due to entrance channel effect in heavy ion fusion reactions", *J. Phys. Conf. Ser.* **515**, 012011(1-9).

Brown I.G., (2004), "The Physics and Technology of Ion Sources", Second Edition., Berlin: Wiley-VCH.

Conhaim R.L., (1963), "R.F. power output measurements", *Electronics world* **70**, 53–56.

Gilbert A. and Cameron A.G.W., (1965), "A composite nuclear-level density formula with shell corrections", *Can. J. Phys.*, **43**, 1446-1496.

Gunsing F., Aberle O., Andrzejewski J., Becares L.A.V., Bacak M., Balibrea-Correa J., Barbagallo M., Barros S., Becvar F., Beinrucker C., Belloni F., Berthoumieux E., Billowes J., Bosnar D., Brugger M., Caamano M., Calvino F., Calviani M., Cano-Ott D., Cardella R., Castelluccio D.M., Cerutti F., Chen Y., Chiaveri E., Colonna N., Cortes-Giraldo M.A., Cortes G., Cosentino L., Damone L., Deo K., Diakaki M., Domingo-Pardo C., Dupont R.D.E., Duran I., Fernandez-Dominguez B., Ferrari A., Ferreira P., Finocchiaro P., Frost R.W., Furman V., Ganesan S., Gawlik A., Gheorghe I., Glodariu T., Goncalves I.F., Gonzalez E., Goverdovski A., Griesmayer E., Guerrero C., Gobel K., Harada H., Heftrich T., Heinitz S., Hernandez-Prieto A., Heyse J., Jenkins G., Jericha E., Kappeler F., Kadi Y., Katabuchi T., Kavrigin P., Ketlerov V., Khryachkov V., Kimura A., Kivel N., Kokkoris M., Krticka M., Leal-Cidoncha E., Lederer C., Leeb H., Lerendegui J., Licata M., Meo S.L., Losito R., Macina D., Marganiec J., Martinez T., Massimi C., Mastinu P., Mastromarco M., Matteucci F., Maugeri E.A., Mendoza E.,

Mengoni A., Milazzo P.M., Mingrone F., Mirea M., Montesano S., Musumarra A., Nolte R., Oprea A., Pinto F.R.P., Paradela C., Patronis N., Pavlik A., Perkowski J., Porras J.I., Praena J., Quesada J.M., Rauscher T., Reifarth R., Riego-Perez A., Robles M., Rubbia C., Ryan J.A., Sabate-Gilarte M., Saxena A., Schillebeeckx P., Schmidt S., Schumann D., Sedyshev P., Smith A.G., Stamatopoulos A., Suryanarayana S., Tagliente G., Tain J.L., Tarifeno-Saldivia A., Tassan-Got L., Tsinganis A., Valenta S., Vannini G., Variale V., Vaz P., Ventura A., Vlachoudis V., Vlastou R., Wallner A., Warren S., Weigand M., Weiss C., Wolf C., Woods P.J., Wright T., Zugec P., (2015), "Nuclear data measurements at the upgraded neutron time-of-flight facility n TOF at CERN", 14th International Conference on Nuclear Reaction Mechanisms, *https://cds.cern.ch/record/2115398*, 323-330.

Huo Junde, (2008), "Nuclear Data Sheets for A = 55", *Nucl. Data Sheets* **109**, 787-942.

Koning A.J., Hilaire S., Goriely S., (released in December, 2017), computer code TALYS, version 1.9, *http://www.talys.eu*.

Lalremruata B., Dhole S.D., Ganesan S., Bhoraskar V.N., (2009), "Double differential cross-sections of (n,α) reactions in aluminium and nickel at 14.77 MeV neutrons", *Nucl. Phys. A* **821**, 23-35.

TM 11-685/TO 31R-1-9, (1961), "Fundamentals of single-side band communication", Technical Manual, Departments of the Army and the Air Force, Washington DC, 119.

Tripathi S.K.P., Pribyl P., Gekelman W., (2011), "Development of a radio-frequency ion beam source for fast-ion studies on the large plasma device", *Rev. Sci. Instrum.* **82**, 93501.

Wallner A., Buczak K., Lederer C., Vonach H., Faestermann T., Korschinek G., Poutivtsev M., Rugel G., Klix A., Seidel K., Plompen A., Semkova V., (2011), "Production of Long-lived Radionuclides ^{10}Be, ^{14}C, ^{53}Mn, ^{55}Fe, ^{59}Ni and ^{202g}Pb in a Fusion Environment", *J. Korean Phy. Soc.* **59**, 1378-1381.